JOINT TRANSPORTATION RESEARCH PROGRAM

Final Report

**A METHOD FOR ACCOUNTING FOR PILE
SET UP AND RELAXATION IN PILE DESIGN
AND QUALITY ASSURANCE**

**Prasenjit Basu
Rodrigo Salgado
Monica Prezzi Tanusree
Chakraborty**

August 2009

INDOT Research Project Implementation Plan

Date: August 18, 2009

Research Project Number: SPR-2930

Project Title: A Method for Accounting for Pile Setup and Relaxation in Pile Design and Quality Assurance

Principal Investigator (PI): Prof. Rodrigo Salgado   *Project Administrator (PA):* _____

Note: If more than one implement or recommended, please fill in the information on each implementor's implementation items:

Name of Implementor: __Mir Zaheer/Nayyar Zia__

Items (Research Results) to be implemented:
- Validate conclusions of the report concerning setup gains by additional model pile and full-scale pile tests
- Investigate the limitations of state-of-practice dynamic testing in estimating or projecting forward short-term setup measurements
- Incorporate setup factors into the portion of the geotechnical design manual dealing with the design of piles in clay based on load testing (this can be done immediately, with some caution as confirmation is awaited)
- Incorporate the new equations for α into the portion of the geotechnical design manual dealing with the design of piles in clay
- Refine the methods proposed in this report for better pile design based on additional analyses and data

Help or resources needed for implementation (e.g., help from PI, funding, equipment, etc.):
- Additional funding, collaboration from implementers, access to well planned pile load testing data

Name of Implementor: _____

Items (Research Results) to be implemented:

Help or resources needed for implementation (e.g., help from PI, funding, equipment, etc.):

Name of Implementor: _____

Items (Research Results) to be implemented:

Help or resources needed for implementation (e.g., help from PI, funding, equipment, etc.):

Signatures of SAC members: _____

_____

Please send a copy of this form to the INDOT Research Division and FHWA with the final report.

A Method for Accounting for Pile Setup and Relaxation in Pile Design and Quality Assurance

Introduction

Pile foundations have been used in construction for thousands of years as an economical means of transmitting the loads from superstructures to the underlying soil or rock strata. In pile design, piles must be able to sustain axial loads from the superstructure without failing in bearing capacity or settling so much that structural damage occurs or serviceability of the superstructure is jeopardized.

The axial capacity of driven and, possibly to a lesser extent, jacked piles in clays has been observed to increase with time. This increase has become known as pile setup. When a displacement pile is driven or jacked into the soil, it displaces a soil volume equal to the volume of the pile. Thus, very high normal and shear forces are applied on the surrounding soil layer, causing increases of pore water pressure and changes in the stress state. It has also been observed that the pile capacity of driven piles increases with time in other soils, including loose to dense silt, sandy silt, silty sand and fine sand.

The mechanism of setup is different for sand and clay. In sand, dissipation of excess pore water pressure induced by pile driving may take only hours, causing only short-term setup, which has no impact on design or quality control. Long-term setup may still be substantial for sand but for other reasons. For clay (the focus of this report), which has very low hydraulic conductivity, excess pore pressures appear in the soil layer surrounding the pile after pile driving. With time, this excess pore pressure dissipates, and effective soil stresses increase. The main cause of pile setup in clay is dissipation of excess

pore water pressure. It causes increase in effective stress in the clay layer, and thus increased strength and stiffness of the clay around the pile, leading in turn to increase in the shaft and base resistances of the pile. After complete dissipation of excess pore water pressures, additional setup may occur at constant effective stress due to aging.

An accurate estimation of this pile capacity increase may lead to significant cost savings and safety in pile design. A better quantification of setup impacts, in particular, pile quality assurance/control because load tests performed shortly after installation are subjected to very limited setup. If short-term measurements can be projected out in time accurately, engineers can be assured that required capacities will be in place when needed (at the time structures are built and loaded). Hence, quantification of the pile capacity increase with time is necessary for cost-effective design of piles. A number of empirical relationships have been proposed in the literature to predict setup of piles. Researchers have investigated pile capacity increase with time for driven piles using semi-empirical, analytical and numerical techniques over the last several decades, but there has been little theoretical research done on studying the effect of setup on jacked piles in clay. This means that currently available methods are per force site specific and would require data for proper calibration that are simply not available but in the rare project. This report outlines a very promising approach to model shaft resistance of jacked/driven piles in clay. Piles in clay, except possibly piles bearing in very stiff clay, depend on shaft resistance for

most of their capacity; additionally, setup along the pile shaft is where most of the setup is observed; consequently, the report can be used as basis for estimating pile setup for piles in clay. The report provides values of the ratio of limit unit shaft resistance to undrained shear strength to be used in the short term (for comparison with measurements taken during load tests) and long-term (for use in design)

Findings

This research took advantage of advanced computational techniques and a realistic constitutive model for clay, developed specifically in the course of this work, to model installation of displacement (jacked) piles and their subsequent loading at various times after installation. Analysis for piles jacked into the ground using a large number of strokes suggests that the analysis asymptotically approaches installation of driven piles, although dynamic loading was not done. The predicted values of limit unit shaft resistance matches closely the results of experiments available in the literature as well as the results of the pile load tests used to develop the API pile design procedure.

Specifically, the present report shows that:
1) The ratio of the limit shaft resistance of displacement piles a long time after pile installation (after complete excess pore pressure dissipation) to that just after pile installation ranges from roughly 1.2 to roughly 1.4.

2) The changes in the soil caused by pile installation, a rest period and then loading are very complex and cannot be modeled with any reliability in a simplistic way.

3) The pile installation process is not simply a cavity expansion process, as many have believed. Shearing has a large impact in that it reduces the normal stress on the pile shaft from the very large stresses that would be predicted by cavity expansion alone. Cycles of shearing along the pile shaft cause further degradation of the normal stress on the pile-soil interface and therefore on the pile shaft resistance; however, the effect is small, not approaching the large degradation of shaft resistance observed in piles in sand.

4) With results of analyses such as presented in this report, it is possible to create effective design methods and quality assurance programs that provide a reliable basis to project from the resistance measured during pile load tests performed shortly after pile installation to the values of resistance that are of interest in design later. We have proposed values for what we called a setup factor to do exactly that.

Implementation

Engineers can incorporate the results of this research in their work in three separate ways:
(1) Quality assurance: Consider load tests successful when they produce values of shaft resistance consistent with values calculated using the values of α proposed in this report for loading applied in the short term (a short time after installation).

2) Design: Use the values of α proposed in this report for loading applied in the long term (after setup has taken place) when calculating limit unit shaft resistance.

(3) Design: When using load tests before pile design, project out values measured during load tests using the ratios of long-term to short-term capacities proposed in the report.

Contact

For more information:

Prof. Rodrigo Salgado
Principal Investigator School of Civil Engineering Purdue University West Lafayette IN 47907 Phone: (765) 494-5030 E-mail: rodrigo@purdue.edu

Indiana Department of Transportation
Office of Research and Development
1205 Montgomery Street, P.O. Box 2279
West Lafayette, IN 47906
Phone: (765) 463-1521
Fax: (765) 497-1665

Purdue University
Joint Transportation Research Program School of
Civil Engineering West Lafayette, IN 47907
Phone: (765) 494-9310
Fax: (765) 496-7996
E-mail: jtrp@ecn.purdue.edu
http://www.purdue.edu/jtrp

Final Report

FHWA/IN/JTRP-2009/24

A METHOD FOR ACCOUNTING FOR PILE SETUP AND RELAXATION IN PILE DESIGN AND QUALITY ASSURANCE

Prasenjit Basu
Graduate Research Assistant

Rodrigo Salgado
Professor of Civil Engineering

Monica Prezzi
Associate Professor of Civil Engineering

Tanusree Chakraborty
Graduate Research Engineer

Geotechnical Engineering
School of Civil Engineering
Purdue University

Purdue University West
Lafayette, Indiana
August 2009

1. Report No. FHWA/IN/JTRP-2009/24	2. Government Accession No.	3. Recipient's Catalog No.	
4. Title and Subtitle A Method for Accounting for Pile Setup and Relaxation in Pile Design and Quality Assurance		5. Report Date August 2009	
		6. Performing Organization Code	
7. Author(s) Prasenjit Basu, Rodrigo Salgado, Monica Prezzi, and Tanusree Chakraborty		8. Performing Organization Report No. FHWA/IN/JTRP-2009/24	
9. Performing Organization Name and Address Joint Transportation Research Program 550 Stadium Mall Drive Purdue University West Lafayette, IN 47907-2051		10. Work Unit No.	
		11. Contract or Grant No. SPR-2930	
12. Sponsoring Agency Name and Address Indiana Department of Transportation State Office Building 100 North Senate Avenue Indianapolis, IN 46204		13. Type of Report and Period Covered Final Report	
		14. Sponsoring Agency Code	
15. Supplementary Notes Prepared in cooperation with the Indiana Department of Transportation and Federal Highway Administration.			

16. Abstract

When piles are installed by jacking or driving, they cause substantial changes in the state of soil located near the pile. These changes result from the complex loading imposed on the soil by expansion of a cylindrical cavity to make room for the pile, by multiple cycles of shearing in the vertical direction as the pile gradually moves down into the ground, and by the slow drainage associated with clayey soils. If a pile is load-tested a short time after installation, it will develop an axial resistance that reflects the existence in the soil of the excess pore pressures caused by the installation process. After the excess pore pressures dissipate, the axial pile resistance will be different from that measured in the short term. This difference is referred to as pile setup (if the resistance increases) or relaxation (if the resistance drops). This report focuses on the pile setup observed in clayey soils, in which it can be quite significant.

Pile setup in clays result primarily from shaft resistance gains with time after installation because the base resistance contributes proportionally much less in soft to medium stiff clays, which are the focus of the research. Accordingly, our focus has been on analyzing setup in shaft resistance, validating the equations resulting from these analyses and then proposing design and quality assurance procedures based on the results of the analyses. The analyses were done using the finite element method and an advanced constitutive model developed specifically for this project. The constitutive model captures all the key features required for these analyses, and the finite element analyses are 1D analyses of shaft resistance that can handle the large deformations and displacements involved in pile installation. The results of the analyses compare well with load test data from the literature. Design equations for the unit shaft resistance are proposed. Equations for unit shaft resistance in the short term (for comparison with load tests) are also proposed.

17. Key Words Piles; piling; pile resistance; clay; pile setup	18. Distribution Statement No restrictions. This document is available to the public through the National Technical Information Service, Springfield, VA 22161		
19. Security Classif. (of this report) Unclassified	20. Security Classif. (of this page) Unclassified	21. No. of Pages 106	22. Price

Form DOT F 1700.7 (8-69)

TABLE OF CONTENTS

LIST OF TABLES

LIST OF FIGURES

CHAPTER 1. INTRODUCTION

1.1. <u>Background</u>

Pile foundations have been used in construction for thousands of years as an economical means of transmitting the loads from superstructures to the underlying soil or rock strata. Piles support the load applied from the superstructure Q_t through basically two sources: 1) friction between the pile shaft and the surrounding soil and 2) compressive resistance of the soil below the pile base. The frictional resistance offered by the soil surrounding the pile is called shaft resistance Q_s, and the compressive resistance offered by the soil at the base is referred to as base resistance Q_b (Figure 1.1).

Applied load Q_t

Pile head

Pile shaft

Shaft resistance Q_s

Pile base
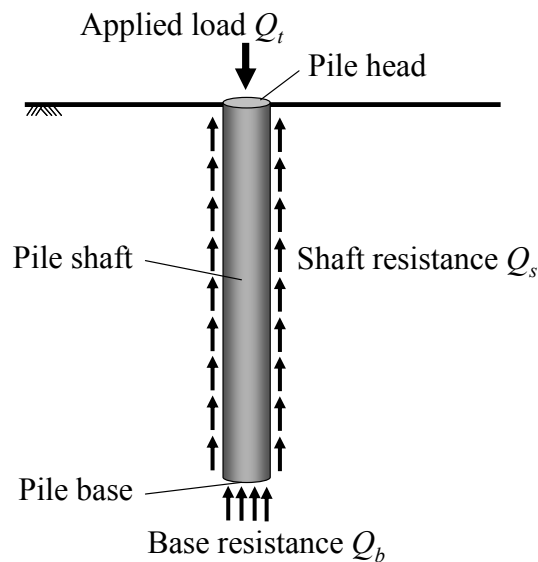
Base resistance Q_b

Figure 1.1 Sources of pile resistances

As the applied load at the pile head is increased, pile settlement increases until eventually the pile plunges into the ground when the shaft and base resistances reach their

limit values. During this loading process, there is high localization of shearing within a thin layer of soil around the pile shaft. As the thickness of this layer (shear zone) is very small, only a small amount of axial displacement of the pile is sufficient for full mobilization of the limit shaft capacity (Q_{sL}). In contrast to the shaft resistance mobilization mechanism, mobilization of the base resistance involves substantial amount of soil compression and requires large pile settlements. In fact, it is almost impossible for the plunging load or limit load Q_L of piles routinely used in practice to be reached with conventional equipment unless the soil profile is very weak. Therefore, ultimate load (Q_{ult}) criteria have been traditionally used to define the capacity of a pile. In the case of the 10%-relative-settlement criterion, Q_{ult} corresponds to the load for which the pile head displacement is 10% of the pile diameter; this is an example of an ultimate load criterion that is widely used in practice. Figure 1.2 illustrates these concepts.
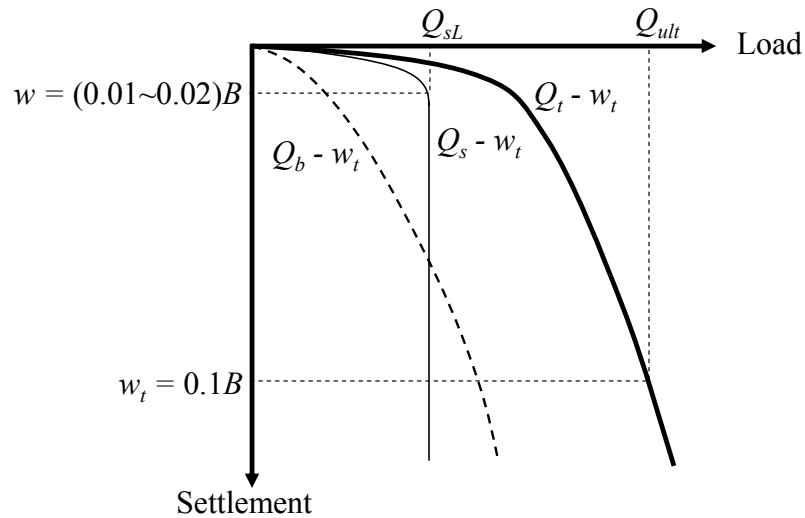
Figure 1.2 Typical load-settlement response of pile

1.2. <u>Problem Statement</u>

The axial capacity of driven and, possibly to a lesser extent, jacked piles in clays has been observed to increase with time. This increase has become known as pile setup. Effect of time on the capacity of displacement piles has been studied in the literature, both experimentally (Karlsrud and Haugen 1985, Axelsson 2000, Komurka *et al.* 2003, Skov and Denver 1988, Chow *et al.* 1998, Cho *et al.* 2000, Bullock 1999, Long *et al.* 1999, Cooke *et al.* 1979, Coop and Wroth 1989, Augustesen 2006) and theoretically (Randolph *et al.* 1979, Whittle and Sutabutr 1999, Titi and Wathugala, 1999). When a displacement pile is driven or jacked into the soil, it displaces a soil volume equal to the volume of the pile. Thus, very large normal and shear forces are applied on the surrounding soil layer, causing increases of pore water pressure and changes in the stress state. It has also been observed that the pile capacity of driven piles increases with time in other soils, including loose to dense silt, sandy silt, silty sand and fine sand.

The mechanism of setup is different for sand and clay. In sand, dissipation of excess pore water pressure induced by pile driving may take only hours, causing only short-term setup, which has no impact on design or quality control. Long-term setup may still be substantial for sand but for other reasons. For clay (the focus of this report), which has very low hydraulic conductivity, excess pore pressures appear in the soil layer surrounding the pile after pile driving. With time, this excess pore pressure dissipates, and effective soil stresses increase. The main cause of pile setup in clay is dissipation of excess pore water pressure. It causes increase in effective stress in the clay layer, and thus increased strength and stiffness of the clay around the pile, leading in turn to increase in the shaft and base resistances of the pile. After complete dissipation of excess pore water pressures, additional setup may occur at constant effective stress due to aging.

A number of empirical relationships have been proposed in the literature to predict setup of piles. Researchers have investigated pile capacity increase with time for driven piles using semi-empirical, analytical and numerical techniques over the last several decades, but there has been little theoretical research done on studying the effect of setup on jacked piles in clay. This means that currently available methods are per force

site specific and would require data for proper calibration that are simply not available but in the rare project.

This report outlines a very promising approach to model shaft resistance of jacked/driven piles in clay. Piles in clay, except possibly piles bearing in very stiff clay, depend on shaft resistance for most of their capacity; additionally, setup along the pile shaft is where most of the setup is observed; consequently, the report can be used as basis for effectively estimating pile setup for piles in clay. We perform one-dimensional (1-D) finite element analysis (FEA) to model the jacking and the subsequent loading of a cylindrical pile jacked in saturated clay. The FEA involves three distinct stages: (i) pile installation (jacking), (ii) dissipation of excess pore pressure generated during installation, and (iii) loading of the pile. These stages were also recognized by several other researchers in studies related to the shaft capacity of displacement piles in clay (Steenfelt *et al.* 1980, Bond and Jardine 1991, Azzouz *et al.* 1990, Lehane 1992, Lehane *et al.* 1994, Lee *et al.* 2004). However, no theoretical study has convincingly solved the problem in a single analysis comprising of installation, setup and loading; additionally, the constitutive model, used in these analyses were either too simple to capture different aspects of soil behavior (e.g., the strain-rate-dependent behavior of clay and the residual strength clay behavior) or it did not have all the features necessary to capture the setup process.

In this study we quantify pile setup through an integrated analysis framework that uses a suitable soil constitutive model and captures all features of pile installation, setup and loading. The report provides values of the ratio of limit unit shaft resistance to undrained shear strength to be used in the short term (for comparison with measurements taken during load tests) and long-term (for use in design).

1.3. Objectives and Organization

In Chapter 2, we describe the rate-dependent constitutive model that is used in the axisymmetric FEA to represent the constitutive behavior of clays (Chakraborty 2009). This constitutive model is based on two-surface plasticity theory and closely follows the formulations originally proposed by Manzari and Dafalias (1997) for triaxial loading

conditions and subsequently modified by several researchers (Li and Dafalias 2000, Papadimitriou and Bouckavalas 2002, Loukidis 2006, Loukidis and Salgado 2008a). The model has the capabilities of predicting the critical and residual states, predicting correct stiffness at small and large strains, capturing the effect of strain-rate on the shear strength of clay, and predicting clay behavior under varying loading conditions (capturing stress-induced anisotropy). The constitutive model parameters were obtained by fitting the results from simulations of different element tests (e.g., triaxial compression and extension, simple shear, isotropic and 1-D consolidation tests) using MATHCAD through real laboratory test data obtained from the literature.

In Chapter 3, we describe different aspects of the one-dimensional FE model that we use to model installation, setup and loading of a pile jacked in saturated clay. We consider pile jacking in clay to be a fully undrained process. At the end of installation and before simulation of pile loading (either from a static pile load test or from the superstructure), we allow the corresponding rest period, during which excess pore pressures will partially dissipate.

In Chapter 4, we present and discuss the FEA results obtained at different stages of installation, setup and loading of the pile. We also discuss the changes in the stress state of the soil during and after the installation of a displacement pile.

In Chapter 5, based on the FE simulation results, we propose a set of equations for the estimation of unit limit shaft resistance of a pile jacked in clay as function of the initial soil state and the intrinsic shear strength parameters. The proposed equations can be used for short- and long-term capacity calculations of displacement piles in clays. In this chapter we also propose setup factors, to be used in conjunction with the proposed equations, to calculate the shaft resistance of displacement piles in clays at different times after the installation. We summarize the key findings of this research and present the conclusions drawn from this study in Chapter 6.

CHAPTER 2. MODEL OF CLAY BEHAVIOR

2.1. <u>Introduction</u>

The constitutive model required for the present analyses should have certain capabilities in order for it to successfully simulate the clay behavior during the installation and subsequent loading of a jacked pile. The two-surface plasticity-based constitutive model described in detail in Chakraborty (2009) that we use in the present study has the capabilities of predicting the critical and residual states, capturing the effect of strain-rate on the shear strength of clay, and predicting clay behavior under varying loading conditions (capturing stress-induced anisotropy). The formulation of this constitutive model closely follows that of the other similar plasticity-based soil models proposed by several researchers (Manzari and Dafalias 1997, Li and Dafalias 2000, Papadimitriou *et al*. 2001, Papadimitriou and Bouckovalas 2002, Dafalias and Manzari 2004, Dafalias *et al*. 2006, Loukidis 2006, and Loukidis and Salgado 2008a).

During sustained shearing, platy clay particles tend to align along the direction of shearing. This tendency of clay particles to align along a shear plane facilitates shearing in that particular direction and results in further decrease in shear strength. At large shear strains, most natural clays have residual strength lower than that at critical state. Capturing the residual shear strength behavior of clays is particularly important when modeling the installation of jacked piles. During pile jacking in clay, large vertical shear strains are localized near the pile shaft and, under this high level of vertical shear strain, soil adjacent to the pile shaft is expected to reach residual shear strength (Salgado 2008).

At high strain rates, as those imposed in the case of pile jacking/driving in clay, both the clay undrained shear strength and stiffness increase. Strain-rate-dependent behavior of clay also plays an important role when a pile is loaded under undrained conditions (e.g., pile load tests). Therefore, analysis of installation and loading of jacked

piles in clay requires the constitutive model to simulate the strain rate-dependent evolution of shear strength and stiffness.

In both normally consolidated (NC) and overconsolidated (OC) natural clay deposits there usually is a K_0 (stress-induced) anisotropy, so that the ratio K_0 (= $\sigma'_{h0}/\sigma'_{v0}$) of horizontal to vertical effective stresses differs from unity. Stress-induced anisotropy can also be introduced during shearing starting from an initial isotropic ($K_0 = 1.0$) condition. According to Ladd and Varallyay (1965), the pore water pressure and the stress-strain responses of anisotropically consolidated clay under undrained shearing are significantly affected by the initial stress ratio. Therefore, a constitutive model should successfully capture the anisotropic behavior of clay during shearing.

To evaluate the shaft resistance of displacement piles in clay at some time after the installation, it is also important to know the exact stress state at the end of the consolidation phase (i.e., the phase during which the excess pore pressure generated during undrained pile installation dissipates) following pile installation. This requires the constitutive model to properly simulate the evolution of stresses during the primary consolidation process. The evolution of stresses during consolidation dictates the soil state (either NC or OC) at the end of consolidation. The deviatoric stress-strain response of clay becomes different (both under drained and undrained shearing) depending on the soil state (either NC or OC) at the end of consolidation. Clay may as well yield under loading along the hydrostatic axis (under zero deviatoric stress). Therefore, the constitutive model should capture both deviatoric and volumetric (hydrostatic) stress-strain response of clay with reasonable accuracy.

The constitutive model that we use in this study is based on the critical-state soil-mechanics (CSSM) framework. In this chapter, we briefly describe different components of the model, present the model parameters which were obtained by fitting the results from simulations of different element tests (e.g., triaxial compression and extension, simple shear, isotropic and 1-D consolidation tests) using MATHCAD through real laboratory test data obtained from the literature, and show some simulations of different element tests (Chakraborty 2009).

2.2. Key Components of the Constitutive Model

In the principal effective stress space ($\sigma_1'\sigma_2'\sigma_3'$ space), the model contains three conical surfaces with their apexes at the origin (i.e., at $\sigma_1' = \sigma_2' = \sigma_3' = 0$), a "bubble-like" yield surface, a dilatancy surface, and a "bounding" critical state surface. Figure 1.2a shows a schematic representation of these surfaces in the $\sigma_1'\sigma_2'\sigma_3'$ space. In the deviatoric plane, a flat surface (cap) is present on the critical state (bounding) surface (Figure 1.2b). The flat surface acts as a volumetric-hardening cap to the critical state (bounding) surface, and moves along the hydrostatic axis as the preconsolidation pressure p_c' increases. The material response within the yield surface is nonlinear elastic. During continuing shearing after reaching the yield surface, the stress state moves with the yield surface in the deviatoric stress space. The yield surface acts like a loading surface and moves in the stress space following a kinematic hardening rule. At any point of loading, the mechanical response of soil is governed by the distance between the current stress state and its projection (i.e., the image stress state) on the bounding surface.

(a)

(b)
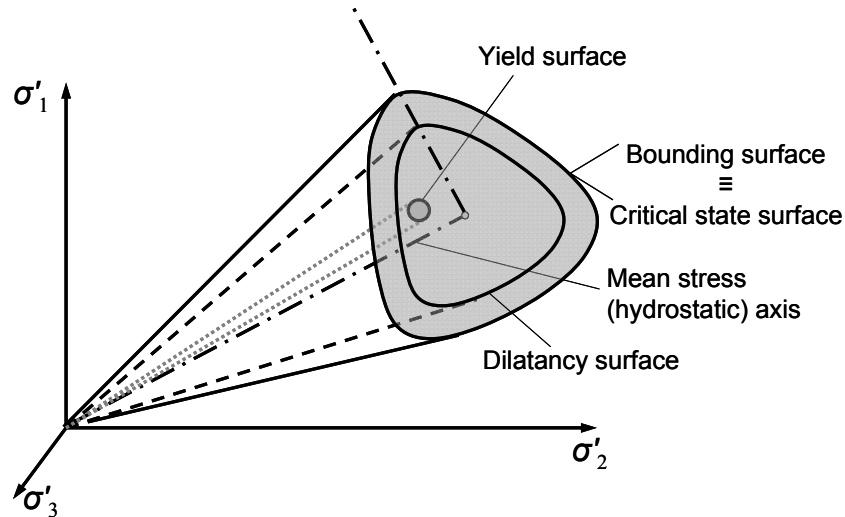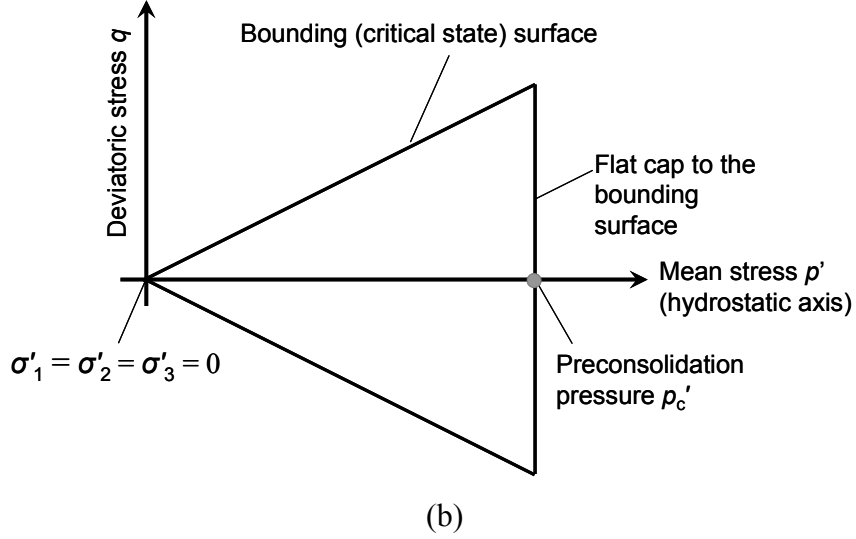
Figure 2.1 Schematic representation of the clay constitutive model: (a) different surfaces in the principal effective stress space, and (b) cap to the bounding surface

2.2.1. Stress-Strain Relationship

We first discuss the constitutive model without reference to the effects of loading rate. Loading rates that are sufficiently low for classical plasticity to be in effect are considered. The stress-strain equation of the model can be expressed as follows:

$$\dot{\sigma}'_{ij} = 2G\left(\dot{\varepsilon}_{ij} - \dot{\varepsilon}^{p}_{ij}\right) + \left(K - \frac{2}{3}G\right)\left(\dot{\varepsilon}_{kk} - \dot{\varepsilon}^{p}_{kk}\right) \tag{2.1}$$

where $\dot{\sigma}'_{ij}$ is the rate of stress, $\dot{\varepsilon}_{ij}$ is the total deviatoric strain rate and $\dot{\varepsilon}^{p}_{ij}$ is the plastic deviatoric strain rate, and $\dot{\varepsilon}_{kk}$ and $\dot{\varepsilon}^{p}_{kk}$ are total and plastic volumetric strain increments. G and K are the shear modulus and the bulk modulus, respectively.

2.2.2. Yield Surface

The yield surface in the present model is a circular cone in stress space with its apex at the origin as shown in Figure 2.1a. The general expression for this yield surface in multi-axial stress space is

$$f = \sqrt{\chi_{ij}\chi_{ij}} - \sqrt{2/3}\, m\, p' = 0 \tag{2.2}$$

and,

$$\chi_{ij} = s_{ij} - \alpha_{ij}\, p' \tag{2.3}$$

where s_{ij} = deviatoric stress tensor, α_{ij} is a kinematic tensor that represents the center of the yield surface, and m is the radius of the cone in the deviatoric plane (m is constant, which means that there is no isotropic hardening or softening of the yield surface).

The evolution of α_{ij} during loading represents the kinematic hardening of the yield surface; α_{ij} is also called the deviatoric back stress tensor. The factor $\sqrt{(2/3)}$ is introduced for convenience of interpretation of the projection on the deviatoric plane from the multi-axial space. The yield surface can also be written in the form:

$$f = \sqrt{\rho_{ij}\rho_{ij}} - \sqrt{2/3}\, m = 0 \tag{2.4}$$

where $r_{ij} = s_{ij}/p'$ and $\rho_{ij} = (r_{ij} - \alpha_{ij})$. After the differentiation of f and rearrangement, the loading direction L_{ij} becomes:

$$L_{ij} = \frac{\partial f}{\partial \sigma'_{ij}}$$

$$= \frac{\left(s_{ij} - p'\alpha_{ij}\right)}{\sqrt{\left(s_{kl} - p'\alpha_{kl}\right)\left(s_{kl} - p'\alpha_{kl}\right)}} - \frac{1}{3}\left[\frac{\left(s_{pq} - p'\alpha_{pq}\right)\alpha_{pq}}{\sqrt{\left(s_{kl} - p'\alpha_{kl}\right)\left(s_{kl} - p'\alpha_{kl}\right)}} + \sqrt{2/3}\, m\right]\delta_{ij}$$

$$\tag{2.5}$$

The loading direction L_{ij} normal to the yield surface is given as:

$$L_{ij} = \frac{\partial f}{\partial \sigma'_{ij}} = L'_{ij} + L''_{pq}\,\delta_{ij} \tag{2.6}$$

where

$$L'_{ij} = \frac{\left(s_{ij} - p'\alpha_{ij}\right)}{\sqrt{\left(s_{kl} - p'\alpha_{kl}\right)\left(s_{kl} - p'\alpha_{kl}\right)}} \tag{2.7}$$

is the loading tensor, and

$$L''_{pq} = -\frac{1}{3}\left[\frac{\left(s_{pq} - p'\alpha_{pq}\right)\alpha_{pq}}{\sqrt{\left(s_{kl} - p'\alpha_{kl}\right)\left(s_{kl} - p'\alpha_{kl}\right)}} + \sqrt{2/3}\,m\right] \tag{2.8}$$

L_{ij} defines the direction of loading and L'_{pq} represents the direction of loading within the deviatoric plane. The tensor δ_{ij} is the Kronecker's Delta. Equation (2.6) can also be expressed as:

$$L_{ij} = n_{ij} - \frac{1}{3}\left(n_{pq}\alpha_{pq} + \sqrt{\frac{2}{3}}\,m\right)\delta_{ij} \tag{2.9}$$

where

$$n_{ij} = \frac{\left(s_{ij} - p'\alpha_{ij}\right)}{\sqrt{\left(s_{kl} - p'\alpha_{kl}\right)\left(s_{kl} - p'\alpha_{kl}\right)}} \tag{2.10}$$

Once the stress state reaches the yield surface, it remains on the yield surface and starts moving with the yield surface. The mechanical behavior of soil is controlled by the distance of this current stress state from its projections on the bounding and dilatancy surfaces.

2.2.3. Bounding and Critical State Surface

In this model, the bounding surface is the critical state surface. The stress state may go outside the bounding surface slightly during a load increment, but it returns to the bounding surface upon convergence. We capture the peak shear strength during drained shearing of OC clay and undrained shearing of NC clay through the hardening parameter and the isotropic hardening of the dilatancy surface. Considering the critical state surface

to be the same as the bounding surface also helps us avoid the post-peak numerical oscillations caused by softening of the clay from the bounding surface to the critical state surface. In the proposed model, the bounding surface (which is also the critical state surface) is a cone, centered on the mean stress axis with apex at the origin. The locus of the bounding surface (or critical state surface) can be given as follows:

$$M_b \left(\equiv M_c \right) = g\left(\theta \right) M_{cc} \tag{2.11}$$

where M_{cc} is the critical stress ratio in triaxial compression; and $g(\theta)$ is a function of Lode's angle θ that determines the shape of the critical state surface, bounding surface and dilatancy surface on the deviatoric plane. We can express $g(\theta)$ as follows (Loukidis and Salgado 2008a):

$$g\left(\theta \right) = \frac{\left(1 - \dfrac{1 - c_1^{1/n_s}}{1 + c_1^{1/n_s}} \right)^{n_s}}{\left[1 - \left(\dfrac{1 - c_1^{1/n_s}}{1 + c_1^{1/n_s}} \right) \cos\left(3\theta \right) \right]^{n_s}} \tag{2.12}$$

where

$$c_1 = \frac{3}{M_{cc} + 3} \tag{2.13}$$

The parameter n_s in equation (2.12) was introduced by Loukidis and Salgado (2008a). If n_s is set equal to 1, then the function $g(\theta)$ becomes the same as that proposed by Manzari and Dafalias (1997) and Dafalias *et al.* (2004). If n_s is set equal to 0.25, then $g(\theta)$ becomes the same as that proposed by Sheng *et al.* (2000). The exponent n_s was introduced to improve predictions of friction angle at conditions other than triaxial compression or extension for all sets of possible M_{cc} values and for different types of clays. It also ensures convexity of the surfaces in the deviatoric plane.

Lode's angle θ can be expressed in terms of the principal components n_1, n_2 and n_3 of the loading tensor n_{ij} using the following equation:

$$\theta = \tan^{-1}\left[\frac{1}{\sqrt{3}}\left\{2\left(\frac{n_2 - n_3}{n_1 - n_3}\right) - 1\right\}\right] + \frac{\pi}{6} \tag{2.14}$$

According to Manzari and Dafalias (1997), θ can also be expressed in terms of effective stress as:

$$\cos 3\theta = \frac{3\sqrt{3}}{2}\left(\frac{\overline{S}}{\overline{J}}\right)^3 \tag{2.15}$$

where $\overline{S} = \left[\frac{1}{3}\mathbf{s} \cdot \mathbf{s} : \mathbf{s}\right]^{\frac{1}{3}}$, $\overline{J} = \left[\frac{1}{2}\mathbf{s} : \mathbf{s}\right]^{\frac{1}{2}}$ and $\mathbf{s} = \boldsymbol{\sigma} - p\mathbf{I}$ (bold face letters are used to represent tensor quantities; the symbol "**.**" represents the tensor product and the symbol "**:**" represents the scalar product of two tensors). Lode's angle $\theta = 0^{\circ}$ simulates the triaxial compression condition and $\theta = 60^{\circ}$ corresponds to triaxial extension. Thus, the value of $g(\theta)$ becomes equal to 1 for triaxial compression and to c_1 for triaxial extension (see equation 2.12). Therefore, the slopes of the critical state line at triaxial compression (M_{cc}) and triaxial extension (M_e) are directly correlated:

$$M_e = c_1 M_{cc} \tag{2.16}$$

This equation gives the flexibility to consider different friction angles for triaxial compression and extension.

2.2.4. Dilatancy Surface

The dilatancy surface is defined as:

$$M_d = g(\theta)\left(2M_{cc} + \frac{M_{cc} k_d \psi \text{ OCR}}{1 - \exp(k_d \psi \text{ OCR})}\right) \tag{2.17}$$

In equation (2.17), k_d is a model parameter defined as:

$$k_{\mathrm{d}} = \frac{M_{\mathrm{cc}}}{N - \Gamma} \tag{2.18}$$

The model always uses the current Overconsolidation Ratio (OCR) values in all the simulations. In this report, OCR is defined in terms of mean stress:

$$\mathrm{OCR} = \frac{p'_{\mathrm{c}}}{p'} \tag{2.19}$$

where p'_{c} represents the preconsolidation pressure, and p' is the current mean stress. The dilatancy surface hardens isotropically through the dependence of the stress ratio M_{d} on the state parameter ψ (which is the difference between the current void ratio e and the critical state void ratio e_{cr} at the same mean effective stress and thus determines whether the clay is dilative or contractive); M_{d} also depends on the OCR of the clay, as the dilatancy properties vary with the OCR. In the current formulation, M_{d} increases with increasing ψ and reaches an asymptote, though the rate of increase of M_{d} with ψ is much less as compared to the purely exponential formulation. This helps us to capture clay behavior reasonably well. As long as the stress state is inside the dilatancy surface, the response of the soil is contractive. The opposite is true if the stress state moves outside the dilatancy surface. At the phase transformation state (the state during shear loading when the plastic volumetric response during shearing changes from contractive to dilative) and at the critical state, the dilatancy is zero.

2.2.5. Volumetric Hardening Cap

Clay also hardens under the application of mean stress. The volumetric hardening cap controls the mean stress dependent hardening of clay. Following Li (2002), the flat cap to the bounding surface is expressed as:

$$F_{\mathrm{c}} = p' - p'_{\mathrm{c}} = 0 \tag{2.20}$$

For NC clay, $p' = p'_{\mathrm{c}}$, i.e., the stress state is on the cap. The value of p'$_{\mathrm{c}}$ defines the position of the cap on the hydrostatic axis. In the present model, the cap remains fixed on

the hydrostatic axis unless the mean stress state is on the cap. If the mean stress increases by dp'_c along the normal consolidation line, the volumetric hardening cap moves from p'_c to $p'_c+dp'_c$ on the hydrostatic axis (in the meridional plane) [Figure 2.2]. When $dp' <0$. the cap remains fixed on the hydrostatic axis.
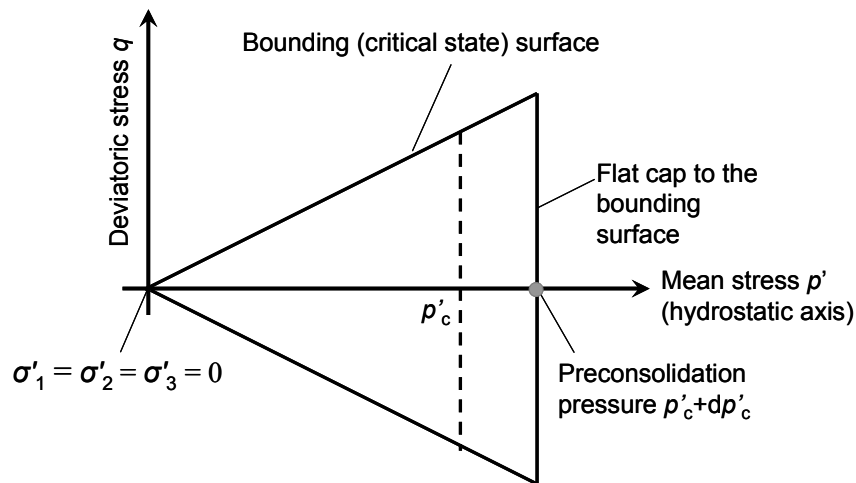
Figure 2.2 Volumetric hardening cap in the meridional plane

2.2.6. Residual Behavior of Clay

At critical state, the clay particles are in equilibrium under the applied confining stress, shear stress and void ratio. At this stage, clay particles roll over each other. Under prolonged shearing after critical state (at very large shear strains of 20% and even larger), clay particles get aligned with the direction of shearing so long as there is a sufficiently large normal stress σ' on the plane of shearing. The platy nature of the clay particles helps in this alignment. The friction angle reduces from its value at critical state ϕ_c to a reduced residual friction angle ϕ_r. The strength of the soil in the residual state is called the residual shear strength. The residual shear strength of clay is the product of the normal effective stress on the shearing plane by the tangent of the residual friction angle ϕ_r. It is important to note that ϕ_r decreases with increasing effective normal stress σ' on the plane of shearing, as larger normal stresses force greater particle alignment in the shearing direction.

In our constitutive model, the residual state is fully defined by the following equation:

$$M_{cc} = M_{c0} \exp\left\{(3\beta - 1)\ln\left(\frac{M_r}{M_{c0}}\right)\right\}$$

(2.21)

where M_{cc} is the current slope of the critical state line in effective mean stress p' vs deviatoric stress q space, M_{c0} is the initial slope of the critical state line, M_r is the slope of the residual state line when the residual angle reaches its minimum at a given normal stress. The parameter β controls the degree of particle alignment: $\beta = 0$ means that clay particles are fully aligned along the direction of shearing, and $\beta = 1/3$ means that there is no alignment. The rate equation of β controls the evolution of β from 0 to 1/3 in terms of the deviatoric strain $\dot{\varepsilon}_q$.

$$\dot{\beta} = b_r\left(M_r - M_{cc}\right)\dot{\varepsilon}_q$$

(2.22)

In equation 2.21, M_r depends on the normal stress σ' acting perpendicularly to the plane of shearing. To capture this, we correlate M_r with the mean stress p' through the following equation:

$$M_r = M_{c0}\exp\left[-Yp'\right] + M_{r,min}\left(1 - \exp\left[-Yp'\right]\right)$$

(2.23)

where Y is a model parameter defining the dependence of M_r on p' and $M_{r,min}$ is the slope of the residual state line in p' versus q space, corresponding to the absolute minimum residual friction angle $\phi_{r,min}$. When $Y = 0$, then M_r does not depend on p' and we obtain $M_r = M_{c0}$. With increasing Y, M_r decreases towards the absolute minimum residual stress ratio $M_{r,min}$.

2.2.7. Strain-Rate-Dependent Behavior of Clay

The constitutive model captures the strain-rate-dependent behavior of clay through the evolution of the critical state line (CSL) and normal consolidation line (NCL). Figure

2.3(a) shows the evolution of the CSL and NCL in the e-ln p' space. The movement of both the CSL and NCL is governed by the present stress state and the applied strain rate increment at any particular stage of loading. During strain hardening, the void ratio intercept Γ_0 (corresponding to the reference mean effective stress) of the CSL increases from its initial value to a maximum value Γ_{max}; during strain-softening Γ_{max} decreases continuously to return to its initial value Γ_0 when the soil reaches the critical state. At any stage of this evolution, the value of Γ (which also decides the location of the CSL in the e-ln p' space) is governed by the applied strain-rate increment. As the CSL moves in the e-ln p' space, the NCL also moves, maintaining a constant distance from the CSL. During the movement of the CSL and NCL in the e-ln p' space, image preconsolidation pressures (e.g., p'_{c2}, p'_{c3} in Figure 2.3a) are calculated along a projection of the overconsolidation line in the e-ln p' space. The hardening cap on the bounding (critical state) surface also moves during the evolution of the CSL and NCL in the e-ln p' space (see Figure 2.3b).

(a)

(b)
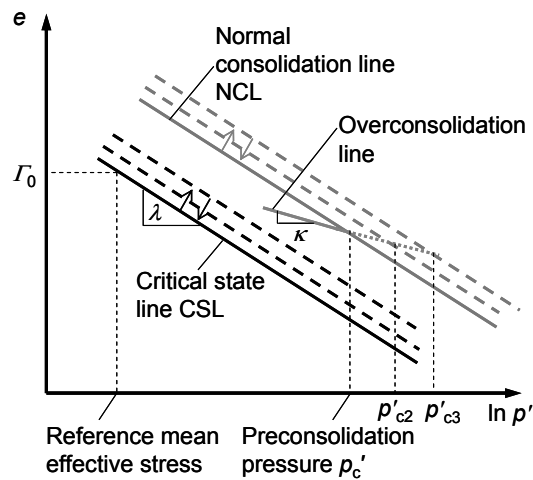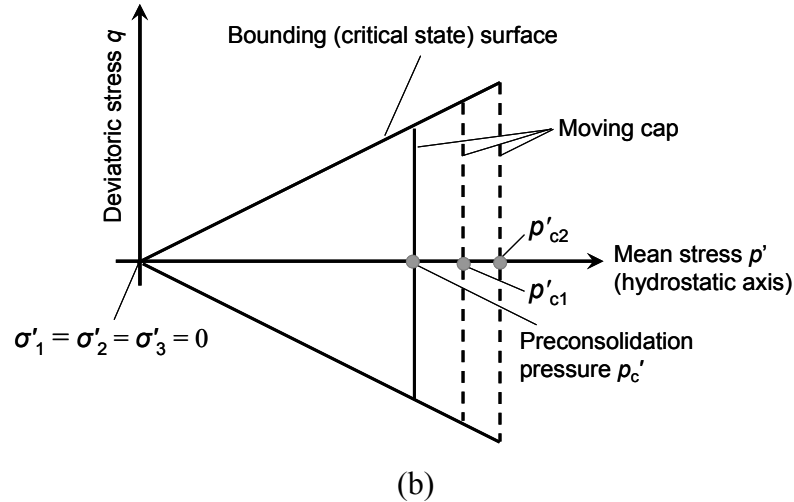
Figure 2.3 Evolution of (a) CSL and NCL (b) hardening cap

2.3. Determination of Model Parameters

We determine model parameters from data for tests on Boston Blue Clay (BBC), San Francisco Bay Mud (SFBM) and London Clay (LC). BBC is a low-plasticity marine clay, composed of illite and quartz (Terzaghi *et al*. 1996). SFBM is a highly-plastic silt containing a large amount of clay-sized particles (montmorillonite and illite), organic substances, shell fragments, and traces of sand (Bonaparte 1982). LC contains illite, kaolinite, smectite and quartz (Al-Tabbaa and Stegemann 2005, Gasparre *et al.* 2007a, Gasparre *et al.* 2007b). In order to show the applicability of the constitutive model to materials that are not strictly clays, we also determine the model parameters for Lower Cromer Till (LCT), which is a glacial till composed of sand (more than 50%), calcite and illite (clay content almost 17%) and almost no silt (Gens 1982) and has been treated in the literature as a clay.

We determine all model parameters based on experimental data found in the literature for one-dimensional and isotropic consolidation, resonant column test, triaxial compression and extension, simple shear and ring shear tests. Experimental data for BBC are taken from Papadimitriou *et al*. (2005), Pestana *et al.* (2002), Ling *et al.* (2002) [reproduced from Ladd and Varallyay (1965), Ladd and Edgers (1972), and Sheahan (1991)] and Santagata *et al.* (2007). SFBM data are obtained from Bonaparte (1982), Jain

(1985), Rau (1999), Jain and Nanda (2008) and Meehan (2006) for soil sample from Hamilton Airforce Base; Kirkgard and Lade (1991) and Stewart and Hussein (1993) for soil sample from Marina district; Hunt *et al.* (2002) for soil sample from Islais creek; and Henke and Henke (2003) for soil sample from Treasure Island site. All these tests were conducted on Young Bay Mud of Holocene age. Data for LC are collected from Gasparre (2005), Gasparre *et al.* (2007a), Gasparre *et al.* (2007b), Hight *et al.* (2003) for soil samples were collected from Heathrow Terminal 5 site; Bishop *et al.* (1971) for LC from Wraysbury and Walthamstow site. Data for LCT are obtained from Dafalias *et al.* (2006) based on the work done by Gens (1982). Model parameters are determined in a hierarchical manner and described in detail by Chakraborty (2009). In this report, we only tabulate the model parameters for BBC, SFBM and LC (Table 2.1).

Table 2.1 Constitutive model parameters for different clays

Model Relationships	Parameters	Parameter Value			Test Data Required
		BBC	SFBM	LC	
Small-strain (elastic) Poisson's Ratio	ν	0.25	0.24	0.2	Test using local strain transducer or isotropic consolidation or 1-D consolidation with unloading
G_0 correlation parameter	C_g	250	200	100	Bender element tests
Elastic moduli with degradation (G and K)	ζ	5 ± 2	5 ± 2	10 ± 5	Isotropic consolidation or 1-D consolidation
	κ	0.036	0.052	0.064	Isotropic consolidation or 1-D consolidation
Normal consolidation line	N	1.138	1.9	1.07	Isotropic consolidation or 1-D consolidation
	λ	0.187	0.404	0.168	Isotropic consolidation or 1-D consolidation
Critical state surface	M_{c0}	1.305	1.157	0.827	Triaxial compression test
	ρ	2.7	2.2	2.5	Isotropic consolidation or 1-D consolidation
Dilatancy surface	D_0	1 ± 0.2	0.5 ± 0.1	1 ± 0.2	Triaxial compression test
Flow rule	c_2	0.95	0.95	0.95	Simple shear or other plane-strain test
	n_s	0.2	0.2	0.2	Simple shear or other plane-strain test
Hardening	h_0	1.1 ± 0.2	1.5 ± 0.3	1.5 ± 0.3	Triaxial compression test
Strain-rate-dependent model parameter	C_0	7 ± 2	0.007 ± 0.001	7 ± 2	Strain-rate-dependent triaxial compression test
	a_{rate}	0.12 ± 0.01	0.1 ± 0.01	0.12 ± 0.01	Strain-rate-dependent triaxial compression test
	b_{rate}	0.01	0.01	0.01	Strain-rate-dependent simple shear test
	c_{rate}	0.00001	0.00001	0.00001	Strain-rate-dependent triaxial compression test or ring shear test
Residual state	$M_{r,min}$	-	0.615	0.33	Ring shear test
	b_r	-	0.01 ± 0.001	0.03 ± 0.001	Ring shear test
	Y	-	0.02 ± 0.002	0.015 ± 0.002	Ring shear test

2.4. Model Simulations for Rate-Independent Behavior of Clay

2.4.1. Consolidation Behavior

Figure 2.4(a) through (d) shows the e-ln(p') response of BBC, LCT, SFBM during one-dimensional consolidation and LC for isotropic consolidation, respectively. Test data for SFBM and LC are obtained from Jain (1985) and Gasparre (2005), respectively. The model captures the loading-unloading-reloading loop using the same model parameters throughout.

(a)   (b)
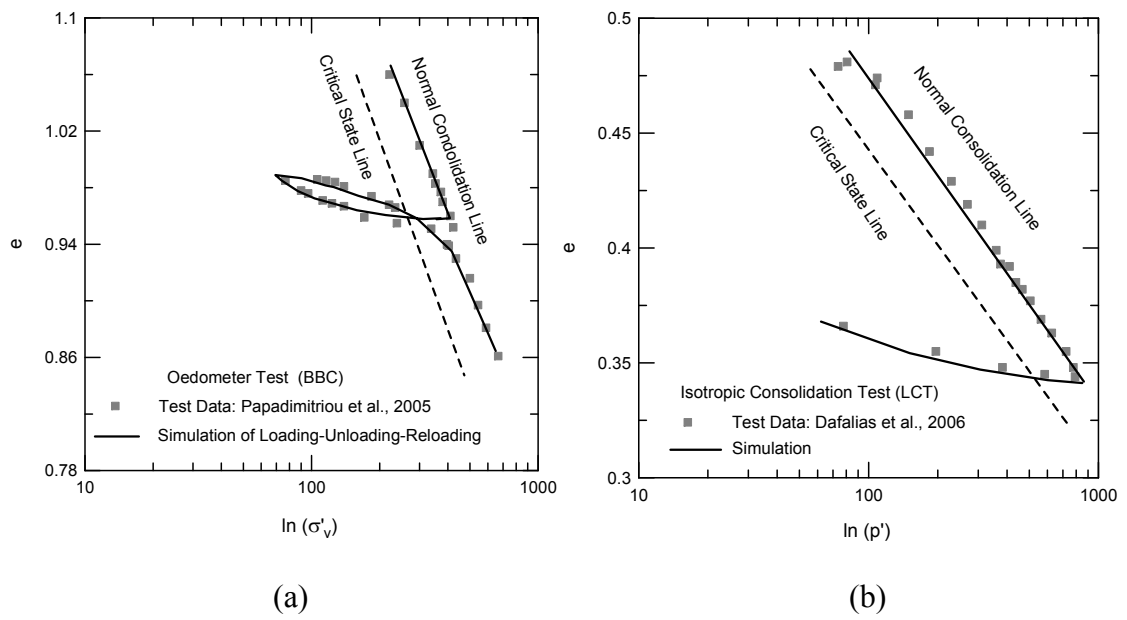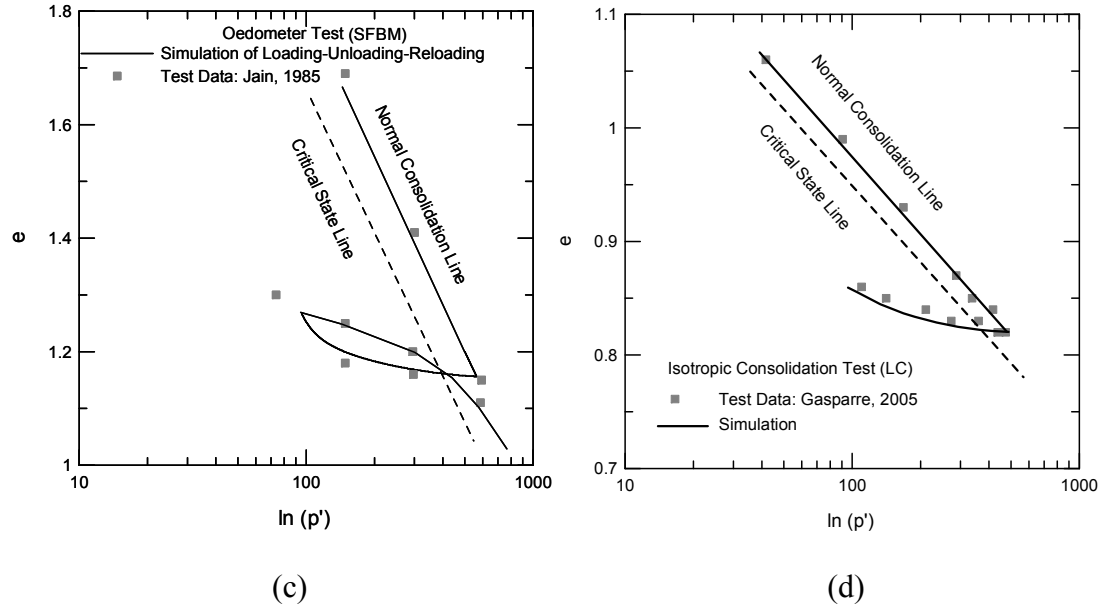
Figure 2.4 Consolidation behavior (horizontal axis in kPa) of (a) BBC, (b) LCT (c) SFBM and (d) LC

2.4.2. Undrained Shearing

Figure 2.5 and Figure 2.6 show the model simulation of undrained triaxial compression and extension after isotropic consolidation for BBC and LCT, respectively. For SFBM and LC, results of undrained triaxial compression tests after isotropic consolidation are presented in Figure 2.7 and Figure 2.8. Test data have been taken from Pestana *et al.* (2002) for BBC and Dafalias *et al.* (2006) for LCT. SFBM data is collected from Bonaparte (1982). Data for LC are taken from Gasparre (2005). The tests stopped at around 12% axial strain. We performed simulations for OCR values of 1, 4 and 8 for BBC; 1, 2, 4 and 10 for LCT; 1, 1.5, 2 and 3 for SFBM; and 1, 1.5 and 6 for LC. Figure 2.5(a) - Figure 2.8(a) present normalized deviatoric stress vs axial strain curves for BBC, LCT, SFBM and LC while Figure 2.5(b) - Figure 2.8(b) shows normalized deviatoric stress vs. normalized mean stress plot. Normalizations are performed with respect to the maximum axial stress at the end of consolidation ($\sigma'_{a,max}$). The model simulations are in good agreement with the data for BBC and LC. For LCT, it slightly overpredicts the stresses at higher OCR values. At OCR = 1, we capture the undrained softening behavior

accurately. At OCR = 2 for LCT, we observe the phase transformation behavior in model simulation. Figure 2.9 compares the normalized deviatoric stress vs axial strain response of isotopic triaxial compression obtained from model simulation with the true triaxial test results (triaxial compression condition) obtained from Kirkgard and Lade (1991).
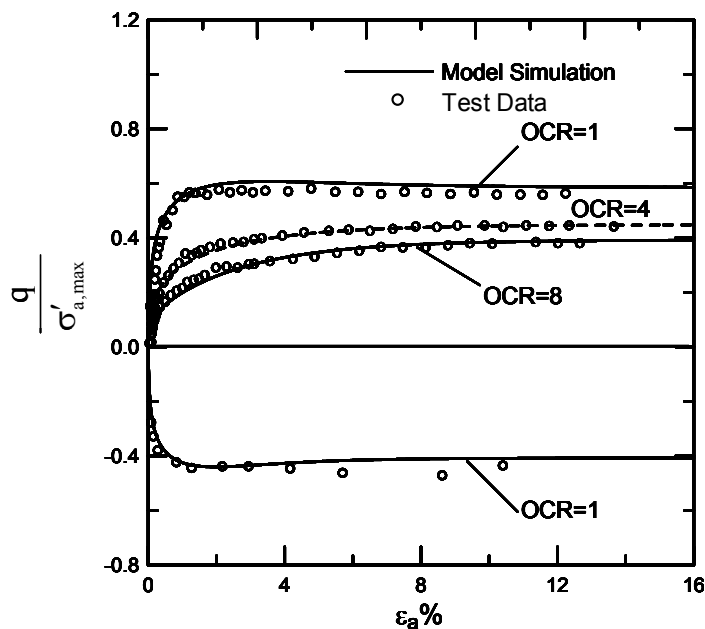
(a)
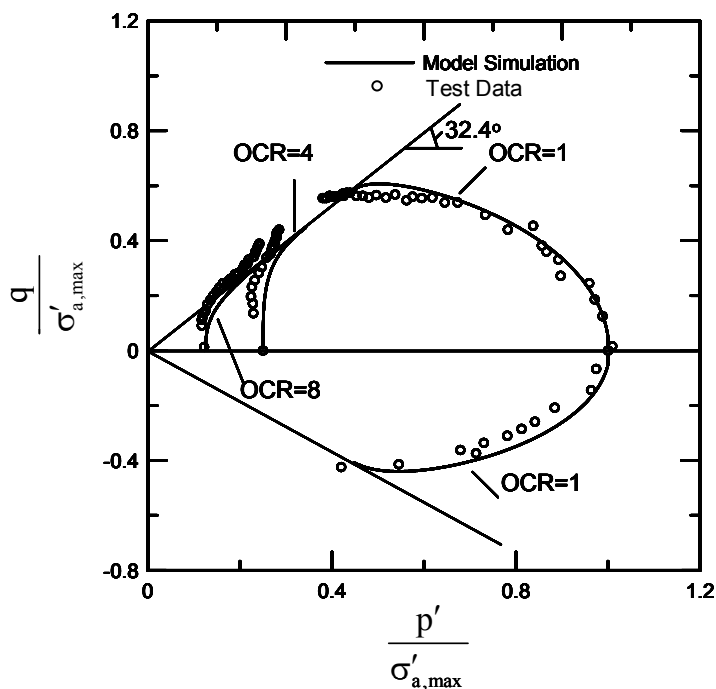
(b)

Figure 2.5 Undrained triaxial compression and extension after isotropic consolidation for BBC for OCR = 1, 4 and 8 (test data: Pestana *et al.* 2002): (a) stress-strain response and (b) stress path

(a)

Figure 2.6 Undrained triaxial compression and extension after isotropic consolidation for LCT for OCR = 1, 2, 4 and 10 (test data: Dafalias *et al.* 2006): (a) stress-strain response and (b) stress path

(a)

(b)

Figure 2.7 Undrained triaxial compression and extension after isotropic consolidation for SFBM for OCR = 1, 1.5 and 3 (test data: Bonaparte 1982): (a) stress-strain response and (b) stress path

(a)

(b)
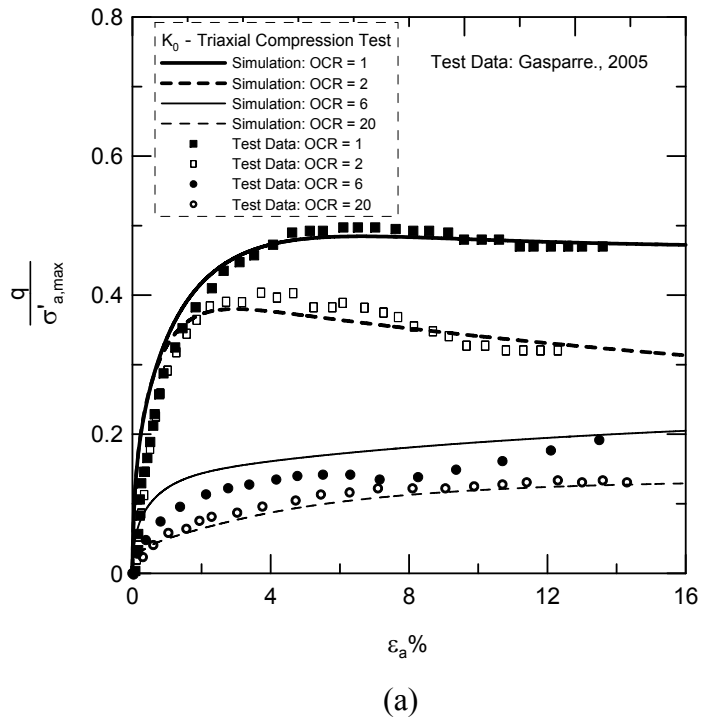
Figure 2.8 Undrained triaxial compression after isotropic consolidation for LC for OCR = 1, 2, 6 and 20 (test data: Gasparre 2005) (a) stress-strain response and (b) stress path
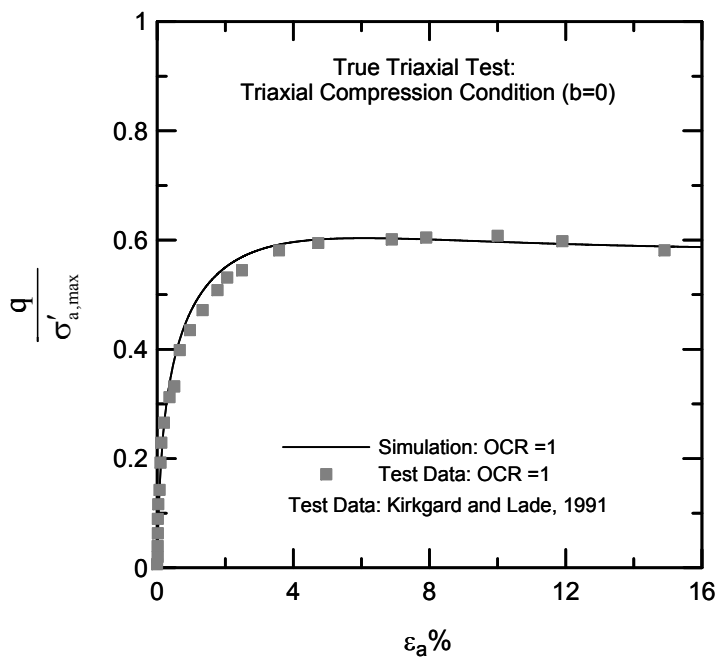
(a)
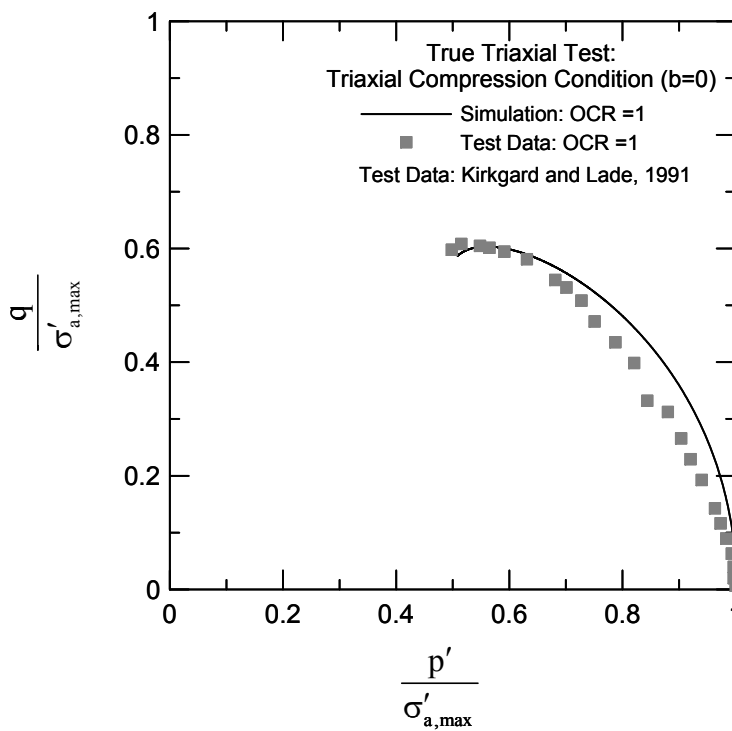
(b)

Figure 2.9 True triaxial compression after isotropic consolidation for SFBM for OCR = 1
(test data: Kirkgard and Lade 1991): (a) stress-strain response and (b) stress path

Figure 2.10 - Figure 2.13 compare the model predictions and experimental data for undrained triaxial compression and extension tests after K_0 consolidation for BBC, LCT, SFBM and LC. Figure 2.10(a) - Figure 2.13(a) show the normalized deviatoric stress vs axial strain plot while Figure 2.10(b) - Figure 2.13(b) show the normalized deviatoric stress vs normalized mean stress plot. Normalizations are performed with respect to maximum axial stress ($\sigma'_{a,max}$). K_0 values are decided based on the one-dimensional consolidation tests. The deviatoric stress reaches critical state at around 12% axial strain for all the OCR values. This is in accordance with the literature. In this model, we use the same M_c value for isotropic and K_0 cases. This causes slight underprediction of stress for all OCR values in the case of BBC and LCT.

(a)

(b)
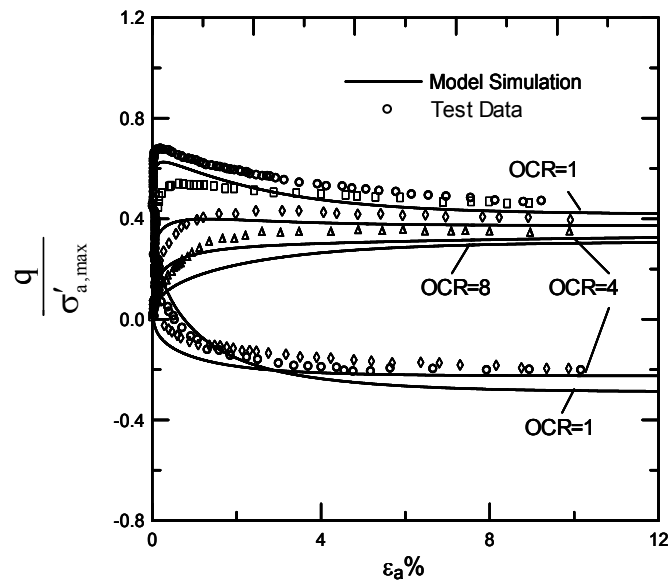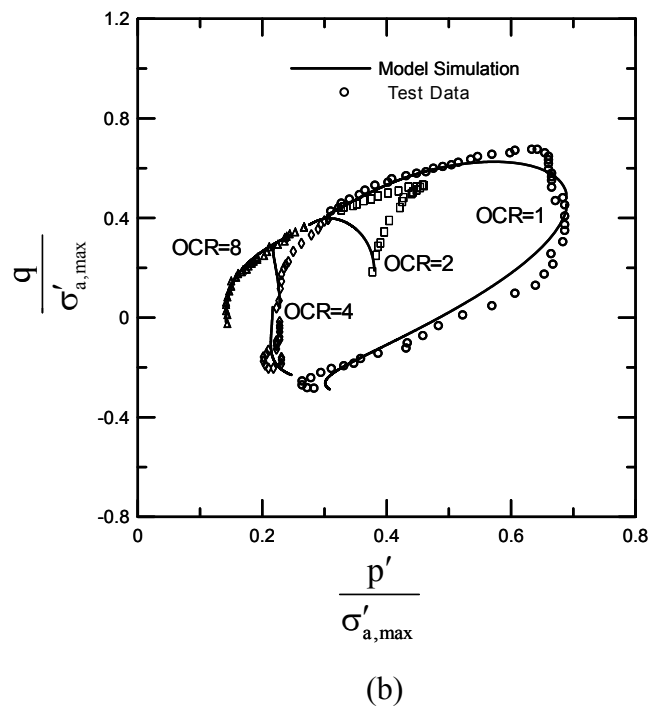
Figure 2.10 Undrained triaxial compression and extension after K_0 consolidation for BBC for OCR = 1, 2, 4 and 8 (Papadimitriou *et al*. 2005): (a) stress-strain response and (b) stress path

(a)

(b)
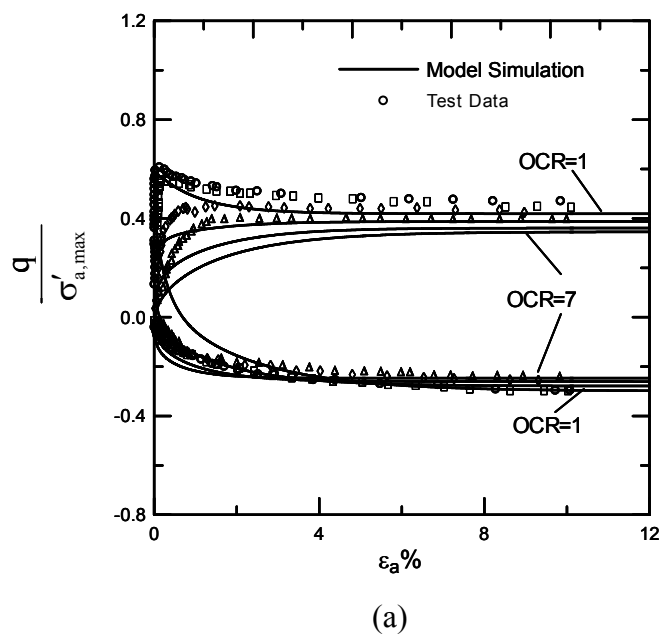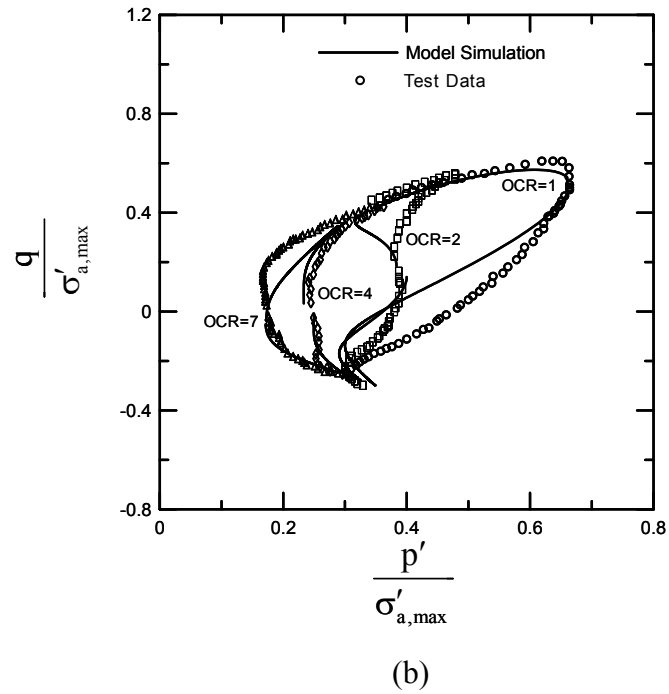
Figure 2.11 Undrained triaxial compression and extension after K_0 consolidation for LCT for OCR = 1, 2, 4 and 7 (test data: Dafalias *et al.* 2006) (a) stress-strain response and (b) stress path

(a)

(b)
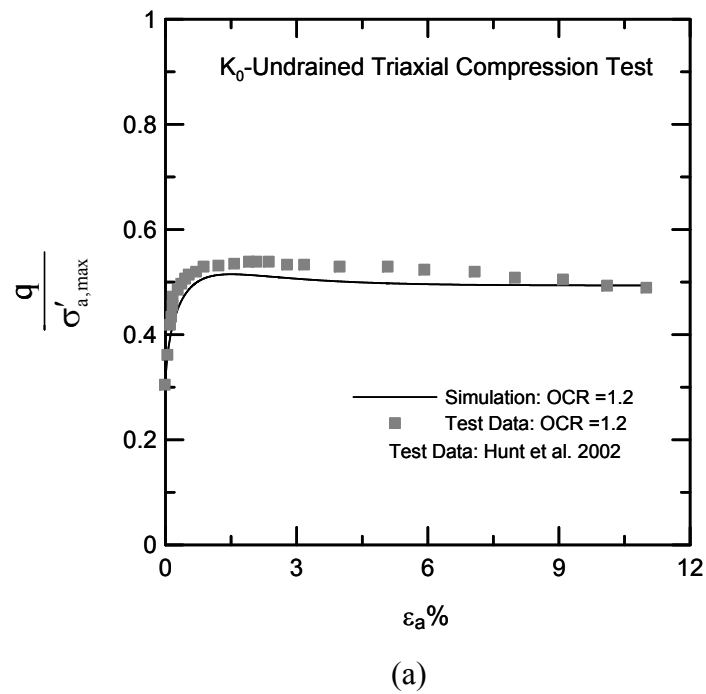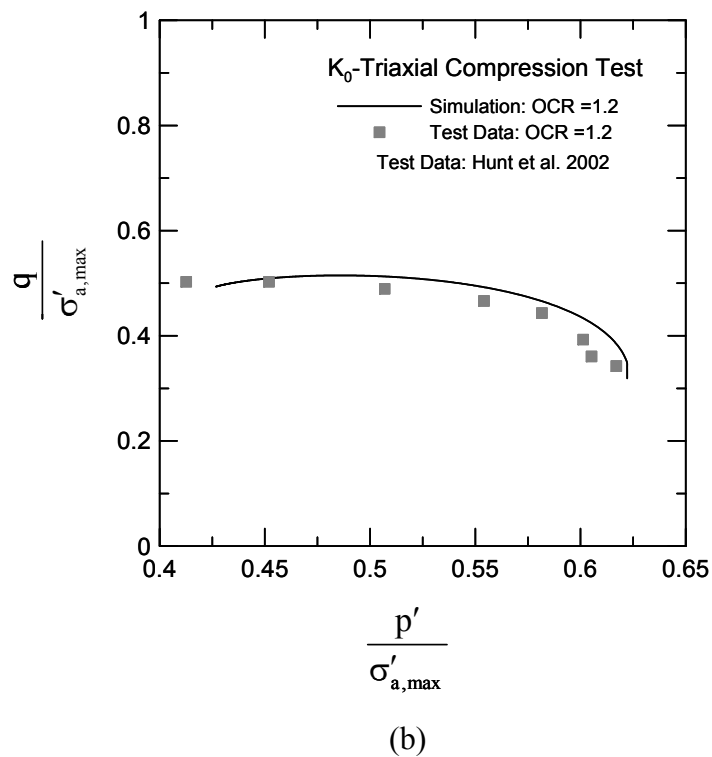
Figure 2.12 Undrained triaxial compression after K_0 consolidation for SFBM for OCR = 1 (test data: Hunt et al. 2002): (a) stress-strain response and (b) stress path
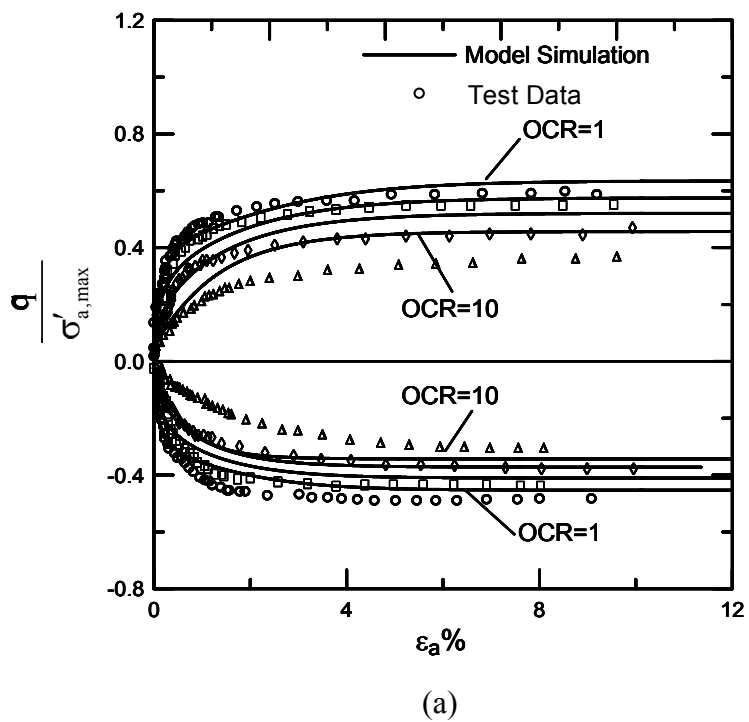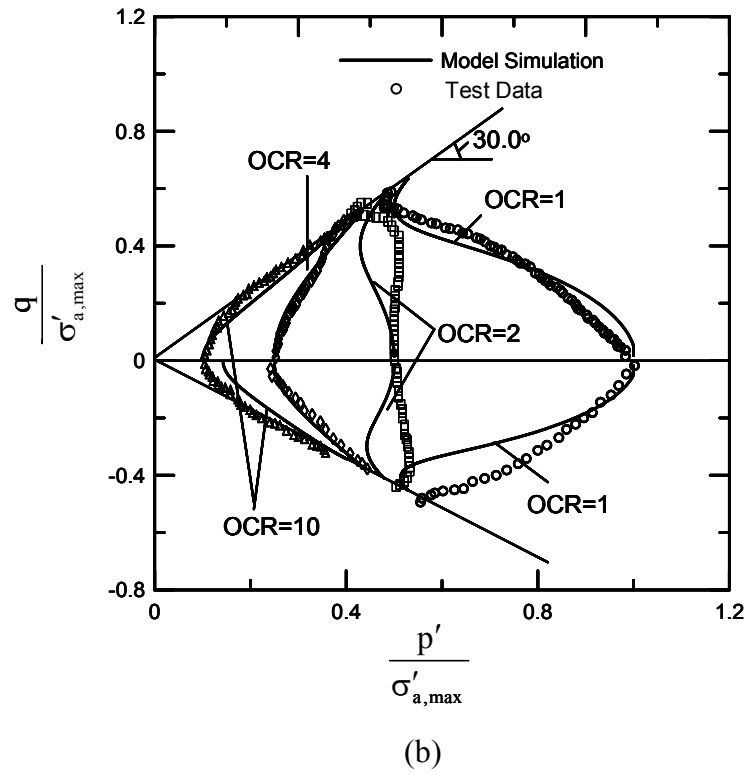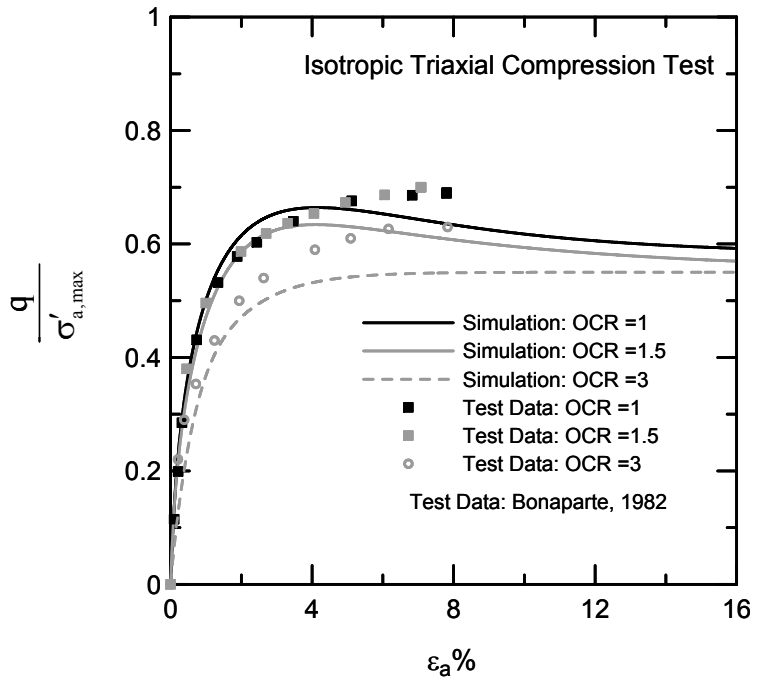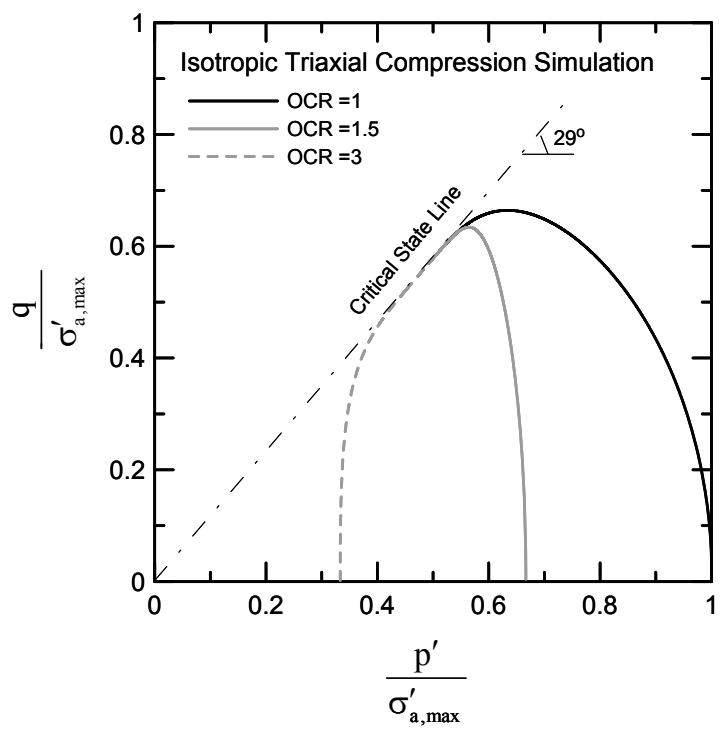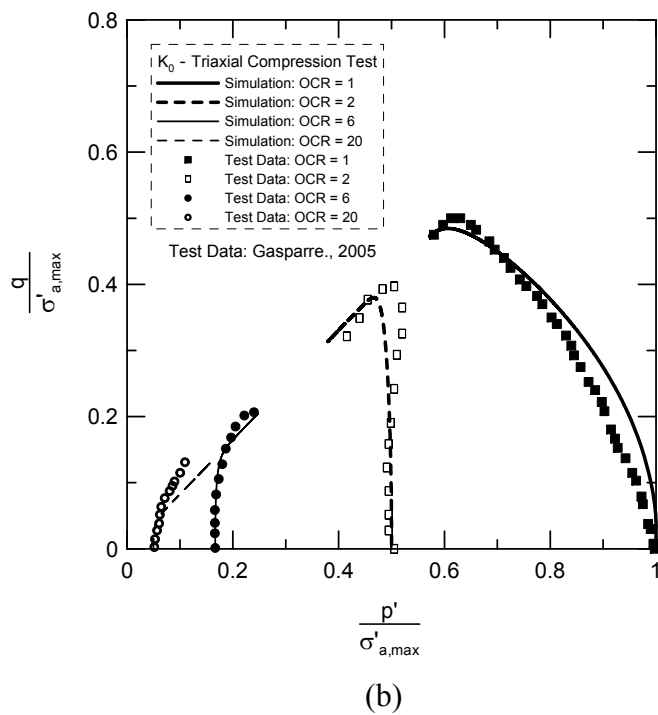

(a)

(b)
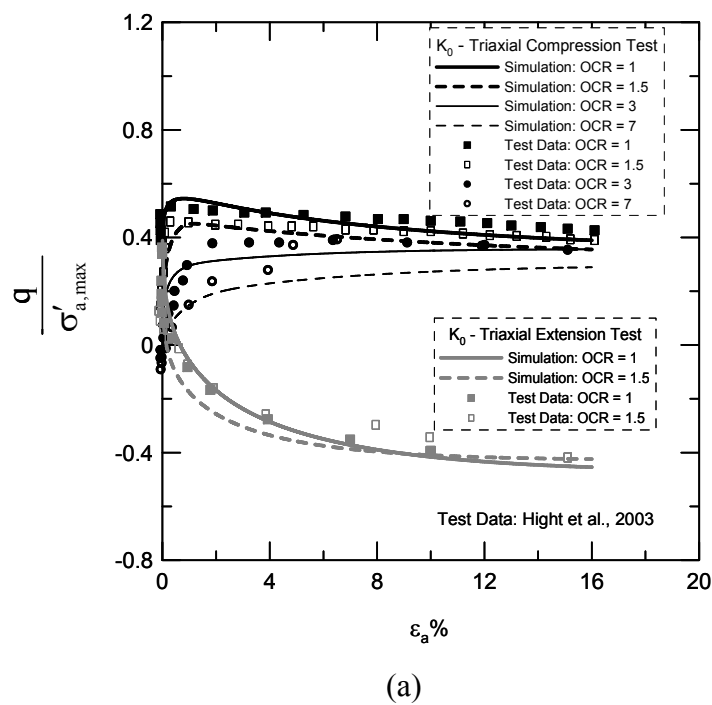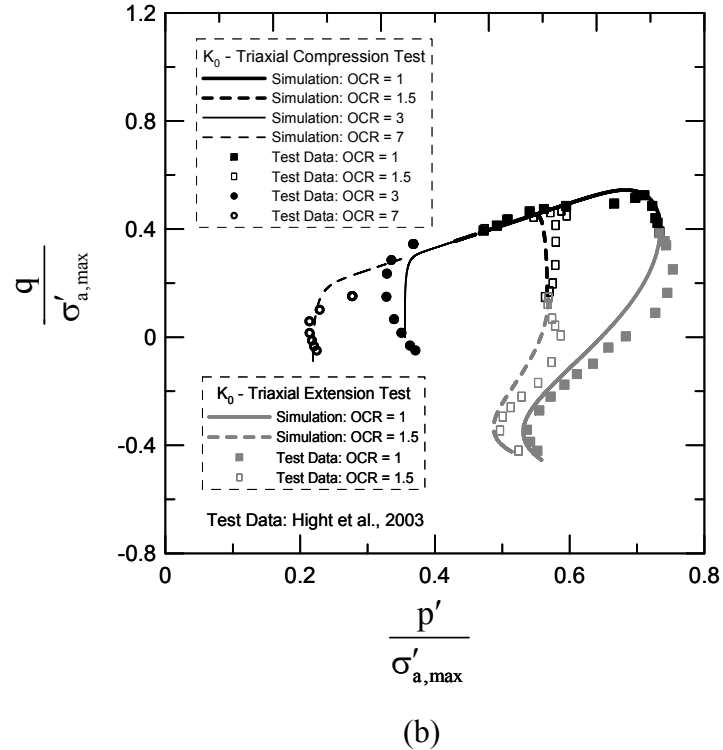
Figure 2.13 Undrained triaxial compression and extension after K_0 consolidation for LC for OCR = 1, 1.5, 3 and 7 (test data: Hight *et al*. 2003): (a) stress-strain response and (b) stress path

2.4.3. Undrained Simple Shear

Figure 2.14(a) through Figure 2.16(a) show the normalized shear stress vs shear strain plot for BBC, SFBM and LC, respectively, while Figure 2.14(b) to Figure 2.16(b) present normalized shear stress vs normalized normal stress plot for BBC, SFBM and LC. The normalizations are performed with respect to vertical preconsolidation pressure $\sigma'_{a,max}$. The figures demonstrate the ability of the model to capture the mechanical response in multi axial stress situations. This test is very important and highly desirable for proper simulation of boundary-value problems in geotechnical engineering. Test data has been taken from Pestana *et al.* (2002) for BBC, Rau (1999) for SFBM and Hight *et al.* (2003) for LC. The tests stopped at around 12% shear strain. Model simulations show a slight overprediction of stresses at OCR = 1 and OCR = 8 for BBC. The model predicts b =

0.429 during simple shear which resulting in θ = 26°. We allow the simulation to soften towards residual strength for SFBM. Softening takes place at constant σ'_v.
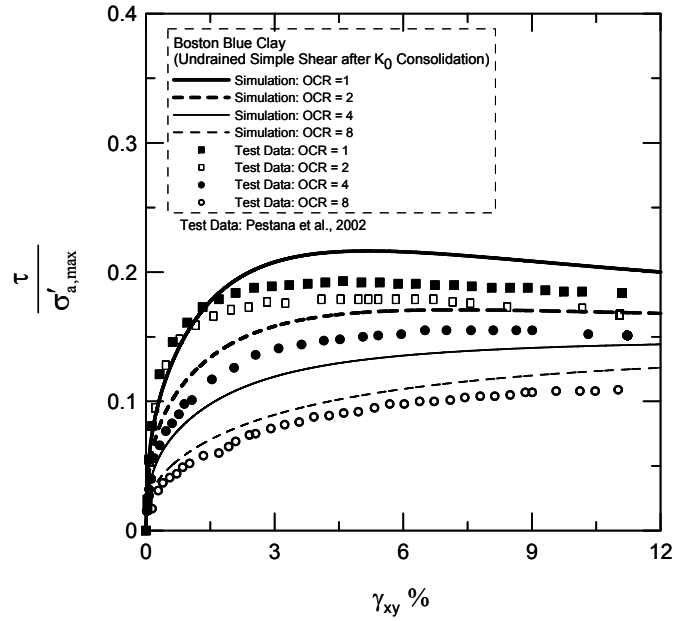
(a)
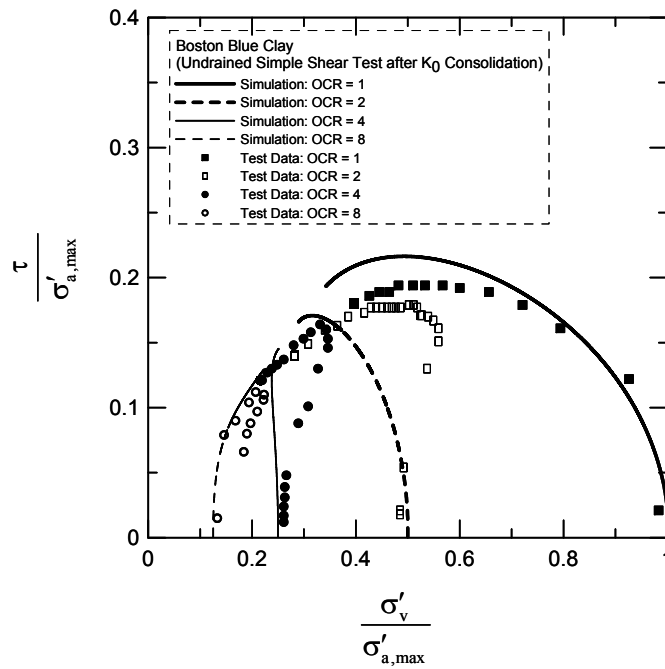
(b)

Figure 2.14 Undrained simple shear after K_0 consolidation for BBC for OCR = 1, 2, 4 and 8 (test data: Pestana *et al*. 2002): (a) stress-strain response and (b) stress path

(a)

(b)
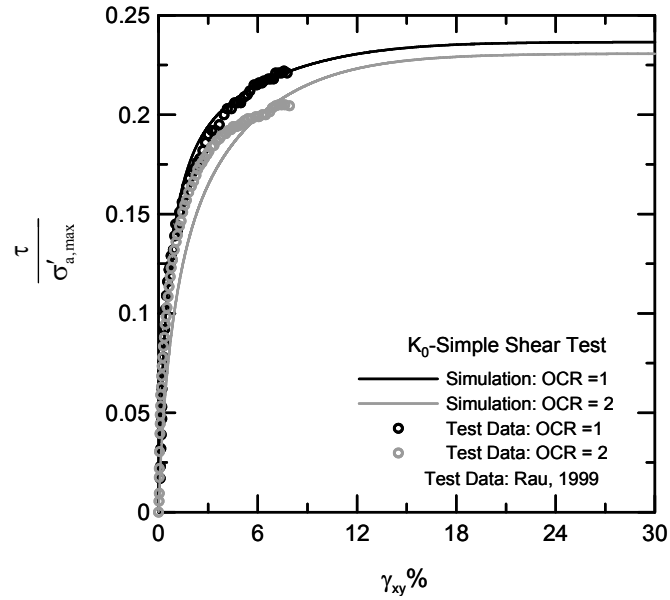
Figure 2.15 Undrained simple shear after K_0 consolidation for SFBM for OCR = 1 and 2
(test data: Rau 1999): (a) stress-strain response and (b) stress path
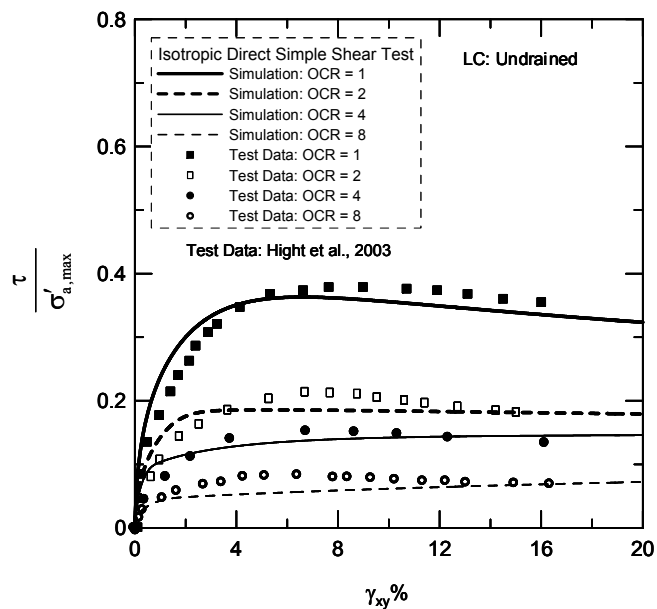
(a)
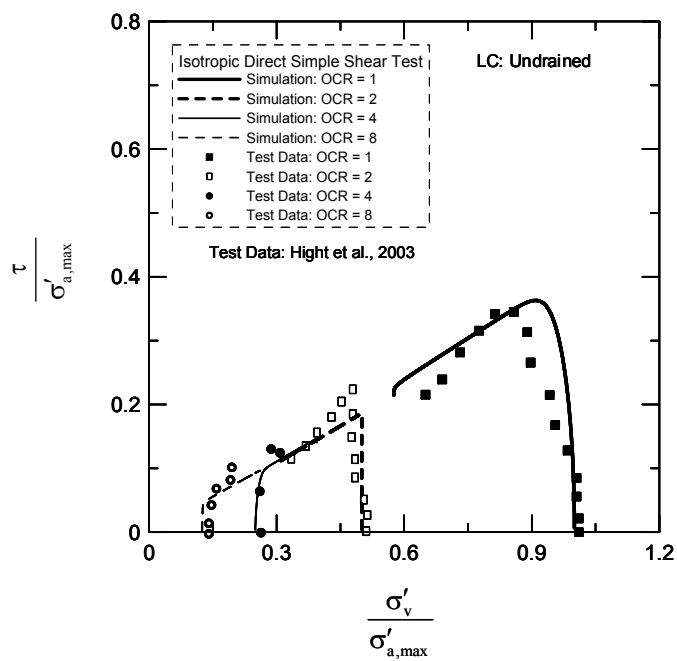
(b)

Figure 2.16 Undrained simple shear after K_0 consolidation for LC for OCR = 1, 2, 4 and 8 (test data: Hight *et al.* 2003): (a) stress-strain response and (b) stress path

2.4.4. Residual Behavior

We determine the model parameters controlling the residual behavior of clay for SFBM and LC. We obtain the ring shear test results for SFBM from Meehan (2006). The minimum residual friction angle for SFBM based on these tests is 16.2°. The residual behavior of LC is validated using the ring shear test results by Bishop *et al.* (1971), for both Brown and Blue LC. In the case of Brown London Clay, the residual friction angle decreases with increasing normal stress on the shear plane. The minimum residual friction angle for Brown London clay is 7.5°. However, for Blue London clay, the angle is constant: 9.4 degrees. Figure 2.17(a) and Figure 2.18(a) show the decrease of the residual friction angle for SFBM and brown LC respectively with increasing normal stress on the shear plane. Figure 2.17(b) and Figure 2.18(b) show the variation of M_r/M_{cc} ratio with shear displacement for Blue LC.
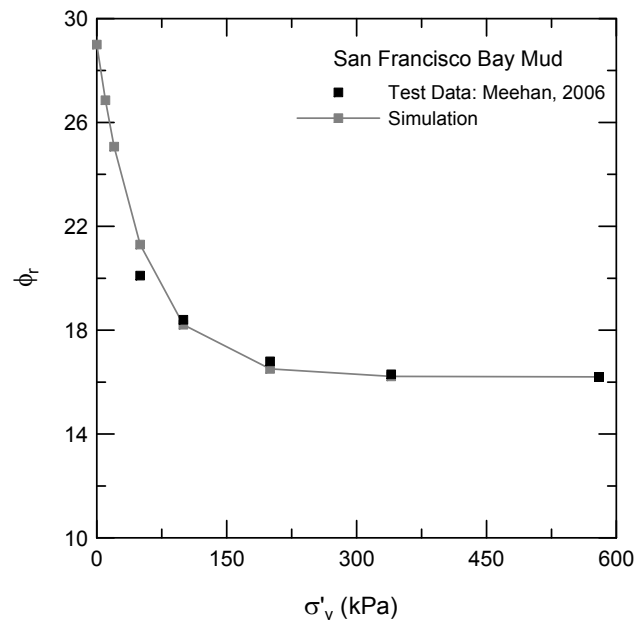
(a)
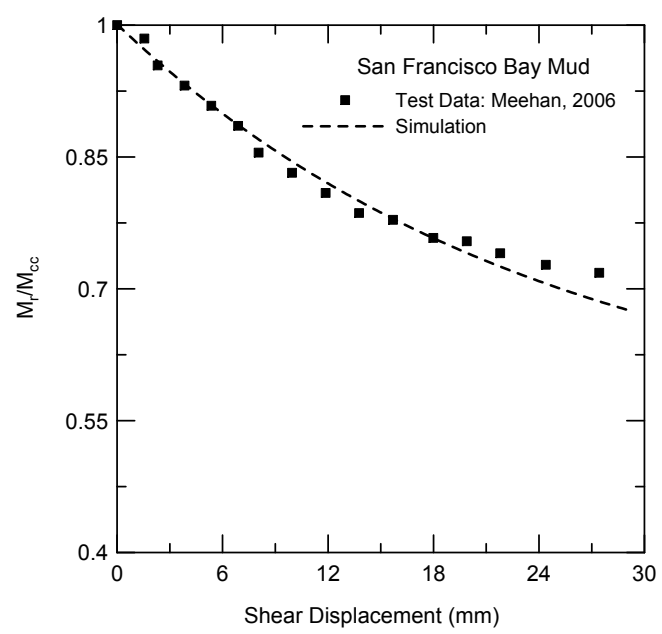
(b)

Figure 2.17 Comparison of model simulation and experimental data for SFBM at residual state

(a)

(b)
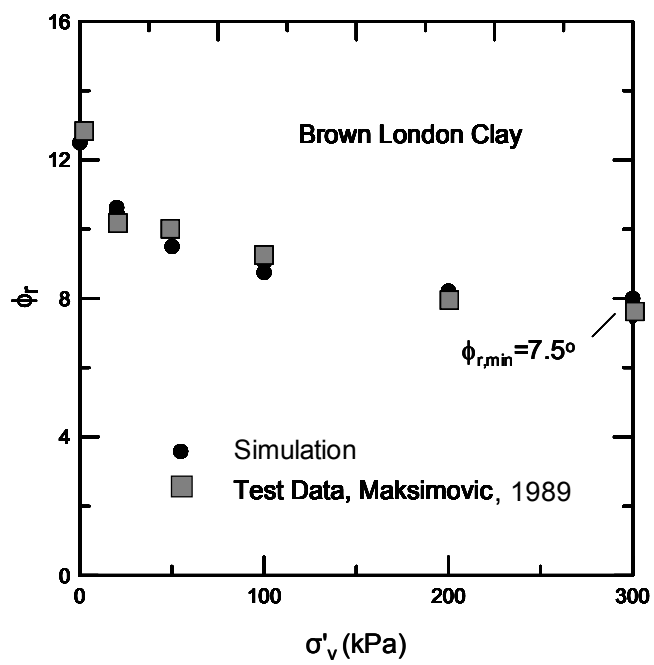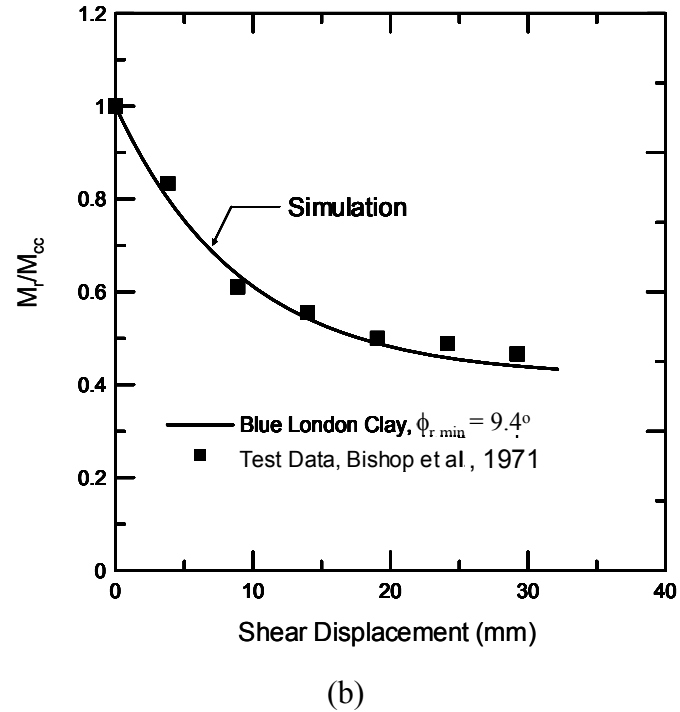
Figure 2.18 Comparison of model simulation and experimental data for London Clay at residual state

2.5. Model Simulations for Rate-Independent Behavior of Clay

2.5.1. Loading Paths for Undrained Triaxial Compression Test

We simulate strain-rate-dependent simple element tests of undrained triaxial compression and undrained simple shear tests using MATHCAD for BBC, SFBM and LC. We plot the stress-strain and stress path response obtained from undrained triaxial compression tests after K_0 consolidation in Figure 2.19. Figure 2.19(a) and Figure 2.19(b) show the plots of normalized deviatoric stress ($q/\sigma'_{a,max}$) vs. deviatoric strain ε_q (%) and normalized deviatoric stress ($q/\sigma'_{a,max}$) vs. normalized mean stress ($p'/\sigma'_{a,max}$) at OCR = 1 for different strain rates. The normalization is performed with respect to the maximum vertical effective stress, $\sigma'_{a,max}$ at the end of consolidation. The figures show that, with increasing strain rate the peak deviatoric stress increases. In this constitutive model, the strength at

critical state increases with increasing strain-rate. The rate effect is still visible at large deviatoric strain values (16%).
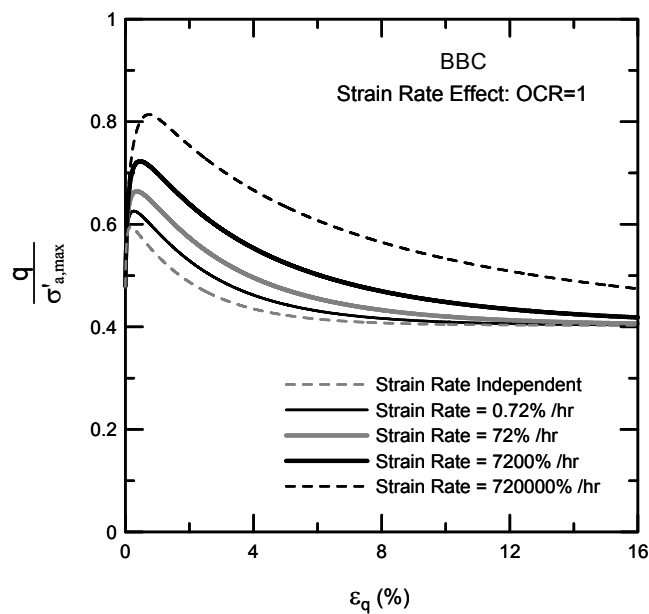
(a)
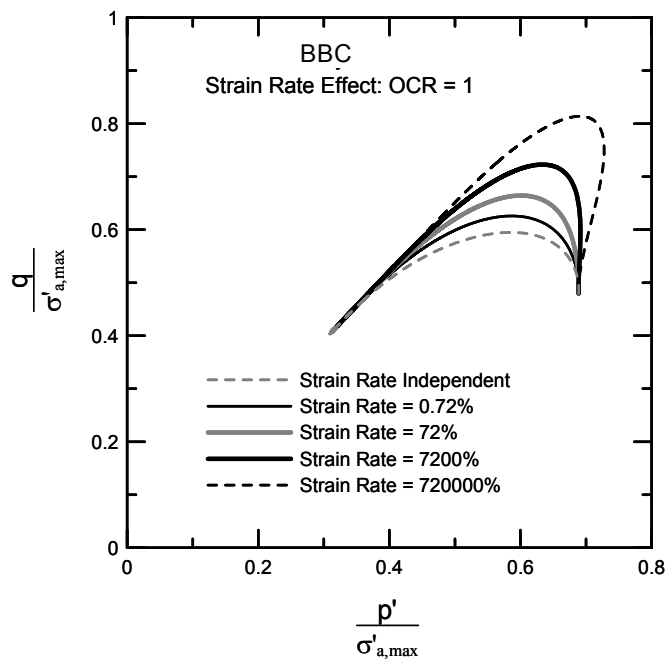
(b)

Figure 2.19 Undrained triaxial compression after K_0 consolidation for BBC for OCR = 1:
(a) stress-strain plot and (b) stress-path

Figure 2.20 and Figure 2.21 show the results of triaxial compressions tests after isotropic consolidation for OCR values 1 and 2 respectively. Figure 2.20 (a) and Figure 2.20(b) show the plots of normalized deviatoric stress ($q/\sigma'_{a,max}$) vs. deviatoric strain ε_q (%) and normalized deviatoric stress ($q/\sigma'_{a,max}$) vs. normalized mean stress ($p'/\sigma'_{a,max}$) respectively at OCR = 1 at different strain-rates. Both the peak and critical-state strength increase with increasing strain rate, though the rate of strength gain with increasing strain rate is much higher at peak than at critical state. The peak and critical-state strength gains in the rate-dependent cases as compared to the rate-independent loading are clearly visible in the plots. We observe that the dilatancy of the sample increases with increasing strain rate. There may be a possibility that under undrained shearing at high strain rate, clay particles form clusters which try to climb over each other during shearing and the sample increases in volume at high strain rate. As a result, at high strain rate, clay behavior could change from contractive to dilative, as suggested by the model.

(a)

(b)
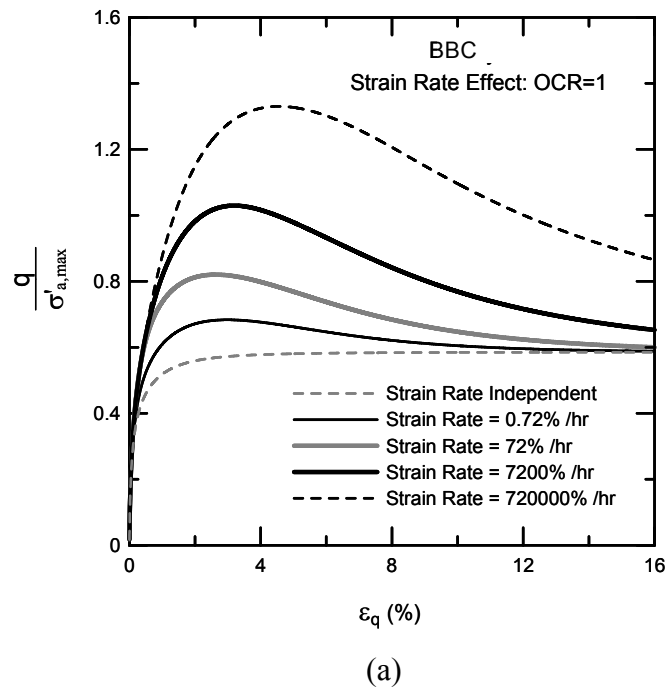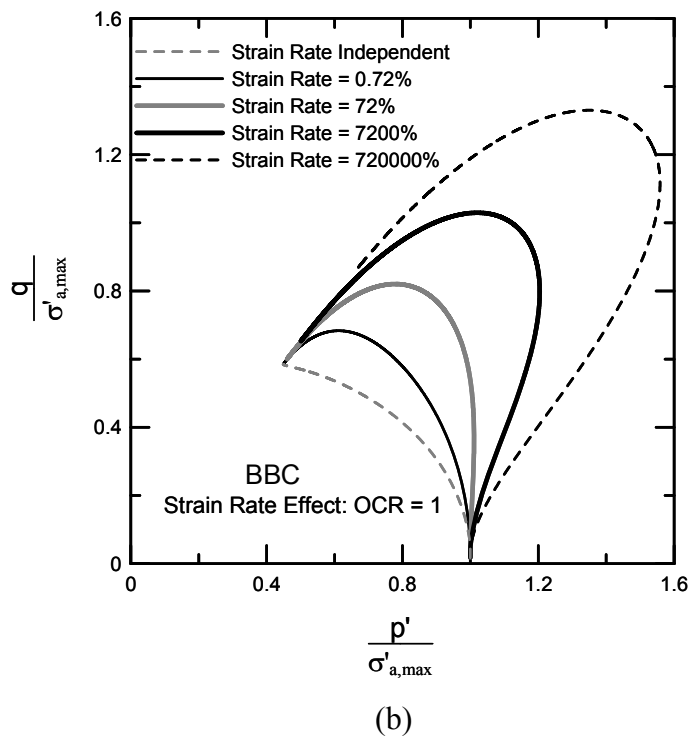
Figure 2.20 Undrained triaxial compression after isotropic consolidation for BBC for OCR = 1: (a) stress-strain plot and (b) stress-path

(a)

(b)
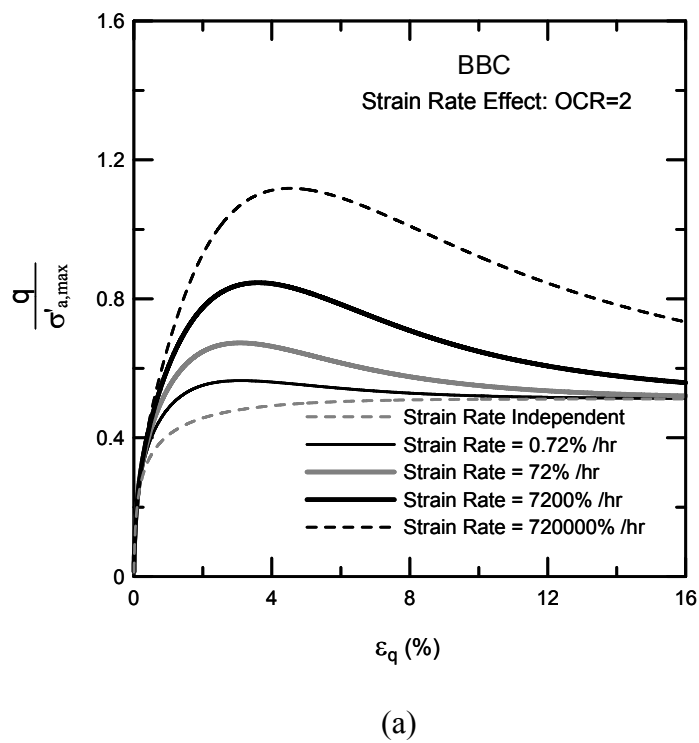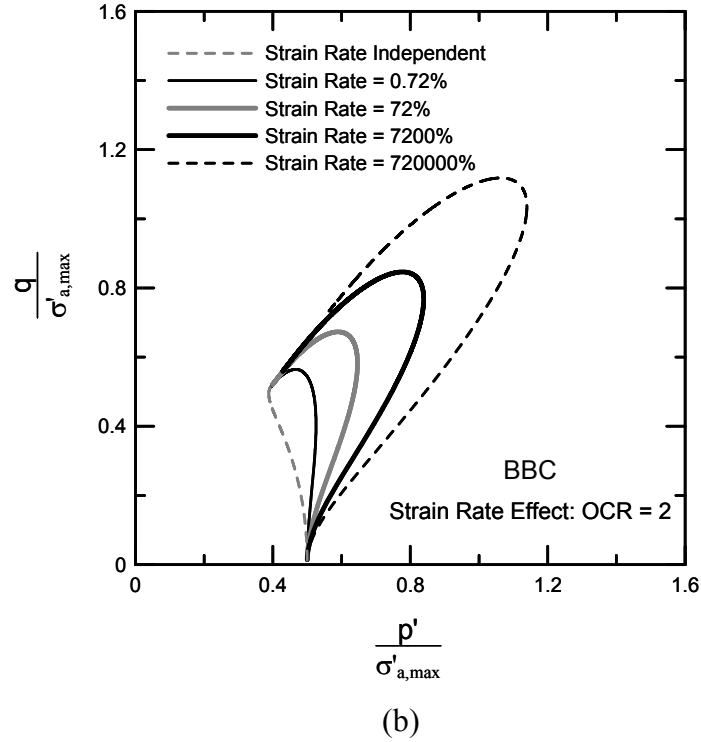
Figure 2.21 Undrained triaxial compression after isotropic consolidation for BBC for OCR = 2: (a) stress-strain plot and (b) stress-path

2.5.2. Loading Paths for Simple Shear Test

The model successfully simulates the mechanical response of soil in multi-axial stress situations. We simulate anisotropically consolidated (K_0-consolidated) undrained simple shear tests. Figure 2.22 and Figure 2.23 demonstrate the ability of the model to capture multi-axial stress situations. Figure 2.22(a) shows normalized shear stress ($\tau/\sigma'_{v,NC}$) vs. shear strain γ_{xy} (%) for undrained simple shear tests at OCR = 1 for BBC, while Figure 2.22(b) shows normalized shear stress ($\tau/\sigma'_{v,NC}$) vs. normalized normal stress ($\sigma'_v/\sigma'_{v,NC}$) at OCR = 1. The normalization is performed with respect to the maximum vertical stress at the end of consolidation for normally consolidated samples ($\sigma'_{v,NC}$). Plot for OCR = 4 is depicted in Figure 2.23. For all the cases, the peak stress increases with increasing strain rate. We also observe in the stress path plots that higher strain rate increases the dilatancy of the clay.
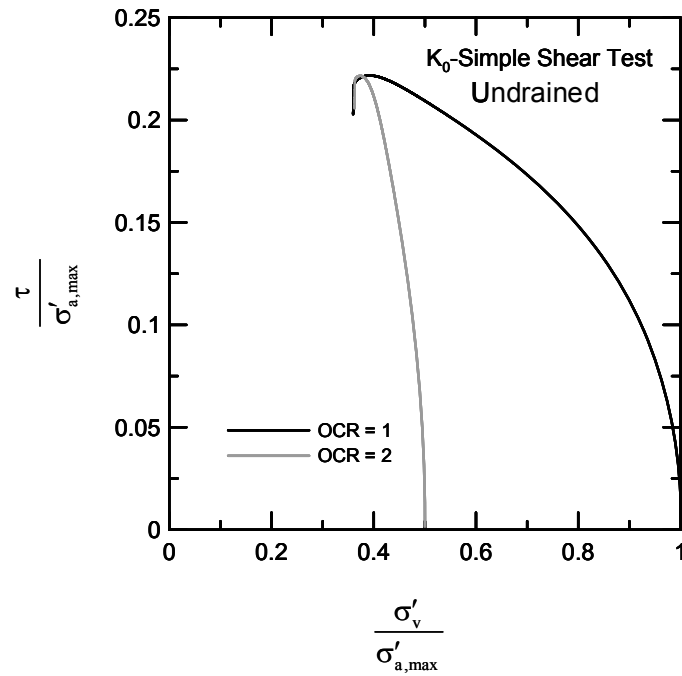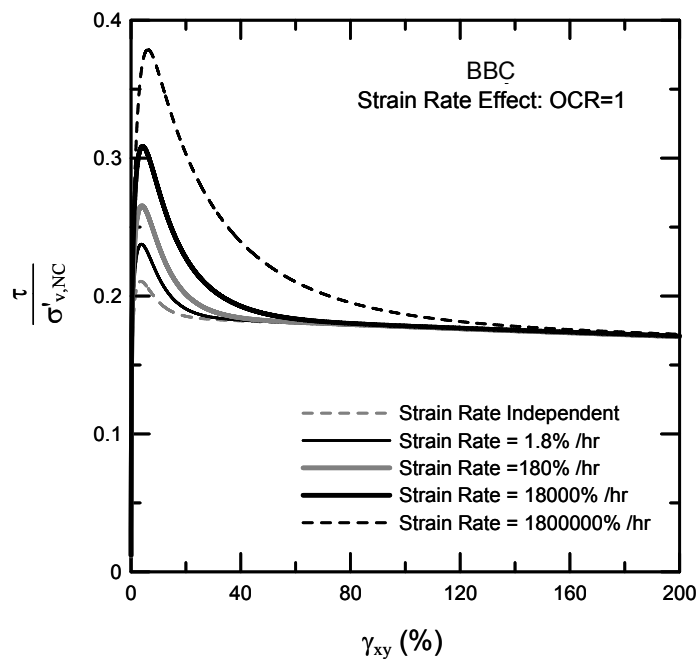
(a)
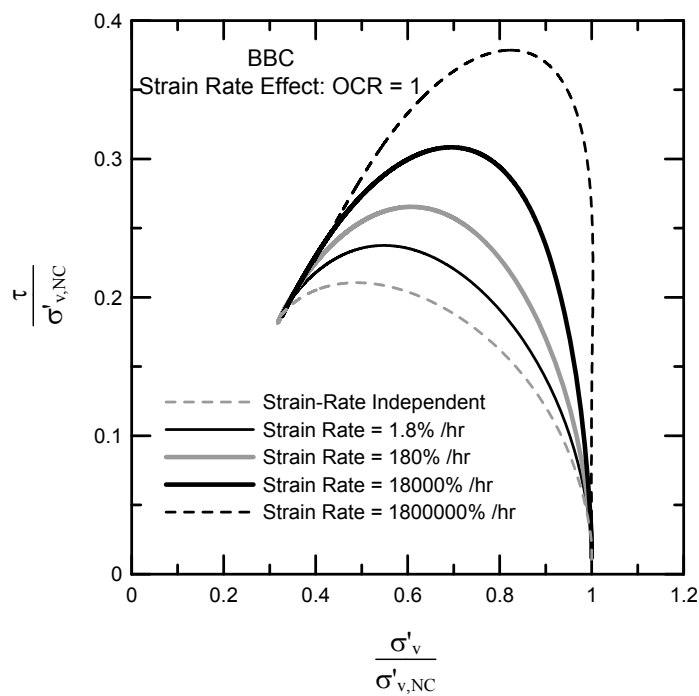
(b)

Figure 2.22 Undrained simple shear tests after K_0 consolidation for BBC for OCR=1: (a) stress-strain plot and (b) stress-path
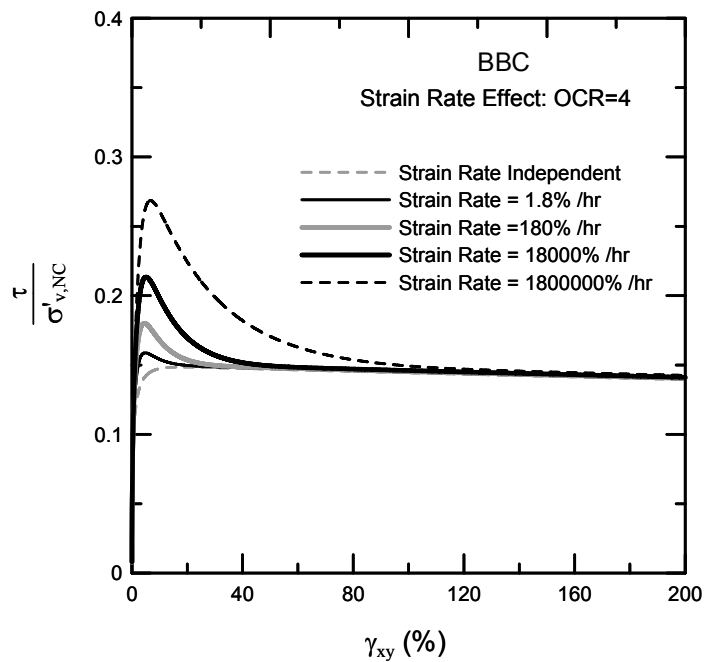
(a)
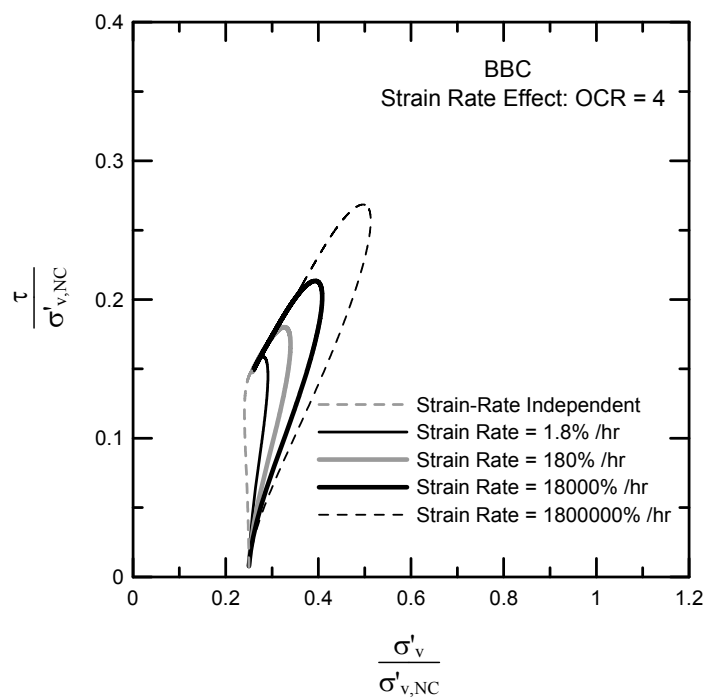
(b)

Figure 2.23 Undrained simple shear tests after K_0 consolidation for BBC at OCR = 4: (a) stress-strain plot and (b) stress-path

CHAPTER 3. THE FINITE ELEMENT METHOD APPLIED TO THE SHAFT
RESISTANCE PROBLEM

3.1. <u>Introduction</u>

Previous numerical studies, aimed to model the installation of a displacement pile in clay, used either undrained cylindrical cavity expansion theory (Carter *et al*. 1979) or the strain path method (Baligh 1985). Randolph *et al*. (1979) simulated the installation of a displacement pile in clay by one-dimensional undrained expansion of a cylindrical cavity and investigated the changes in the stresses and pore pressure within the soil during and after the installation. Excess pore pressure generated during the undrained cylindrical cavity expansion (which was intended to model pile installation) was assumed to dissipate through a one-dimensional flow in the radial direction outward from the pile. A work-hardening, elasto-plastic model (similar to the modified cam clay model) was used to represent the constitutive behavior of the soil.

The strain path method (SPM) provides an analytical framework to evaluate the strains associated with quasi-static, undrained penetration in saturated clays. This method assumes the deep penetration in saturated clays to be a fully-constrained process (no volume change); the deformations and strains developed during the penetration of a foreign object are considered to be independent of the shear resistance offered by the soil. Whittle and Sutabutr (1999) used the SPM to derive the end-of-installation stresses and pore pressure around a displacement pile installed in saturated clay. A one-dimensional finite element (FE) model was then used to investigate the radial dissipation of generated excess pore pressure. The MIT-E3 model (Whittle and Kavvadas 1994, Whittle *et al*. 1994) was used to represent the nonlinear soil behavior.

In this chapter we describe different aspects of the one-dimensional (1-D) finite element (FE) model that we use to model installation, setup and loading of a pile jacked in saturated clay. We consider pile jacking in clay to be a fully undrained process. At the

end of installation and before simulation of pile loading (either from a static pile load test or from the superstructure), we allow the corresponding rest period, during which excess pore pressures will partially or fully dissipate. Although our analysis focus on jacked piles, we believe that the conclusions in general apply to driven piles; although some deviations in shaft resistance values are possible, they are not expected to be large.

3.2. Mathematical Formulation

We perform 1-D finite element analysis (FEA) to model the jacking and the subsequent loading of a cylindrical pile jacked in saturated clay. The FEA involves three distinct stages: (i) pile installation (jacking), (ii) dissipation of excess pore pressure generated during installation, and (iii) loading of the pile. These stages were also recognized by several other researchers in studies related to the shaft capacity of displacement piles in clay (Steenfelt *et al*. 1980, Bond and Jardine 1991, Azzouz *et al*. 1990, Lehane *et al*. 1994, Lee *et al*. 2004). The rate-dependent, two-surface plasticity-based constitutive model described in Chapter 2 of this report is used in the FEA to represent the constitutive behavior of clay.

3.2.1. Simulation of Pile Jacking in Clay and Pile Loading

Jacking of a pile into the ground is assumed to load the soil mass through a combination of cavity expansion and vertical shearing. Figure 3.1 shows schematically the different stages involved in the analysis of a pile monotonically jacked in clay. This figure also shows the evolution of normal (radial) stress σ_r, vertical shear stress τ_z and excess pore pressure u in a soil element adjacent to the pile shaft (Element A). Figure 3.1(a) shows Element A subjected to *in situ* stresses (excess pore pressure and vertical shear stress acting on the vertical face of the element at this stage are zero).

Stage 1 (Figure 3.1b) corresponds to the penetration of the pile into the soil mass and is modeled as a sequential combination of two phases: the undrained cavity expansion (CE) phase and the phase of "primary shearing". The first phase (i.e., CE) represents the creation of a cylindrical space (to be occupied by the pile) within the

ground as the pile tip pushes the soil away from the path of the pile. The conical area shown in Figure 3.1 is either a conical tip fitted to the pile or the "rigid" tapered cone predicted by bearing capacity theory in the case of a rough base. The soil in the "rigid" tapered cone is in a nearly elastic state. The cylindrical cavity expansion stops when the cavity radius becomes equal to the pile radius, i.e., as the shoulder (base) of the cone clears Element A (Figure 3-1b). At the end of CE, the normal stress σ_r acting on the pile-soil interface reaches a limiting value p_L at the same time as the excess pore pressure takes a value u_{CE}. The vertical shear stress on the pile shaft (vertical side of the Element A) remains zero throughout this phase. The cavity expansion phase is followed by vertical shearing along the shaft wall ("primary shearing" phase) until the limit shear stress τ_l is reached along the pile shaft. The soil element adjacent to the pile shaft is expected to reach the residual shear strength at this state. At the end of the "primary shearing" phase the total normal stress acting on the pile shaft is reduced from p_L to σ_{r1}.

(a)

(b)
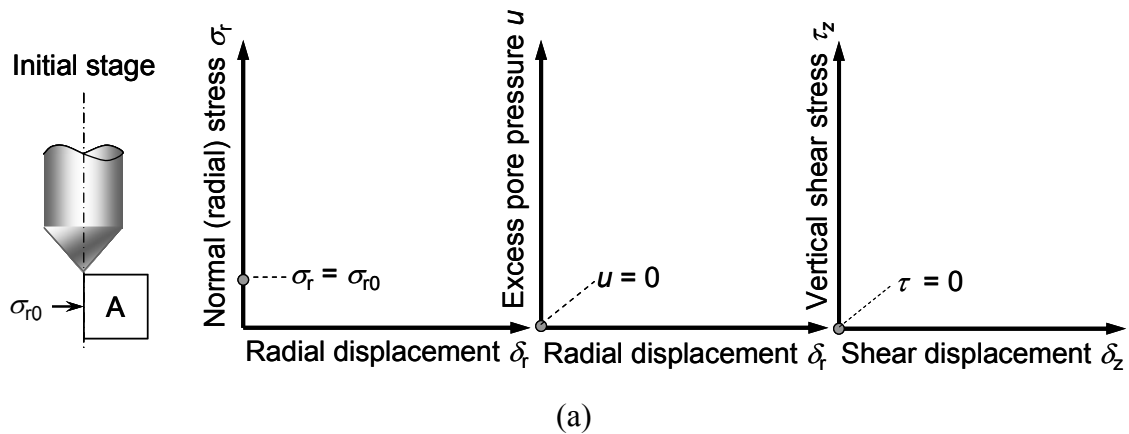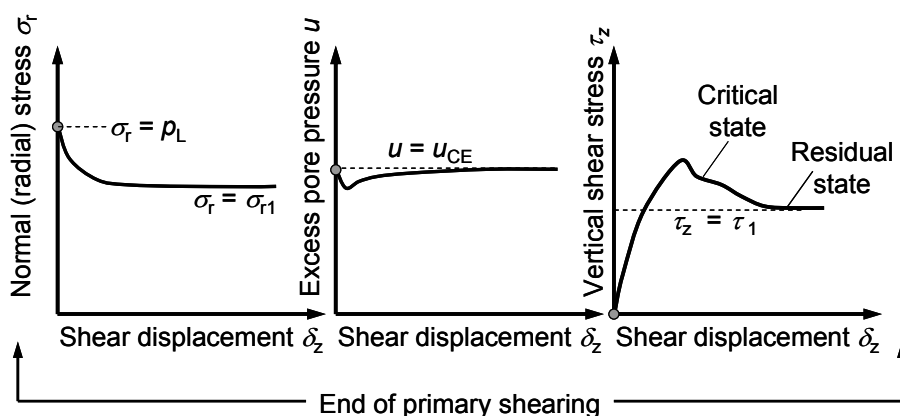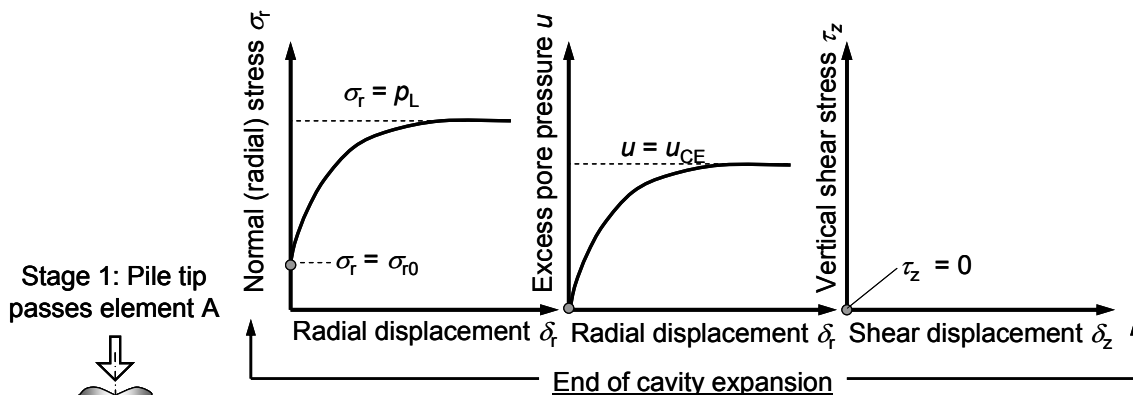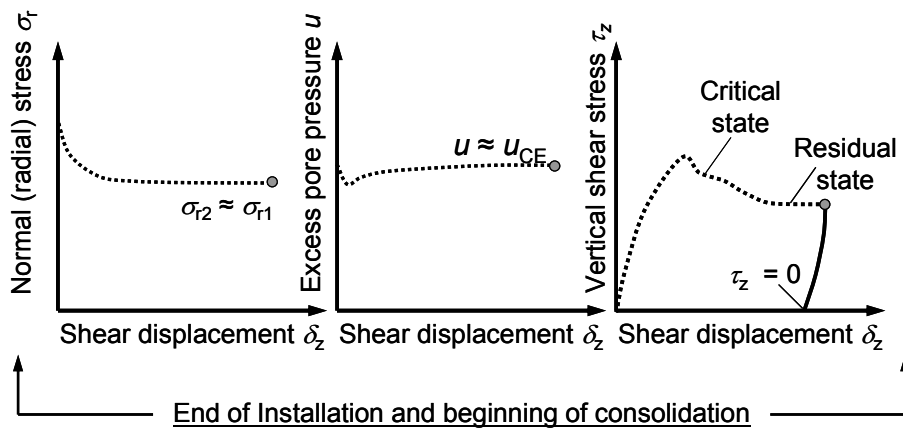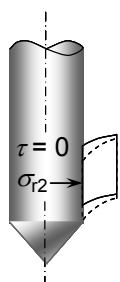
(c)
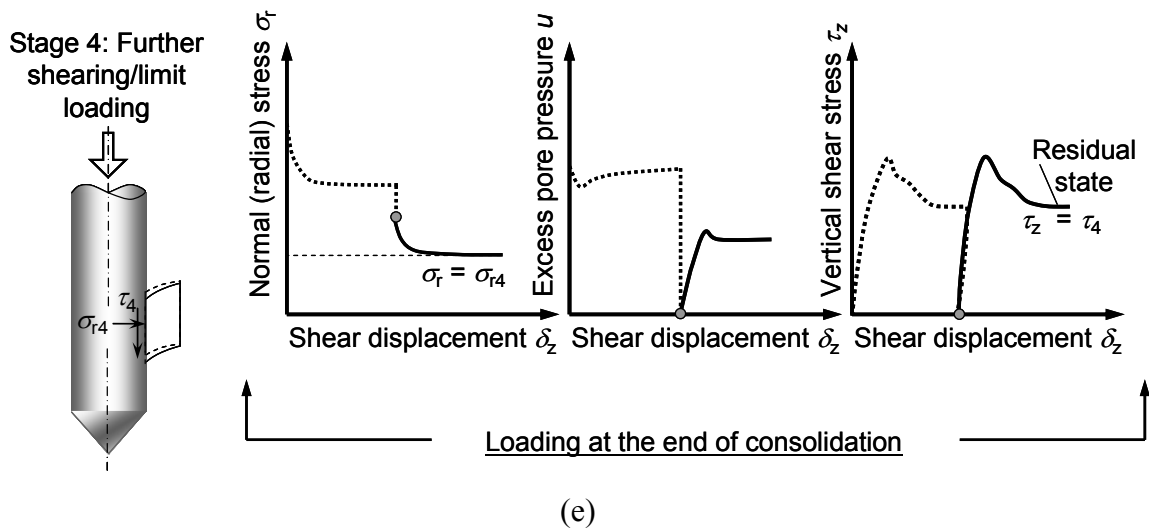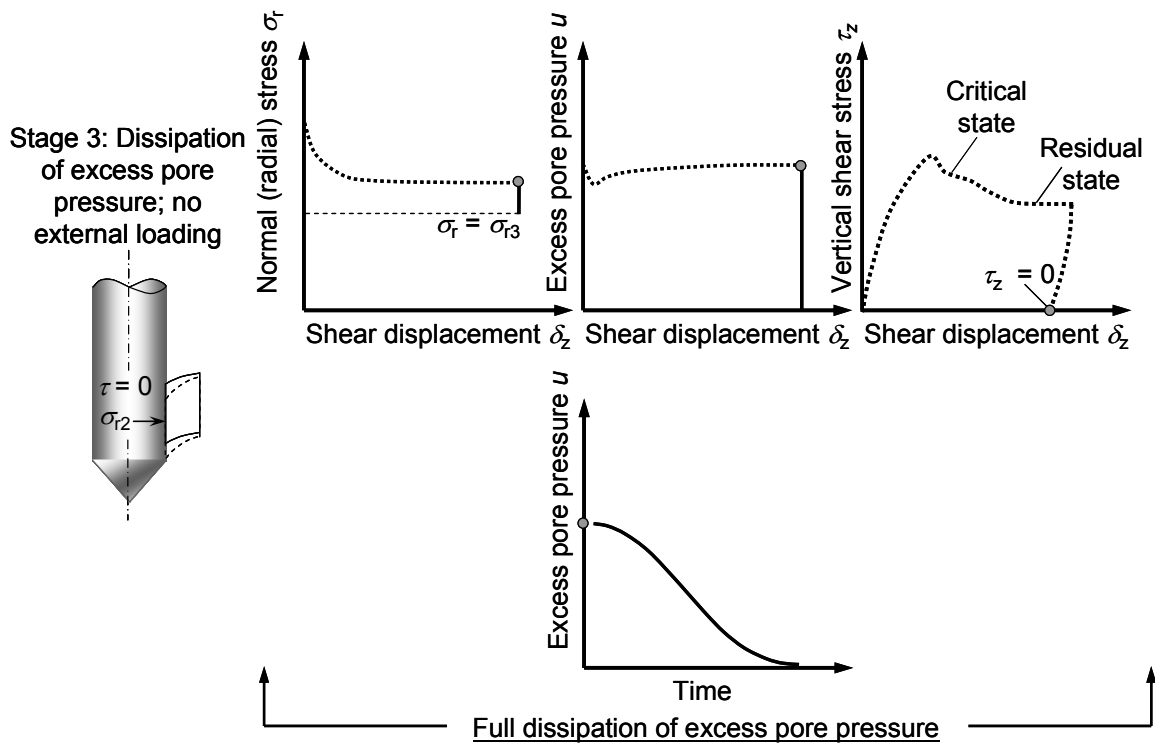
Figure 3.1 Stages involved in the jacking (installation) of a pile in clay, dissipation of excess pore pressure, and undrained loading of the pile

Stage 2 (Figure 3.1c) represents the removal of the jacking load, which occurs after the maximum jacking stroke length *s* of the hydraulic jack is reached or at the end of installation. During the shear unloading stage, the total normal stress remains practically unchanged ($\sigma_{r2} \approx \sigma_{r1}$) and the shear stress τ_z is reduced from τ_1 until it becomes equal to zero (we assume that the residual shear stress acting on the pile shaft at this stage is equal to zero). Due to the instantaneous nature of jacking load removal, the unloading process remains practically undrained. *Stage* 2 represents the end of installation (EOI) for a monotonically jacked pile.

At *Stage* 3, we allow the generated excess pore pressure to stabilize (dissipate) completely. During *Stage* 3 (Figure 3.1d), the shear stress does not change (remains equal to zero) and, at the end of this stage, the excess pore pressure becomes equal to zero. Due to the dissipation of excess pore pressure, the effective stress increases during *Stage* 3. Biot's coupled consolidation theory (Biot 1941) was used to model this consolidation phase (dissipation of excess pore pressure with time). According to Biot's theory, both the effective stress and the excess pore pressure change during consolidation; however, they do not necessarily counterbalance each other, and thus, a change in total stress is possible during *Stage* 3 (the consolidation phase). The difference between the reduction in excess pore pressure and the increase in the effective stress is reflected through a reduction in the normal stress from σ_{r1} to σ_{r3} at the end of *Stage* 3.

Stage 4 (Figure 3.1e) represents the application of the structural load (or the performance of a static pile load test) for a pile installed monotonically. The soil element adjacent to the pile shaft is expected to reach the residual shear strength at the end of this stage. A limit shear stress τ_4 is reached along the pile shaft and the normal stress acting on the pile shaft reduces from σ_{r3} to σ_{r4}.

For a pile installed using multiple jacking strokes, *Stage* 4 represents the application of the next jacking stroke. For piles installed using multiple jacking strokes, *Stage* 3 (consolidation phase) is omitted after *Stage* 2, and *Stage* 4 represents the second jacking stroke. Subsequent jacking strokes are represented by successive repetition of *Stages* 2 and 4 (multiple releases and re-applications of the jacking load at the pile head). At the end of installation, we allow the dissipation of the generated excess pore pressure

(as represented by *Stage* 3). Finally, we repeat *Stage* 4 to simulate the application of the structural load (or the load applied during a static pile load test).

3.2.2. Mesh and Boundary Conditions

We consider a disk of soil around the pile shaft to model the pile shaft-soil interaction during installation, dissipation of excess pore pressure and subsequent loading. We also assume that the vertical normal strain is negligible and that there is no bending deformation. Using these assumptions, the analysis becomes independent of the thickness of the soil disk, and thus, one-dimensional. These conditions resemble closely those existing at depths that are sufficiently removed from the ground surface and from the pile base. A similar approach was used to investigate the shaft resistance of nondisplacement piles in clays and sands (Randolph and Wroth 1978, Potts and Martins 1982, Salgado 2006, Loukidis and Salgado 2008b) and also of jacked piles in sands (Basu *et al*. 2009).

In reality, the vertical normal strain at depths very close to the pile tip may not be negligible. There is compression of the soil just below the tip during pile penetration and then unloading of the same soil element as the tip moves below it. Near the ground surface, the deformation of the soil is less constrained than at lower depths, and, consequently, rotation may occur in a soil element along with the development of non-negligible vertical normal strain. Therefore, the assumptions in the 1-D analyses are not strictly valid near the pile tip and the ground surface. However, these assumptions closely resemble conditions existing at depths that are sufficiently removed from the ground surface and from the pile base.

Figure 3.2 shows the finite element (FE) mesh, boundary conditions, and nodal constraints used for the analyses. The mesh consists of a row of 8-noded rectangular axisymmetric elements with 4 Gauss-quadrature points. Along with the displacement fields, we also consider excess pore water pressure as a continuous field inside the domain. Each corner node of the rectangular elements has three degrees of freedom (DOF): radial displacement, vertical displacement and excess pore pressure. The middle nodes, lying on the vertical and horizontal sides of the elements, have only the displacement DOFs. All corresponding DOFs of the nodes lying along a vertical line are

tied together to enforce the condition of zero normal vertical strain (i.e., no extension/contraction of soil in the vertical direction) and no bending deformation (i.e., no rotation of the vertical sides of the elements). Imposition of this constraint (tying the corresponding DOFs along any vertical line) guarantees that shearing takes place only in the vertical direction and makes the analysis results independent of the height of the rectangular elements. We also constrain all DOFs of the nodes lying on the left (innermost) and right (outermost) boundaries of the domain. These constraints allow us to measure the reaction at the left boundary (pile shaft-soil interface) and to enforce the conditions of zero displacement and zero excess pore pressure at the far field. At different stages of the pile installation and loading process, radial and vertical displacement increments are applied at the nodes on the leftmost boundary of the domain. At these nodes, we monitor the reactions and excess pore pressure generated due to the applied displacement increments.

(a)

(b)
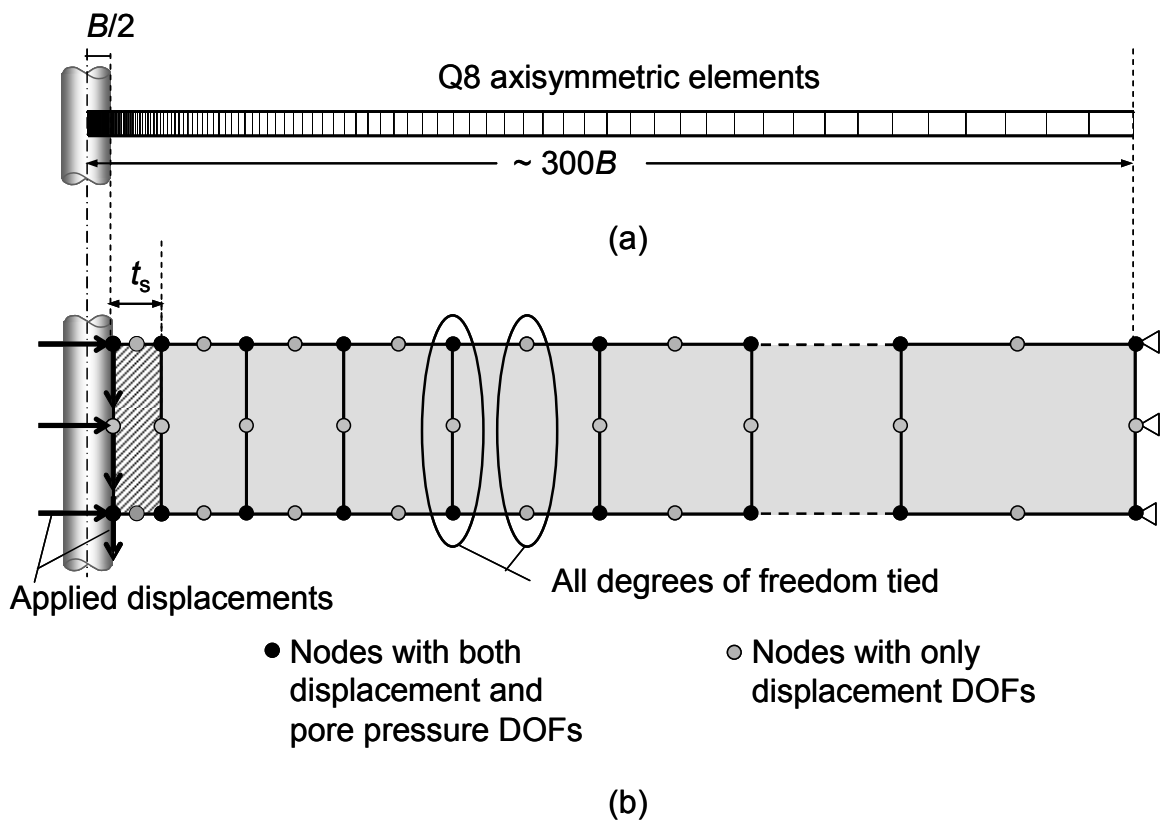
Figure 3.2 One-dimensional domain considered in the analysis: (a) finite element mesh and (b) boundary conditions and applied displacements

We assume that the excess pore pressure around the pile shaft (generated during pile installation) dissipates through a radial outward flow away from the pile shaft. Results from a field study on instrumented model jacked piles in overconsolidated soft marine clay show that for most of the pile length (except near the ground surface or near the pile tip) the excess pore pressure dissipates through radial flow away from the pile (Konard and Roy 1987). Nonetheless, some vertical dissipation of excess pore pressure may occur if a layer with higher hydraulic conductivity is present in the ground within the pile length. Following the assumption of radial pore pressure dissipation in a purely clay deposit, we consider the pile shaft-soil interface (leftmost boundary) and the top and bottom boundaries of the domain to be impervious.

In FEA involving a strain-softening material, as in the present study, the development of a shear band (localization of shear strain within a band) may lead to a nonunique solution, leading to a physically irrelevant solution (Zienkiewicz and Taylor 2000). In these cases, shearing tends to intensify in a particular zone and thus hinders the load transfer to the neighboring regions. Therefore, successive refinements of the FE mesh may not lead to the convergence to a unique solution because, whenever softening starts, shear strains tend to localize in incrementally smaller elements (in the refined mesh). Complex FE formulations involving different regularization techniques (e.g., the Cosserat continuum, gradient-dependent plasticity, and non-local plasticity) can be used to deal with the nonuniqueness. These techniques use implicit or explicit length scales to capture the deformation inside the shear bands, which also involves a significant amount of material rotation. A realistic shear band thickness can thus be predicted.

In the present study, we are dealing with the pile installation problem for which the zone of shear strain localization is known a priori. After the peak stress is reached, strains localize intensively near the pile shaft (i.e., in the leftmost element adjacent to the pile shaft), and a vertical shear band is formed. Shear bands are formed during undrained shearing of both NC and OC clays. However, compared to NC clays, shear bands are

more prominent in OC clays (Oka *et al*. 2005). An element thickness (and, consequently a shear band thickness t_s) that is either too small or too large would produce stresses and strains that would be unrealistic and incorrect. By keeping the thickness of the leftmost element consistent with the expected shear band thickness, we can correctly represent the shear banding along the pile shaft and calculate unit limit shaft resistance accurately. The constitutive model that we use in this study does not explicitly account for material rotation and does not include asymmetric stress tensors. However, this model is able to adequately predict the tractions at the boundaries of shear bands. Therefore, we can avoid the problem of solution nonuniqueness by ensuring that the element size near the zone of shear strain localization (i.e., at the pile shaft-soil interface) does not exceed the expected value of the shear band thickness observed for clays. This technique also allows us to use a simpler FE formulation. In modeling the penetration of cylindrical and spherical penetrometers in clay, Zhou and Randolph (2007) used the smallest element size (adjacent to the penetrometers) equal to 2.5% of the diameter of the penetrometers. In the present analysis, the thickness of the smallest element (adjacent to the pile shaft) reduces from 8.7% of the pile diameter B at the beginning of CE to 1% of B at the end of CE phase (before the primary shearing phase starts).

Theoretically, the thickness of the smallest element adjacent to the pile shaft can be twice the thickness of the expected shear band. This means that shear strain localization will occur only in the first (nearest to the left boundary) line of quadrature points within the first (1st) element adjacent to the pile shaft. However, in the simulation of an undrained process (like the one we are dealing with in the present study), this formulation that allows localization of shear strain only at the leftmost quadrature points of the 1st element leads to the development of a high gradient of excess pore pressure within the first element, and the analysis becomes unstable. We avoid this problem by selecting an adequate size for the 1st element. With the selected size of the 1st element the excess pore pressures developed at different nodes do not create a very high gradient across the element, and thus, we avoid the instability problem.

An alternate approach to eliminate the problems associated with shear strain localization would be to use an interface element between the pile and soil. However, this

interface element will need a separate constitutive model to represent the stress-strain response of the pile-soil interface (Hu and Pu 2004). This special constitutive model for the interface also needs to be calibrated using results from interface shear tests. Properly modeled single or multiple interface elements will thus be able to capture the load-deformation mechanism at the pile-soil interface under large shear strains. The use of interface elements would also allow the use of coarser meshes compared to the one used in the present study. In the absence of a separate constitutive model to represent the stress-strain response of the pile-soil interface we did not use this approach in our analysis.

3.3. Solution Algorithms and Applied Displacements

The finite element code SNAC (Abbo and Sloan 2000) is used for the numerical simulations. The modified Newton-Raphson method is used as the solution scheme for the global nonlinear load-displacement system of equations. The elastic global stiffness matrix was used in the modified Newton-Raphson scheme. The constitutive model equations are integrated using a semi-implicit algorithm adapted with sub-incrementation and error control (Loukidis 2006, Chakraborty 2009) using relative stress error tolerance equal to 10^{-4}.

Our analyses are based on the conventional, small-strain finite element formulation with node updating. SNAC was modified to update the position (x and y coordinates) of the nodes after each solution increment (updated Lagrangian approach), which is needed for the proper simulation of a large-deformation problem like the one addressed in this paper. The present approach of using small-strain FEA to solve large-deformation problems is similar to the approach followed by Hu and Randolph (1998) to successfully analyze a two-dimensional large-strain penetration problem. In our 1-D analysis with specific displacement constraints, the elements do not distort. Therefore, the remeshing and stress interpolation techniques used by Hu and Randolph (1998) are not necessary. Basu *et al*. (2009) demonstrated the validity of the present FE approach by comparing the FEA results from cylindrical cavity expansion analysis in sand with the results obtained by other researchers (Yu and Houlsby 1991, Collins *et al*. 1992, and

Salgado and Randolph 2001) who followed analytical and semi-analytical large-strain formulation. In our present analysis, during each load increment (between two successive node updates), the displacement gradient and the corresponding strain increments are very small. The convective terms in the strain definition are one order of magnitude smaller than the Cauchy (infinitesimal) strains. As a result, decreasing the Cauchy strain increments by one order of magnitude leads to a two order of magnitude decrease in the convective terms included in the definition of large strains. Thus, we minimize the error introduced by the omission of the convective terms (present in the large-strain FE formulations) by using sufficiently fine displacement incrementation.

Displacement-controlled analyses were performed, and the displacement increments were applied at the nodes on the left boundary of the domain (contact surface between soil and pile shaft). We monitored the reactions at the nodes where displacement increments were applied. Horizontal displacement increments were applied to the leftmost nodes of the domain to simulate the CE phase associated with pile installation. The CE phase starts from a very small initial cavity radius r_0 (= 0.015 m) and ends when the cavity radius becomes equal to the pile radius R. With a sufficiently small initial cavity radius (compared to the final radius), the limit cavity pressure is closely approximated at the end of the cavity expansion process. Vertical displacement increments are applied at the nodes of the leftmost boundary to simulate the vertical shearing. Any slippage between pile and soil is simulated by the formation of a vertical shear band inside the soil adjacent to the shaft wall. This condition corresponds to a perfectly rough interface. The vertical shearing phase following the CE phase ("primary shearing") is stopped when both normal and tangential reactions at the left boundary of the domain stabilize and the limit state is reached. Negative (upward) vertical displacement is applied at the nodes lying on the pile shaft to simulate the removal of the jacking load (*Stage* 2). The unloading stage is stopped when the shear stress along the left boundary of the domain becomes equal to zero. The unloading (reversal of vertical displacement increment) is automated in the analyses based on two convergence criteria: (i) for three consecutive displacement increments, the corresponding reaction values on the pile shaft differ only by a value equal to or less than 10^{-7} and (ii) the ratio (M_{cc}-

$M_{res})/M_{res}$ becomes less than 1% [where M_{cc} is the ratio of the deviatoric stress q to the mean effective stress p' at critical state, and M_{res} is the same stress ratio corresponding to the residual state]. The first criterion (related to the reactions measured at the pile shaft-soil interface) is applied simultaneously to both the normal and tangential reactions measured at the nodes on the pile shaft to guarantee that the limit state is reached. For analyses involving multiple jacking strokes, we repeat the shear loading and unloading stages after the first shear unloading.

CHAPTER 4. ANALYSIS RESULTS

4.1. Introduction

We performed finite element analysis (FEAs) of piles jacked in London Clay (LC) with different values of initial vertical effective stress (σ'_{v0} = 25, 50, 100, 200 and 400 kPa) and different values of initial OCR (= 1, 2, 4 and 8). The values of the critical-state friction angle ϕ_c (from triaxial compression tests) and the minimum possible residual friction angle $\phi_{r,min}$ for LC were considered to be equal to 21.3° (Gasparre 2005, Gasparre et al. 2007a, Gasparre et al. 2007b) and 9.4° (Bishop *et al.* 1971), respectively. During pile jacking, the clay particles become aligned along the direction of shearing (i.e., along the pile shaft), and the clay is expected to reach the residual state. We performed analyses for the minimum possible residual friction angle $\phi_{r,min}$ of LC [i.e., for (ϕ_c-$\phi_{r,min}$) = 11.9° ≈ 12°]. Two additional sets of analyses were also performed with (ϕ_c-$\phi_{r,min}$) = 0° and (ϕ_c-$\phi_{r,min}$) = 5°. We performed these additional analyses [with varying (ϕ_c-$\phi_{r,min}$)] to assess the effect of residual strength mobilization along the shaft on the limit shaft resistance of a pile jacked in clay.

Ratnam *et al.* (2005) reported results of different *in situ* hydraulic conductivity tests performed by several researchers in different LC deposits. Theses results show that the hydraulic conductivity of LC varies between 9.6×10^{-12} m/s and 8.8×10^{-9} m/s. In our analyses the clay hydraulic conductivity was assumed to be equal to 10^{-10} m/s. We used K_0 values in the analyses that corresponded to different OCR values for LC. These K_0 values (Table 4.1) were determined through simulations of one-dimensional consolidation tests (Chakraborty 2009, Gasparre 2005). Table 4.1 also shows the initial values of void ratio e_0 and undrained shear strength s_u corresponding to different values of *in situ* vertical effective stress σ'_{v0} and OCR values used in the analyses. The values of s_u reported in Table 4.1 were determined from rate-independent element simulations of

isotropic triaxial compression tests (Chakraborty 2009) in MATHCAD. In this chapter, we present and discuss the FEA results obtained at different stages of installation, setup and loading of the pile. We also discuss the changes in the stress state of the soil during and after the installation of a displacement pile.

Table 4.1 Different values of K_0, e_0 and s_u values used in the analyses for LC (σ'_{v0} and s_u are in kPa)

OCR	K_0	σ'_{v0}	e_0	s_u	s_u/σ'_{v0}
1	0.6	25	1.354	4.34	0.173
		50	1.238	8.67	
		100	1.121	17.34	
		150	1.053	26.01	
		200	1.005	34.68	
		250	0.967	43.35	
2	0.9	25	1.268	7.23	0.289
		50	1.151	14.47	
		100	1.035	28.94	
		150	0.967	43.40	
		200	0.918	57.87	
		250	0.881	72.34	
4	1.34	25	1.178	12.30	0.492
		50	1.061	24.60	
		100	0.945	49.20	
		150	0.877	73.80	
		200	0.829	98.40	
		250	0.791	123.00	
8	2.0	25	1.086	21.10	0.844
		50	0.970	42.21	
		100	0.853	84.42	
		150	0.785	126.62	
		200	0.737	168.83	
		250	0.699	211.04	

4.2. Results of the Finite Element Analyses

4.2.1. Evolution of Stress during Pile Installation

Figure 4.1 shows the evolution of the total normal (radial) stress σ_r and the excess pore pressure u at the cavity wall as a function of the cavity radius during the undrained CE phase of *Stage* 1 (for σ'_{v0} = 50 kPa, OCR = 1, 2, 4 and 8). Both σ_r and u reach limiting values at the end of CE. The limit cavity pressure p_L increases with increasing OCR values. At the end of CE, the element adjacent to the cavity wall reaches critical state with a net increase or decrease (depending on the initial value of OCR) of mean effective stress p' (see Figure 4.2). The stress paths shown in Figure 4.2 (for σ'_{v0} = 100 kPa, OCR = 1, 2, 4 and 8) are similar to those expected in the case of undrained shearing of NC and OC clays. For NC and slightly OC clays, the stress paths in q-p' space first reach a peak deviatoric stress q_p before reaching critical state (see Figure 4.2a). For OCR = 8, the stress path initially crosses the CSL in the q-p' space to reach a peak value of stress obliquity (q/p') before reaching the maximum deviatoric stress q_p at critical state. Figure 4.2(b) shows the stress paths in the e-p' space during undrained CE. Due to the volumetric constraint in the undrained CE phase, the void ratio e cannot change from its initial value e_0, and hence the stress paths in the e-p' space are horizontal (parallel to the p' axis). Depending on the initial value of OCR, the initial stress state (initial value of p') and initial void ratio e_0, the point representing the initial soil state may fall either on the right or on the left of the CSL in the e-p' space. For any initial state falling on the right of the CSL, critical state is achieved through a loss of p' (this is the case for NC or slightly OC clays with OCR = 1 and 2, respectively). For OCR = 4, the initial stress state is very close to the CSL and thus the loss of p' is not significant at the end of CE (when the stress state finally falls on the CSL). For OCR = 8, the initial stress state falls on the left of the CSL, and we observe a net increase in p' to reach the CSL at the end of the undrained CE phase.
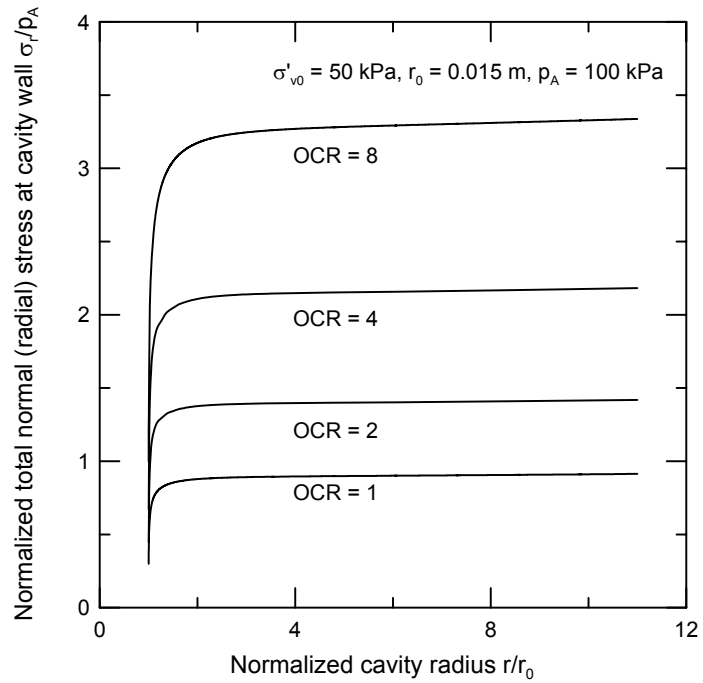
(a)
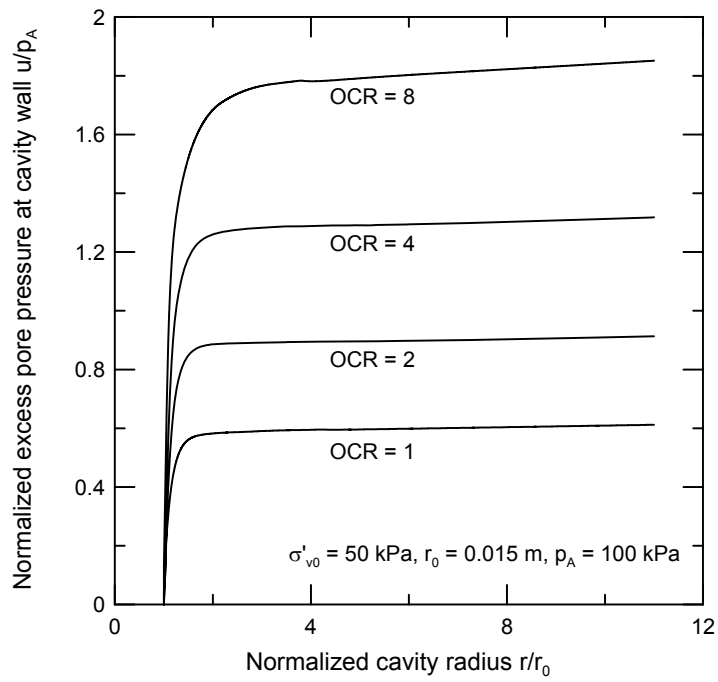
(b)

Figure 4.1 Evolution of stresses during undrained cavity expansion (a) total normal (radial) stress, and (b) excess pore pressure
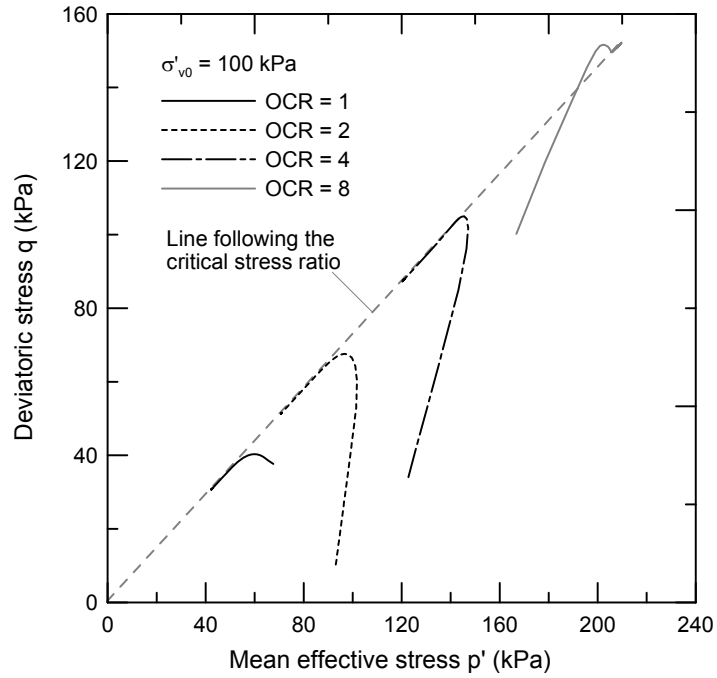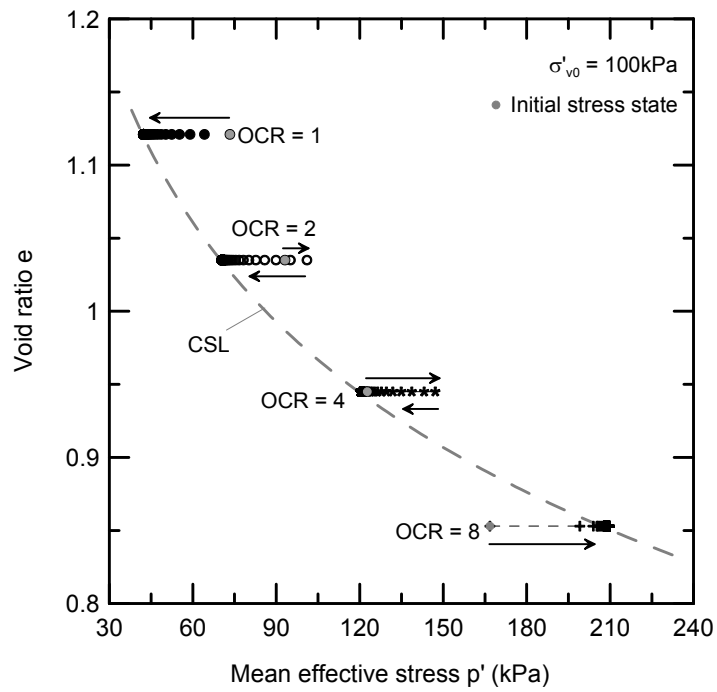
Figure 4.2 Stress paths during undrained cavity expansion in (a) *q-p′* space and (b) *e-p′* space

Figure 4.3 shows [for σ'_{v0} = 100 kPa, OCR = 4 and (ϕ_c- $\phi_{r,min}$) = 12°] the evolution of stresses on the pile shaft during the "primary shearing" (A to B) phase and during the removal of the jacking load (B to C). Point A (Figure 4.3) represents the end of CE when the total normal (radial) stress σ_r acting on the pile shaft and the excess pore pressure u (generated during undrained cavity expansion) are at their limiting values; the vertical shear stress τ_z acting along the pile shaft is zero at this point. During the "primary shearing" phase, the soil element adjacent to the pile shaft first reaches the critical state and then the residual state with continued shearing along the pile shaft. In this process, τ_z acting on the pile shaft increases and reaches a limiting value (point B) at the end of the "primary shearing" phase (which is also the end of S*tage* 1). In the initial part of the "primary shearing" phase, the soil element adjacent to the pile shaft shows a tendency to dilate. As the shearing associated with pile installation is an undrained process (the low hydraulic conductivity of clay does not allow any dissipation of excess pore pressure during fast shearing), the dilatancy (the tendency to increase volume) of the soil element adjacent to the pile shaft causes a decrease in u (through the generation of negative excess pore pressure or suction). As the critical state is approached, the soil response becomes contractive resulting in an increase in u. At critical state, both u and σ_r acting on the pile shaft are stabilized. As shearing continues after the critical state, τ_z continues to decrease and reaches a residual value (point B). At the end of the "primary shearing" phase, the jacking load is removed instantaneously (shear unloading; *Stage* 2) from the pile head. During this process, τ_z acting on the pile shaft decreases to zero (point C). We also observe a slight reduction in u and σ_r. This reduction in u and σ_r is attributed to the generation of suction during undrained shear unloading. Point C represents the end of installation (EOI) for a monotonically jacked pile.
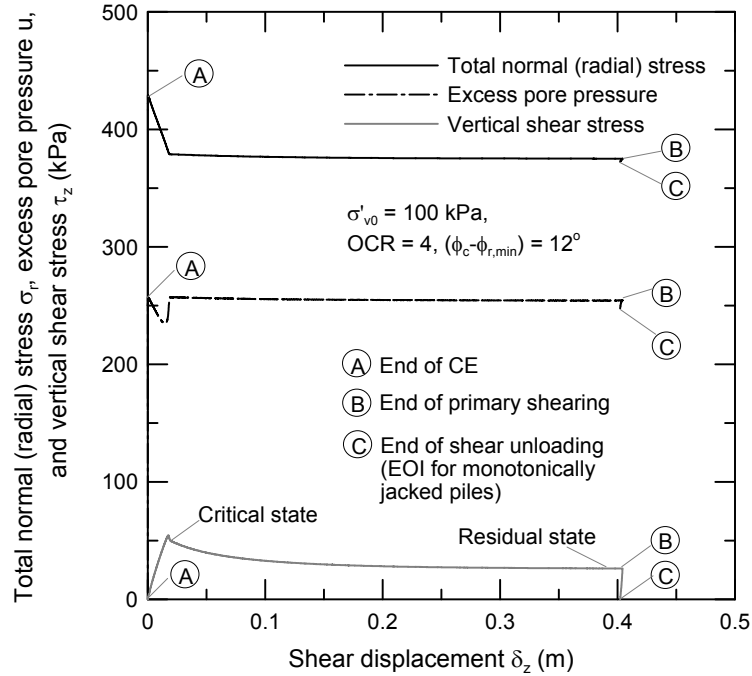
Figure 4.3 Evolution of total normal (radial) stress σ_r, excess pore pressure u, and vertical shear stress τ_z acting on the pile shaft during the "primary shearing" phase and during the removal of the jacking load from the pile head

Figure 4.4 shows [for $\sigma'_{v0} = 100$ kPa, $(\phi_c - \phi_{r,min}) = 12°$, OCR = 1 and 4] the stress path for the leftmost Gauss-quadrature point (located at a distance 0.166 m from the pile axis after CE) of the first element adjacent to the pile shaft. As the "primary shearing" phase starts, the stress state immediately leaves point A (end point of CE) and follows a loop to reach the critical-state stress ratio M_{cc}. With continuing shearing along the pile shaft, the deviatoric stress q decreases (at constant p') until the residual-state stress ratio M_{res} is reached (point B). During the removal of the jacking load (B to C), q decreases continuously with some associated increase in p'. Point C indicates the end of the installation (EOI) for a monotonically jacked pile (installed using a single jacking stroke N; i.e., $N = 1$). Figure 4.5 compares the stress paths [for $\sigma'_{v0} = 100$ kPa, $(\phi_c - \phi_{r,min}) = 12°$, OCR = 4] recorded at quadrature points located at distances 1.66 m ($\approx 5B$), and 3.23 m ($\approx 10B$) from the pile axis. The stress paths plotted in this figure show that the changes in stress state at these locations during installation of a monotonically jacked pile is primarily due to the undrained cavity expansion process.
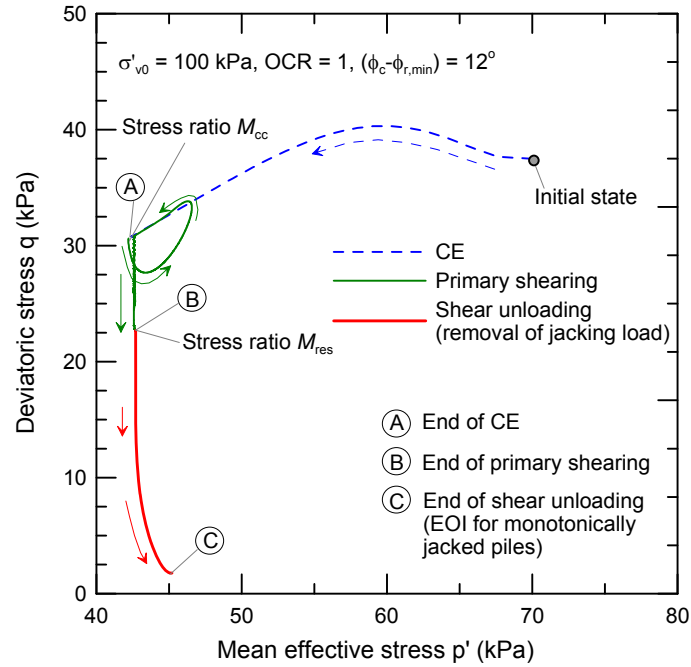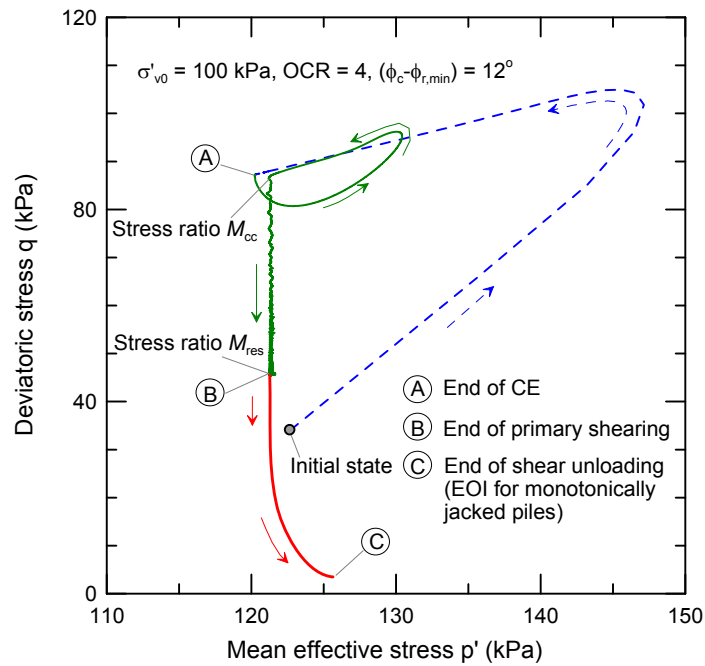
Figure 4.4 Stress paths (in the *q*-*p'* space) recorded at a distance 0.166 m (≈ 0.5*B*) from the pile axis during the installation of a monotonically jacked pile: (a) OCR = 1 and (b) OCR = 4
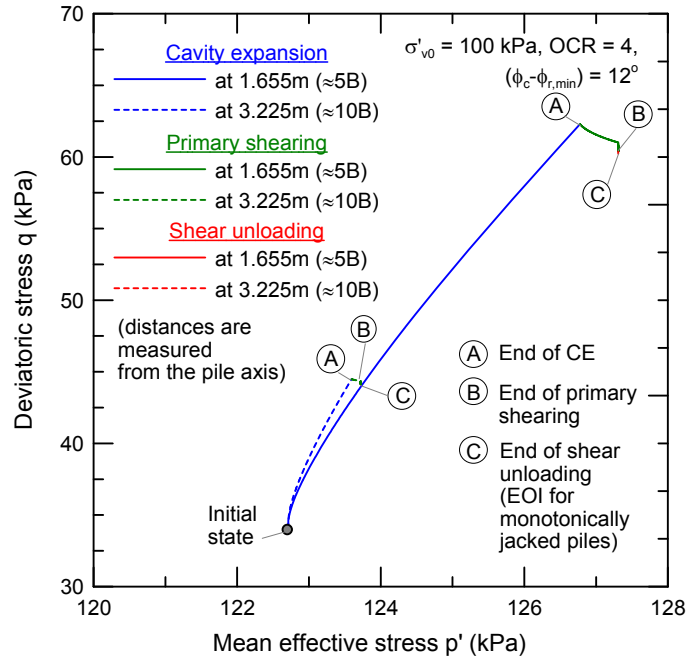
Figure 4.5 Stress paths (in the q-p' space) recorded during the installation of a monotonically jacked pile at distances approximately equal to $5B$ and $10B$ from the pile axis

We repeated the undrained shear loading and unloading stages (successive application and removal of jacking strokes) to model multi-stroke jacking. The number of such shear cycles depends on the number of jacking strokes N. For a pile installed using 30 jacking strokes (i.e., $N = 30$), Figure 4.6 shows the stress path in the q-p' space [for $\sigma'_{v0} = 100$ kPa, $(\phi_c - \phi_{r,min}) = 12°$, OCR = 2 and 4] recorded at the leftmost quadrature point (at a distance 0.166 m from the pile axis after CE) of the first element adjacent to the pile shaft. Up to the first shear unloading (point C), the stress path is identical to that obtained for monotonic jacking (because we follow the same loading steps until point C). Beyond this point, the nodes lying on the pile shaft are subjected to 30 undrained shear loading and unloading cycles. As a result of these cycles, the stress path gradually moves towards the left with a net decrease in p'. The point C_M in Figure 4.6 represents the EOI for a pile installed with 30 jacking strokes.
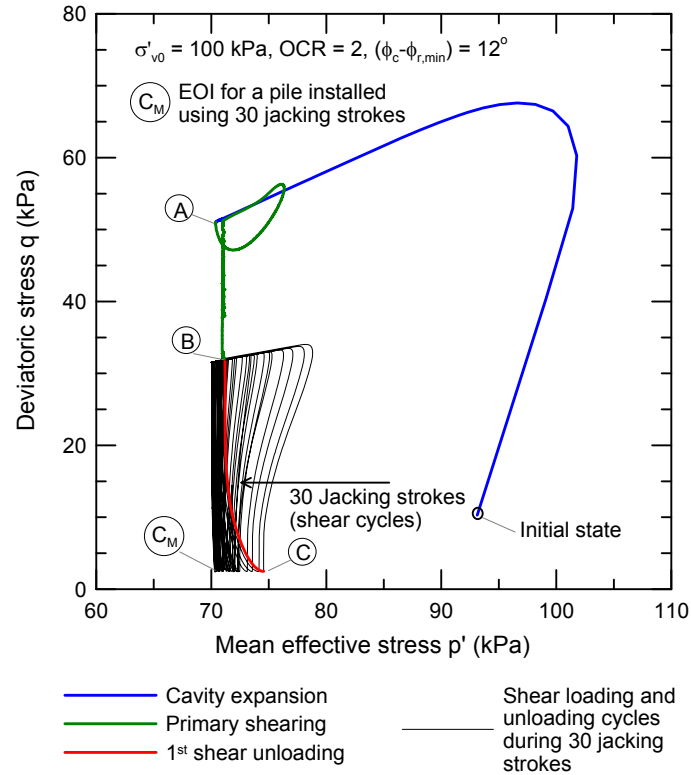
(a)
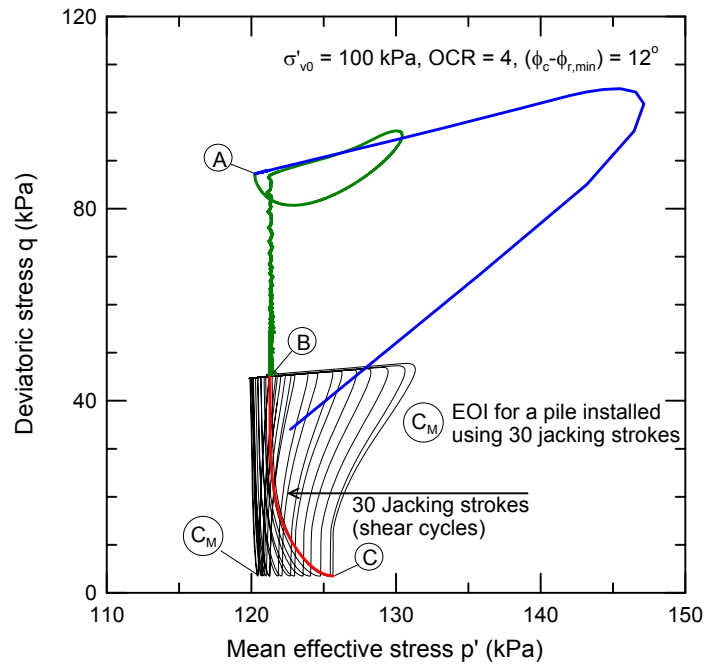
(b)

Figure 4.6 Stress path (recorded at a distance 0.166 m from the pile axis) during the installation of a pile [σ'_{v0} = 100 kPa, (ϕ_c- $\phi_{r,min}$) = 12°] using 30 jacking strokes: (a) OCR = 2, (b) OCR = 4

We observe that the reduction in p' (due to the application of 30 undrained shear cycles along the pile shaft) is not significant; p' reduces only by 5.8% and 4.2% (for OCR = 2 and 4, respectively) as the stress path moves from point C (EOI for a monotonically jacked pile) to point C_M (EOI for a pile installed using 30 jacking strokes). This observation corroborates the fact that *friction fatigue*, observed for piles jacked in sands, is not significant for piles jacked in clays (under undrained conditions). Consequently, we can expect that the shaft resistance of driven piles in clay will not differ significantly from that developed in piles jacked in clay.

4.2.2. Dissipation of Excess Pore Pressure

At the end of installation, we allowed u (generated during pile installation) to dissipate (stabilize) with time. Figure 4.7 shows the decay of u (at different distances from the pile axis) with time [for σ'_{v0} = 100 kPa, (ϕ_c- $\phi_{r,min}$) = 12° and OCR = 4]. Adjacent to the pile shaft, 50% of the excess pore water pressure generated by the installation process dissipates 7 days after pile installation, while it takes 6 months to dissipate 90% of the excess pore water pressure due to pile installation (with the initial conditions σ'_{v0} = 100 kPa and OCR = 4). The u generated during the pile installation process decreases at points further away from the pile axis. The time required for the dissipation of u depends to a great extent on the value of hydraulic conductivity of clay. For example, if we consider the hydraulic conductivity for LC to be 10^{-9} (a value measured using *in situ* tests at different LC sites; Ratnam *et al*. 2005), the time required for the dissipation of 50% and 90% excess pore pressure (generated by the installation process) adjacent to the pile shaft will be 16.8 hours and 18 days, respectively (for the same conditions of Figure 4.7).
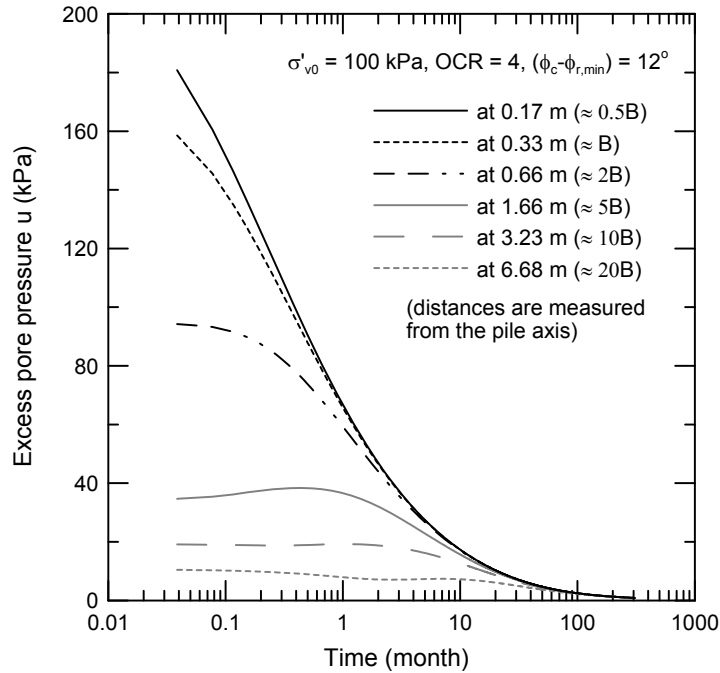
Figure 4.7 Dissipation of excess pore pressure u with time

Figure 4.8 shows the evolution of total and effective normal stress acting on the pile shaft and at some distances from the pile during the dissipation of excess pore pressure generated due to pile installation [for $\sigma'_{v0} = 100$ kPa, $(\phi_c - \phi_{r,min}) = 12°$ and OCR = 4]. Total normal (radial) stress σ_r decreases continuously during the dissipation of excess pore pressure (Figure 4.8a). Effective normal (radial) stress σ'_r acting on the pile shaft and at a distance B from the pile axis increases continuously as the excess pore pressure dissipates. At distances $2B$ and $5B$ from the pile axis, σ'_r decreases in the initial period of excess pore pressure dissipation and increases thereafter (Figure 4.8b).
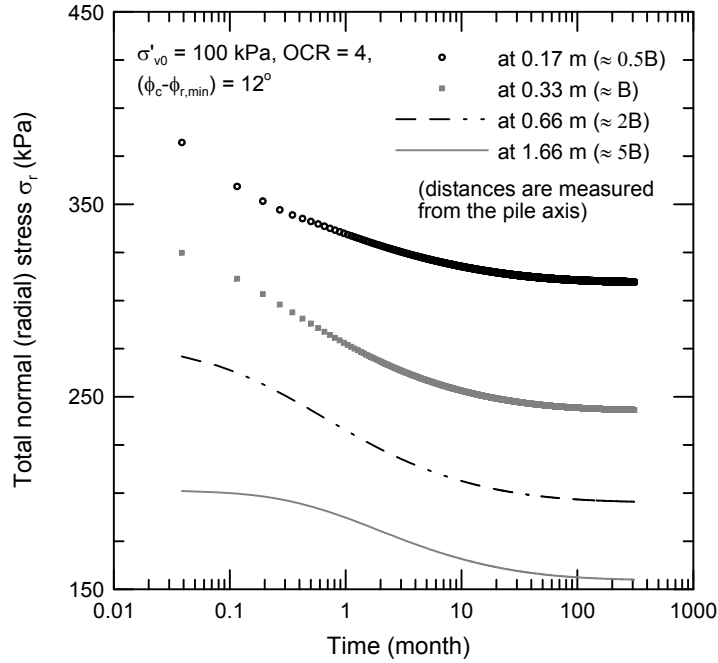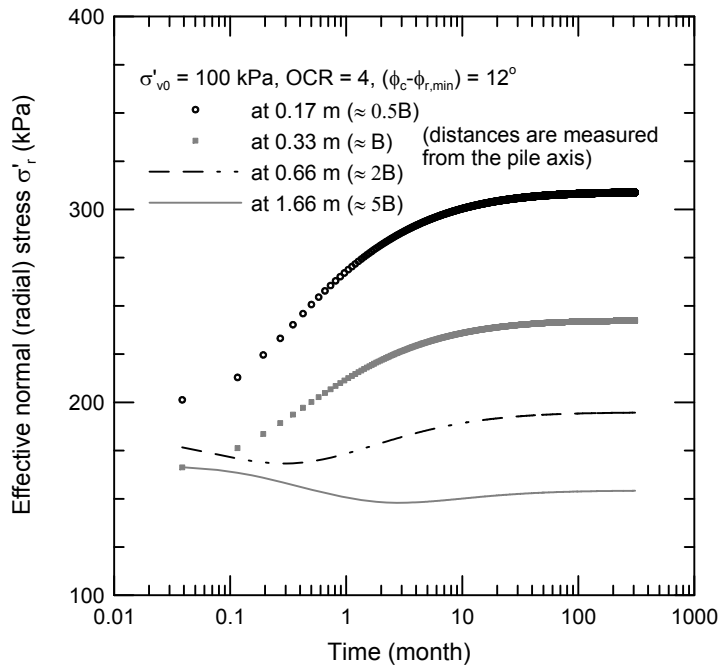
Figure 4.8 Evolution of stresses with time (during the dissipation of excess pore pressure) at different distances from the pile shaft: (a) total normal (radial) stress σ_r, and (b) effective normal (radial) stress σ'_r

Pile installation significantly changes the stress state of the soil surrounding the pile. Figure 4.9 shows the radial distribution of effective normal (radial) stress σ'_r and excess pore pressure u (generated during pile installation) within a zone $20B$ surrounding the pile. As u dissipates from the pile-soil interface towards the free field, σ'_r acting near the pile shaft [within a radial zone approximately equal to $3B$ surrounding the pile for σ'_{v0} = 100 kPa, $(\phi_c - \phi_{r,min}) = 12°$ and OCR = 4] increases significantly from its value at the end of pile installation (Figure 4.9a).

(a)

σ'_{v0} = 100 kPa, OCR = 4, $(\phi_c - \phi_{r,min})$ = 12°

— At the end of installation
---- At the end of 50% dissipation of excess pore pressure
— At the end of 90% dissipation of excess pore pressure
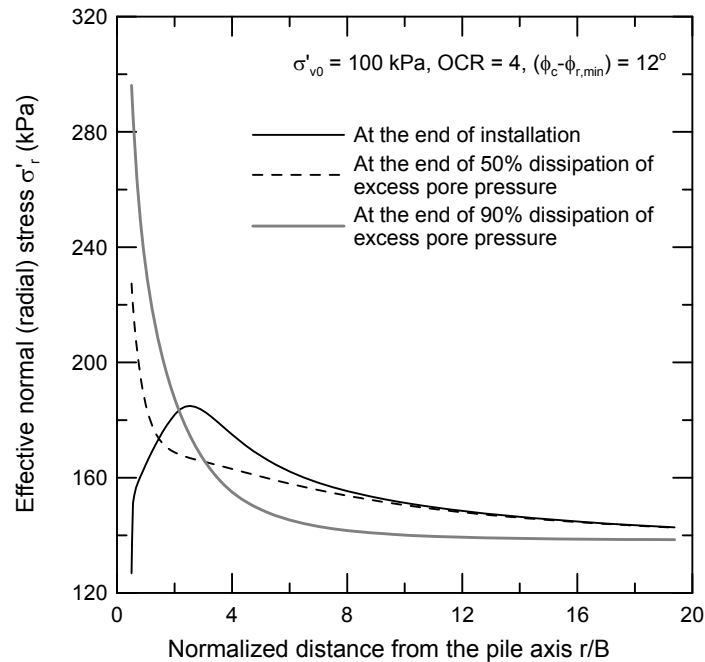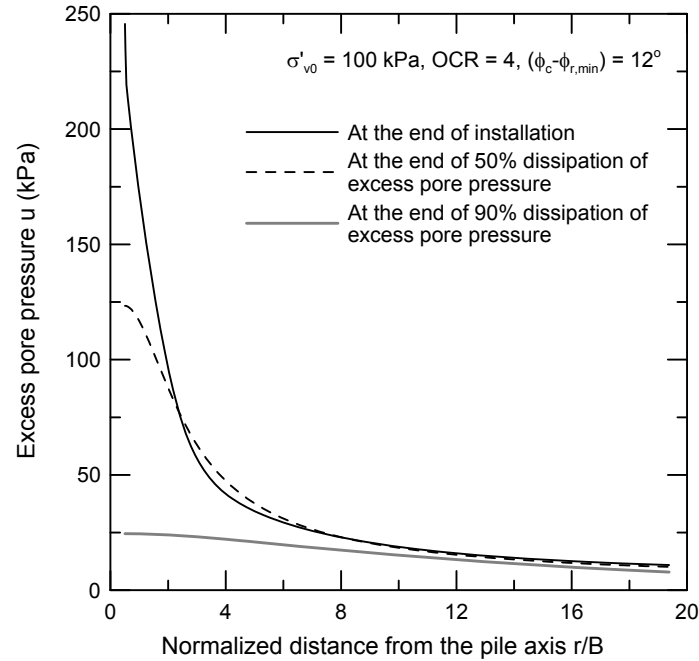
(b)

Figure 4.9 Radial distribution of (a) normal (radial) effective stress σ'_r and (b) excess pore pressure u at the end of installation and at different stages of pore pressure dissipation

4.2.3. Undrained Loading of the Pile

We simulated undrained loading of the pile after full dissipation of the u generated during pile installation. Figure 4.10 shows the evolution of σ_r, u (generated during undrained loading) and τ_z acting on the pile shaft during the undrained loading of the pile. Point D (Figure 4.10) represents the end of the pore pressure dissipation stage when u and τ_z acting on the pile shaft are equal to zero.

The mean effective stress p' increases as u dissipates and the stress state moves closer to the Normal Consolidation Line (NCL) (Figure 4.11). As a result, after u is fully dissipated, the element adjacent to the pile shaft reaches nearly a normally consolidated state. This creates a contractive tendency in the soil surrounding the pile shaft. Due to the volume change constraint during undrained shearing, the contractiveness (tendency to reduce volume) of the soil elements adjacent to the pile shaft is reflected through the generation of positive excess pore pressure during undrained loading of the pile. At the

end of undrained loading (point E_{UD}), a limit condition is reached along the pile shaft; the vertical shear stress τ_z acting on the pile shaft at this limit state is equal to the unit limit shaft resistance q_{sL}.
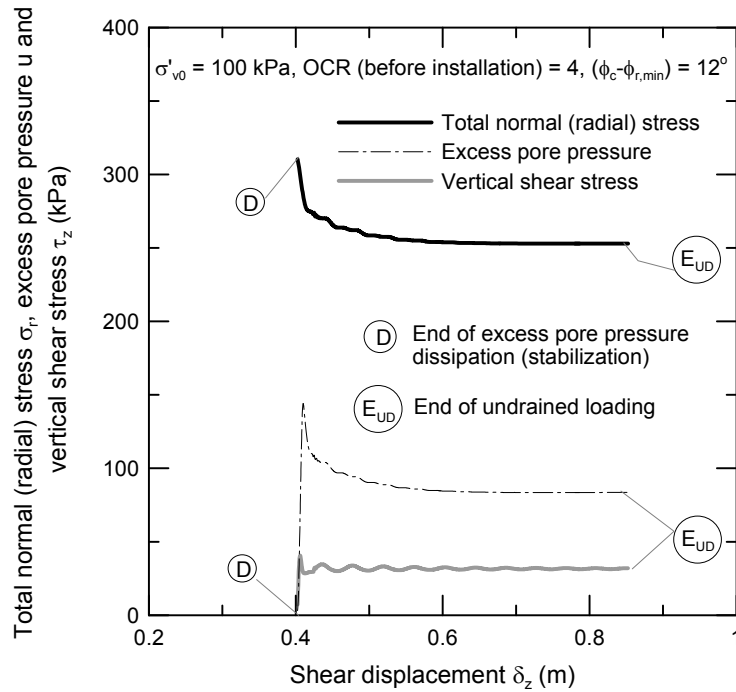
Figure 4.10 Evolution of stresses on the pile shaft during undrained loading of the pile
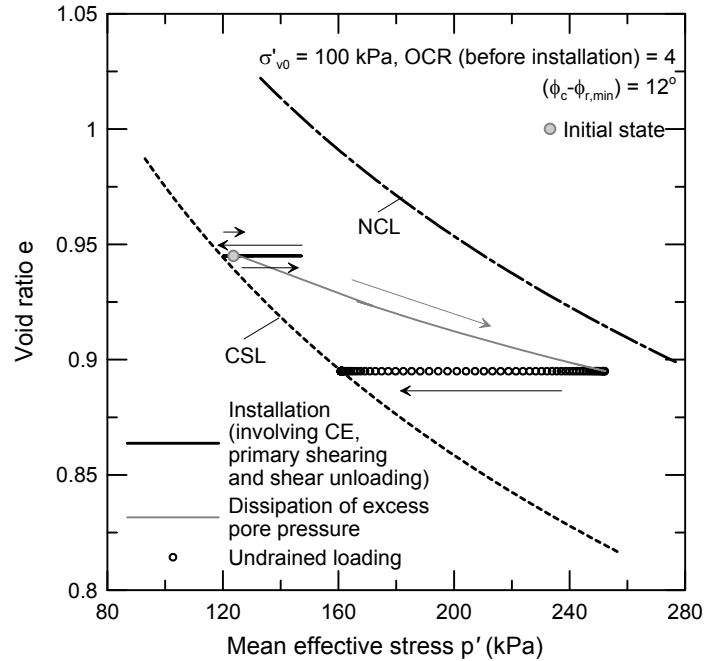
Figure 4.11 Evolution of void ratio *e* and mean effective stress *p'* (for the leftmost quadrature point of the first element adjacent to the pile shaft) during installation, dissipation of excess pore pressure and undrained loading of a monotonically jacked pile

4.3. Summary of Analysis Results

From the results of our analysis we observe that the soil surrounding the pile undergoes complex changes in its *in situ* stress state during the installation (jacking) of the pile, dissipation of excess pore pressure generated during installation, and loading of the pile. During the undrained CE phase (associated with pile installation) the soil surrounding the pile is pushed away radially from the path of the pile. This radial displacement of soil increases the total normal (radial) stress and generates excess pore pressure in the surrounding medium. However, the mean effective stress at a point just adjacent to the pie shaft may increase or decrease depending on the initial value of OCR. The shearing (along the pile shaft) phase associated with pile installation causes a reduction of total normal stress acting on the pile shaft, however, the excess pore pressure generated during the CE phase remains practically unchanged at the end of this phase. At the end of installation (after the jacking load in removed from the pile head), the shear

stress acting on the pile shaft becomes zero (as we neglect any residual shear stress that might be present along the pile shaft at this stage).

The effective normal (radial) stress and the mean effective stress within a zone near the pile shaft increases as the excess pore pressure (generated during installation) dissipates (through a radial flow) away from the pile. Consequently, the soil surrounding the pile tends to approach the NCL. The increase in the effective normal stress acting on the pile shaft increases the limit shaft resistance of the pile. Therefore, the evolution of soil stress state during the dissipation of u plays an important role in determining the load carrying behavior of the pile during loading. In the next chapter, we present the coefficient of limit shaft resistance α which would be obtained from undrained load tests performed on a jacked pile in clay at different times after the installation.

CHAPTER 5. USE OF RESULTS IN DESIGN AND QUALITY ASSURANCE OF PILING

5.1. Introduction

The existing methods for estimating the limit shaft resistance of displacement piles in clay rely mostly on empirical relations based on data from experimental research on model or full-scale piles. These methods relate the limit shaft resistance to relevant soil state (existing before pile installation, as represented by a variable such as the *in situ* vertical effective stress σ'_{v0}) and/or shear strength parameters, such as the *in situ* undrained shear strength s_u. Three different approaches are available in the literature: the total stress approach (α method), the effective stress approach (β method), and the mixed approach (λ method). In this report, we follow the total stress approach to estimate the limit shaft resistance of a pile jacked in clay. According to the total stress approach, the unit limit shaft resistance q_{sL} is related to s_u through a factor α:

$$q_{sL} = \alpha s_u \tag{5.1}$$

The factor α is commonly known as the coefficient of shaft friction. In this chapter, based on the FE simulation results (presented in Chapter 4), we propose a set of equations for the estimation of q_{sL} of a pile jacked in clay as function of the initial soil state and the intrinsic shear strength parameters. The proposed equations can be used for short- and long-term capacity calculations of displacement piles in clays. In this chapter we also propose setup factors, to be used in conjunction with the proposed equations, to calculate the shaft resistance of displacement piles in clays at different times after the installation.

5.2. Proposed Equations for α

We calculate a long-term value of α (α_{LT}) from the limiting value of the vertical shear stress τ_z acting on the pile shaft at the end of undrained pile loading (point E_{UD} in Figure 4.10) performed a long time after pile installation. At this stage, τ_z acting on the pile shaft becomes equal to the unit limit shaft resistance q_{sL} that would be available after full dissipation of excess pore pressure generated during pile installation. We also calculate a short-term value of α (α_{ST}) from the limiting value of τ_z acting on the pile shaft at the end of the "primary shearing" phase (point B in Figure 4.3) of installation. This value of τ_z will be equal to the limit unit shaft resistance q_{sL} that would be available if a load test were performed immediately after installation. Mathematically

$$\alpha_{ST} = \frac{\tau_z\big|_{at\ B}}{s_u} = \frac{q_{sL,\ ST}}{s_u} \tag{5.2}$$

$$\alpha_{LT} = \frac{\tau_z\big|_{at\ E_{UD}}}{s_u} = \frac{q_{sL,\ LT}}{s_u} \tag{5.3}$$

We select appropriate values of s_u (corresponding to particular values of σ'_{v0} and OCR) from Table 4.1 to calculate α from equations (5.2) and (5.3). Based on the FEA results, we propose the following equations for α that can be used in the design of a jacked pile in clay:

$$\alpha_{ST} = 1.03\left[A_1 + (1-A_1)\exp\left\{ -\left(\frac{\sigma'_{v0}}{p_A}\right)(\phi_c - \phi_{r,min})^{A_2} \right\} \right] \tag{5.4}$$

and,

$$\alpha_{LT} = 1.28\left(\frac{s_u}{\sigma'_{v0}}\right)^{-0.05}\left[A_1 + (1-A_1)\exp\left\{ -\left(\frac{\sigma'_{v0}}{p_A}\right)(\phi_c - \phi_{r,min})^{A_3} \right\} \right] \tag{5.5}$$

where

$$A_1 = \begin{cases} 0.75 & \text{for } (\phi_c - \phi_{r,min}) = 5° \\ 0.43 & \text{for } (\phi_c - \phi_{r,min}) = 12° \end{cases} \tag{5.6}$$

$$A_2 = 0.55 + 0.43\ln\left(\frac{s_u}{\sigma'_{v0}}\right) \tag{5.7}$$

$$A_3 = 0.64 + 0.40 \ln\left(\frac{s_u}{\sigma'_{v0}}\right) \qquad (5.8)$$

Figure 5.1 and Figure 5.2 show the α values obtained from the FEAs involving the installation and loading of jacked piles in LC, respectively, in the short and long term (shortly after and long after pile installation). These figures also show the predictions using equations (5.4) through (5.8). We observe that α decreases as the initial value (before pile installation) of OCR increases. The *in situ* strength ratio s_u/σ'_{v0} for clay depends on the OCR value (Table 4.1); s_u/σ'_{v0} increases as OCR increases (i.e., soil becomes stiffer with increasing OCR). Therefore, the α value decreases as the s_u/σ'_{v0} value increases. We also observe that the α value depends strongly on the difference of the friction angles at critical and residual state (ϕ_c-$\phi_{r,min}$). For a clay that shows residual behavior, the value of α decreases (for a given OCR value) with increasing values of (ϕ_c-$\phi_{r,min}$) and σ'_{v0}. However, for a clay showing no residual behavior (i.e., for ϕ_c-$\phi_{r,min} = 0°$), the α value does not depend on the σ'_{v0}. The rate of decrease in the value of α is more pronounced for lower values of σ'_{v0}. For clays with OCR $\geq$ 4, α reaches an asymptotic value (this value depends on the value of OCR) for $\sigma'_{v0} \geq$ 150 kPa.

(a)

Figure 5.1 Short-term α values obtained from the results of the FE simulations (for jacked piles in LC) and from the proposed equations for: (a) $(\phi_c\text{-}\phi_{r,min}) = 5°$, and (b) $(\phi_c\text{-}\phi_{r,min}) = 12°$

Symbols are from FE simulations
Lines are from proposed equations
OCR denotes the overconsolidation
ratio of the *in situ* soil

$\phi_c - \phi_{r,min} = 0°$

OCR = 1; s_u/σ'_{v0} = 0.173
OCR = 2; s_u/σ'_{v0} = 0.289
OCR = 4; s_u/σ'_{v0} = 0.492
OCR = 8; s_u/σ'_{v0} = 0.844

Normalized initial vertical effective stress (σ'_{v0}/p_A)
(p_A = 100 kPa)

(a)

Symbols are from FE simulations
Lines are from proposed equations
OCR denotes the overconsolidation
ratio of the *in situ* soil

$\phi_c - \phi_{r,min} = 5°$

OCR = 1; s_u/σ'_{v0} = 0.173
OCR = 2; s_u/σ'_{v0} = 0.289
OCR = 4; s_u/σ'_{v0} = 0.492
OCR = 8; s_u/σ'_{v0} = 0.844

Normalized initial vertical effective stress (σ'_{v0}/p_A)
(p_A = 100 kPa)

(b)

Figure 5.2 Long-term α values obtained from the results of the FE simulations (for jacked piles in LC) and from the proposed equations for: (a) $(\phi_c\text{-}\phi_{r,min}) = 0°$, (b) $(\phi_c\text{-}\phi_{r,min}) = 5°$, and (c) $(\phi_c\text{-}\phi_{r,min}) = 12°$

5.3. Setup Factors

In practice, depending on the construction schedule, the time interval between installation and loading of a pile may not be always enough for the excess pore pressure (generated during installation of piles) to dissipate completely. Therefore, the limit shaft resistance q_{sL} available at the time of pile loading will be intermediate between q_{sL} estimated using the value of α available after full pore pressure dissipation ($\alpha_{long\text{-}term}$) and that estimated using the value corresponding to zero pore pressure dissipation ($\alpha_{short\text{-}term}$, available immediately after installation). We performed analyses to investigate the variation of q_{sL} with time after pile installation. Based on the results from these analyses, we propose a setup factor F_s that allows precise estimation of q_{sL} at any given time after pile installation. We define F_s as the ratio of the q_{sL} available at any particular time t after pile installation to that available immediately after installation. Mathematically:

$$F_s = \frac{q_{sL}\big|_{\text{at time } t \text{ after installation}}}{q_{sL}\big|_{\text{immediately after installation}}} \tag{5.9}$$

Figure 5.3 shows the variation of F_s with time [for σ'_{v0} = 25 and 250 kPa, OCR = 1 and 8, and $(\phi_c\text{-}\phi_{r,min} = 12°)$] available for the dissipation of u after the installation of a jacked pile in LC. We observe that the increase in F_s (and thus also in q_{sL}) with time after installation of a jacked pile depends on both σ'_{v0} and OCR. F_s increases as the initial vertical effective stress (before pile installation) σ'_{v0} increases. For a lower value of σ'_{v0} (= 25 kPa), F_s decreases as OCR increases (except for pile loading within a very short time after installation; see Figure 5.3a); however, for a higher value of σ'_{v0} (= 250 kPa), F_s increases with increasing values of OCR (Figure 5.3b).

The time shown in Figure 5.3 was calculated based on a value of clay hydraulic conductivity equal to 10^{-10} m/s, which is a representative value of hydraulic conductivity for natural LC deposits (Ratnam *et al*. 2005). For a clay deposit with a different value of hydraulic conductivity, the time scales mentioned in Figure 5.3 need to be revised. For example, if the value of hydraulic conductivity of clay deposit at a particular site is equal to 10^{-9} m/s (which is 10 times larger than the value assumed in our analysis) the horizontal axes (i.e., the time axes) of Figure 5.3 should be divided by 10 to have a proper estimation of F_s. Figure 5.4 shows the variation of F_s with normalized time T. To obtain T, we normalize the real time t with respect to clay hydraulic conductivity k, *in situ* undrained shear strength s_u and pile diameter B:

$$T = \frac{ks_u t}{\gamma_w B^2} \tag{5.10}$$

where γ_w is the unit weight of water. The normalization of t, as expressed in equation (5.10), facilitates the use of the proposed setup factors for any value of k and pile diameter B.
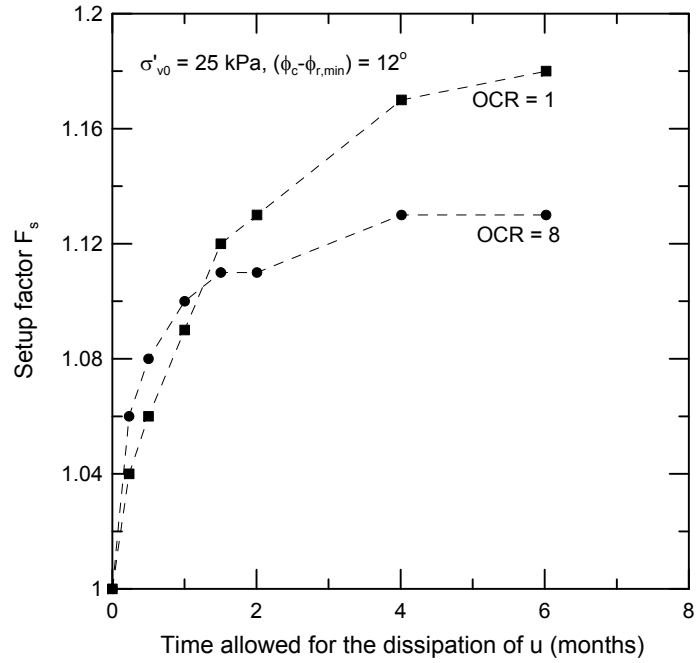
(a)
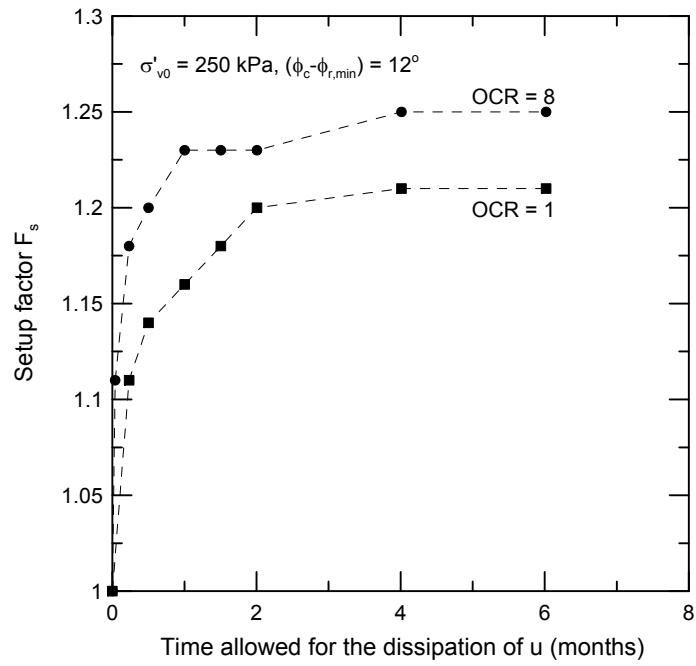
(b)

Figure 5.3 Setup factor F_s at different times after the installation of a jacked pile in LC for: (a) σ'_{v0} =25 kPa, and (b) σ'_{v0} =250 kPa
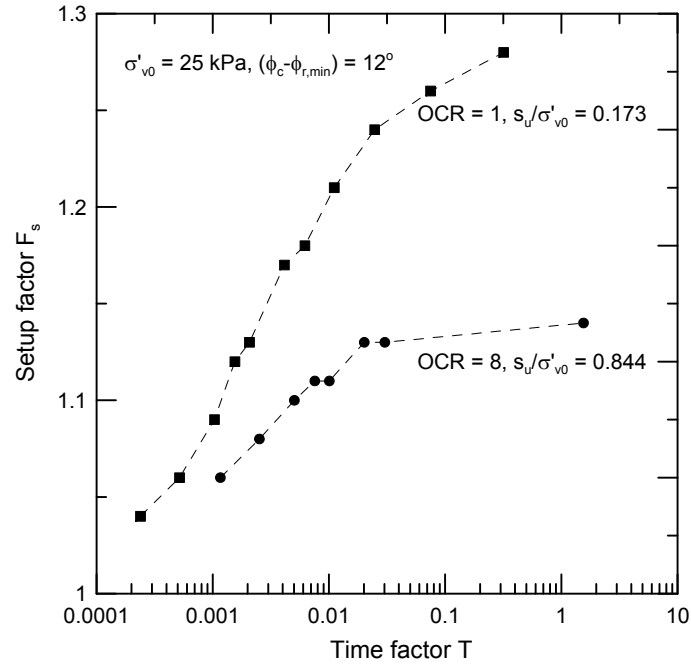
(a)
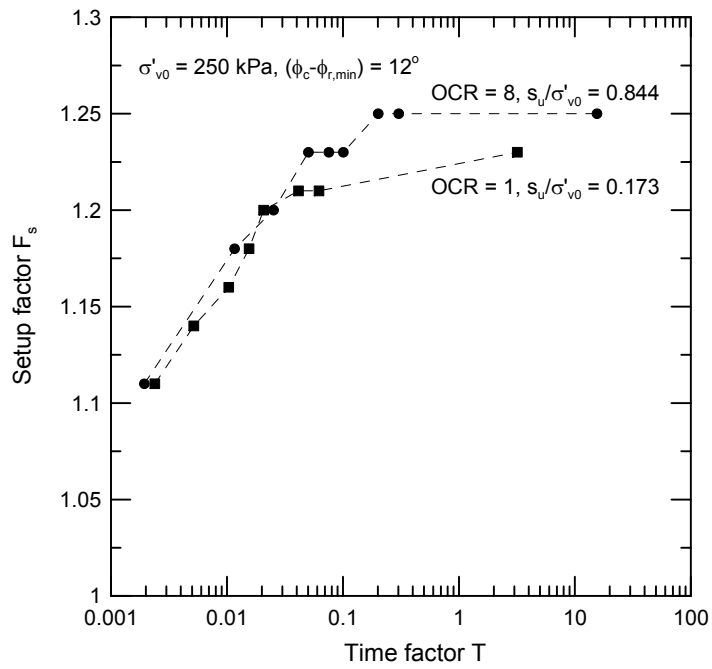
(b)

Figure 5.4 Variation of setup factor F_s with normalized time T after the installation of a jacked pile in LC for: (a) σ'_{v0} =25 kPa and (b) σ'_{v0} =250 kPa

Figure 5.5 shows the variation of F_s with the degree of consolidation U (a direct measure of % dissipation of excess pore pressure generated during pile installation) of the soil adjacent to the pile shaft [for σ'_{v0} = 25 and 250 kPa, OCR = 1 and 8, and (ϕ_c-$\phi_{r,min}$ = 12°)]. Any particular value of U in Figure 5.5 corresponds to different absolute times (elapsed between installation and loading of pile) for different initial conditions (σ'_{v0} and OCR). For σ'_{v0} = 25 kPa, F_s corresponding to a certain degree of consolidation decreases with OCR. However, for σ'_{v0} = 250 kPa, F_s corresponding to a particular value of U does not vary significantly with OCR.
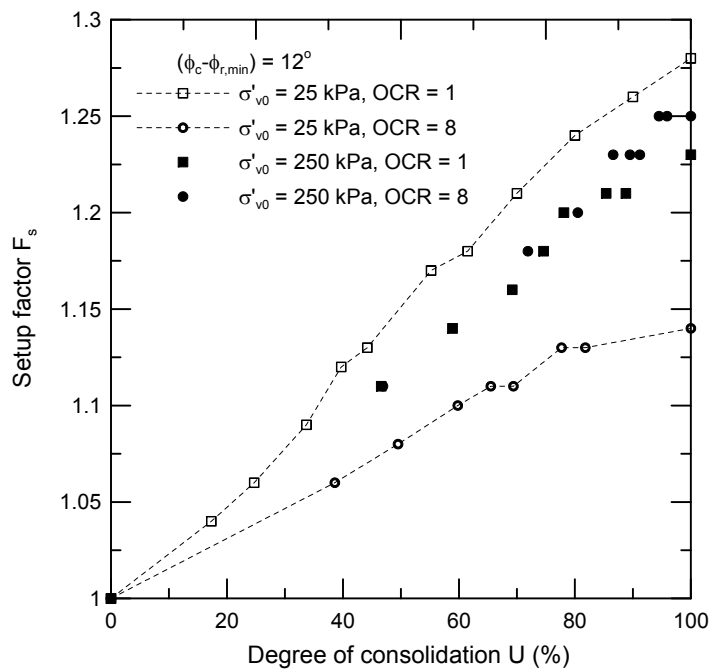
Figure 5.5 Setup factor F_s at different stages of consolidation (just adjacent to the pile shaft) after the installation of a jacked pile in LC

5.4. Validation of the Proposed Equations

We developed equations (5.4) through (5.8) from the results of FEA for LC. To assess the validity of these equations for other clays (having properties different from those of LC) we performed a few additional analyses for piles installed in SFBM [ϕ_c = 29° and (ϕ_c-$\phi_{r,min}$) = 13°]. Figure 5.6 shows that the α values (long-term) predicted using the proposed equations are in good agreement with the α values (long-term) obtained from

the FEA for SFBM (note that the properties of LC and SFBM are different). Additionally, we compared the long-term α values obtained using the equations proposed in this chapter with the α values deduced by Semple and Rigden (1984) from field pile load test on driven piles. Figure 5.7 shows the variation of α values with normalized initial undrained shear strength s_u/σ'_{v0}. We also calculated α values following the API RP-2A (1993) guidelines and included them in Figure 5.7. The α values obtained using the proposed equations are in good agreement with those obtained from the field test results and also with the α values obtained following the API RP-2A (1993) guidelines.
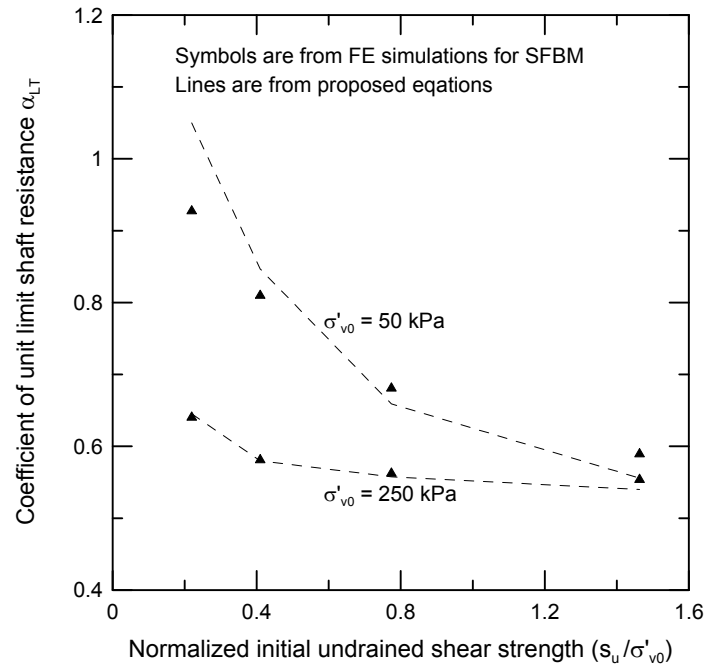
Figure 5.6 Comparison of α values obtained from the results of the FEA for SFBM with those calculated using the proposed equations [with $(\phi_c - \phi_{r,min}) = 13°$]
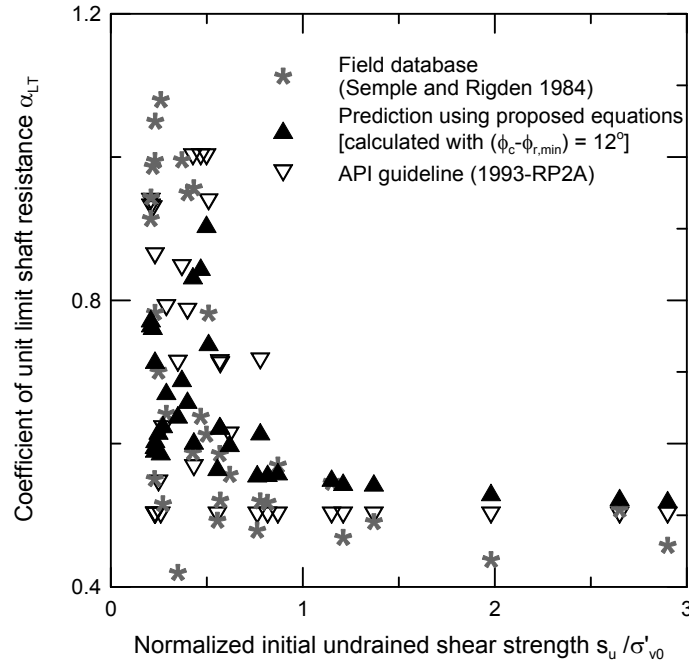
Figure 5.7 Comparison of α values predicted by the proposed equations with those calculated following the API RP-2A criterion and obtained from the field data reported by Sempel and Rigden (1984)

Kim *et al.* (2009) and Seo *et al.* (2009) reported the results of instrumented load tests on closed-ended pipe piles and H piles, respectively. These piles were driven into a multilayered soil profile (11 different soils) and were embedded slightly in a very dense nonplastic silt layer to a depth of 17.4 m. From the results of dynamic pile load tests performed immediately after pile driving and at different times (1, 8, 107 and 127 days) after pile installation, we calculated the setup factors F_s which represent the gain in the local unit limit shaft resistance at different depths within 9m and 17.5m. Figure 5.8 shows the variation of F_s with different values of the time factor T. This figure also shows the values of F_s that would be obtained using the results of the present analysis for a deposit of pure clay. The prediction from our analysis matches well a number of dynamic load tests, but some dynamic test results show either relaxation (i.e., $F_s<1$) or excessive increase in the unit limit shaft resistance. We believe that this shows that dynamic load test (PDA) results have the potential to capture the setup process but in their current state can be substantially in error as well.
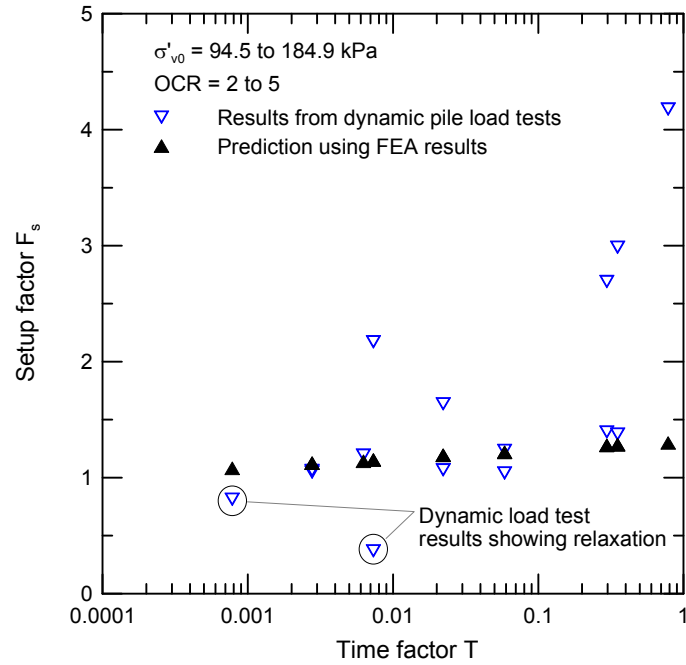
Figure 5.8 Comparison of F_s values deduced from the dynamic pile load test results and those predicted by the present study

CHAPTER 6. SUMMARY AND CONCLUSIONS

6.1. <u>Summary</u>

When piles are installed by jacking or driving, they cause substantial changes in the state of soil located near the pile. These changes result from the complex loading imposed on the soil by expansion of a cylindrical cavity to make room for the pile, by multiple cycles of shearing in the vertical direction as the pile gradually moves down into the ground, and by the slow drainage associated with clayey soils. During the undrained expansion of a cylindrical cavity (associated with pile installation) the soil surrounding the pile is pushed away radially from the path of the pile. This radial displacement of soil increases the total normal (radial) stress and generates excess pore pressure in the surrounding ground. The shearing (along the pile shaft) associated with pile installation causes a reduction of total normal stress acting on the pile shaft; however, the excess pore pressure generated due to cavity expansion remains practically unaltered by the vertical shearing along the pile shaft.

If a pile is load-tested a short time after installation, it will develop an axial resistance that reflects the existence in the soil of the excess pore pressures caused by the installation process. The evolution of the soil stress state during the dissipation of excess pore pressure plays an important role in determining the load carrying behavior of the pile during loading at any particular time after pile installation. The effective normal (radial) stress and the mean effective stress within a zone near the pile shaft increase as the excess pore pressure (generated during installation) dissipates (through radial flow) away from the pile. After the excess pore pressures dissipate, the axial pile resistance will be different from that measured in the short term. This difference is referred to as pile setup (if the resistance increases) or relaxation (if the resistance drops). This report focuses on the pile setup observed in clayey soils, in which it can be quite significant.

Pile setup in clays results primarily from shaft resistance gains with time after installation because the base resistance contributes proportionally much less in soft to medium stiff clays, which are the focus of the present research. Accordingly, our focus has been on analyzing setup in shaft resistance, validating the equations resulting from these analyses and then proposing design and quality assurance procedures based on the results of the analyses. The analyses were done using the finite element method and an advanced constitutive model developed specifically for this project. The constitutive model captures all the key features required for these analyses, and the finite element analyses are 1D analyses of shaft resistance that can handle the large deformations and displacements involved in pile installation. The results of the analyses compare well with load test data from the literature. Design equations for the unit shaft resistance are proposed. Equations for unit shaft resistance in the short term (for comparison with load tests) are also proposed.

6.2. Conclusions

Based on findings of the present study, we can draw conclusions as follows:

1. The changes in the soil caused by pile installation, a rest period and then loading are very complex and cannot be modeled with any reliability in a simplistic way.

2. The pile installation process is not simply a cavity expansion process, as many have believed. Shearing has a large impact in that it reduces the normal stress on the pile shaft from the very large stresses that would be predicted by cavity expansion alone. Cycles of shearing along the pile shaft (applied during pile installation) cause further degradation of the normal stress on the pile-soil interface and thus of the pile shaft resistance. However, this degradation of pile shaft resistance is not as significant as in piles in sand and can be considered small.

3. The ratio of the limit shaft resistance of jacked piles in clay a long time after pile installation (after complete excess pore pressure dissipation) to that just after pile installation ranges from 1.23 to 1.37.

4. The setup factor F_s (with respect to shaft resistance) increases with time after installation of a jacked pile and depends on both σ'_{v0} and OCR. F_s increases as the initial vertical effective stress (before pile installation) σ'_{v0} increases. For a lower value of σ'_{v0} (= 25 kPa), F_s decreases as the OCR increases (except for pile loading within a very short time after installation); however, for a higher value of σ'_{v0} (= 250 kPa), i.e., for deeper pile segments, F_s increases with increasing values of OCR.

5. For low initial vertical effective stress (i.e., vertical effective stress before pile installation), F_s corresponding to a certain degree of consolidation U (just adjacent to the pile shaft) decreases with OCR. This is shown in the report, for example, for $\sigma'_{v0} = 25$ kPa. However, for higher values of σ'_{v0} (for example, 250 kPa), F_s corresponding to a particular value of U does not vary significantly with OCR.

6. The absolute time t required for a certain degree of consolidation around the pile shaft can be normalized with respect to clay hydraulic conductivity k, *in situ* undrained shear strength s_u and pile diameter B.

7. Dynamic pile load test results have the potential to capture the setup process but in their current state can be substantially in error as well.

LIST OF REFERENCES

Abbo, A. J. and Sloan, S. W. (2000). Solid nonlinear analysis code (SNAC), *User manual version 2.0*, Department of Civil, Surveying and Environmental Engineering, University of Newcastle, Australia.

Al-Tabbaa, A, and Stegemann, J.A. (2005) "Stabilisation/solidification Treatment and Remediation: Advances in S/S for Waste and Contaminated Land", *Proceedings of the International Conference on Stabilisation/Solidification Treatment and Rememdiation*, University of Cambridge, United Kingdom, 12-13 April 2005

API RP-2A. (1993). Recommended practice for planning, designing and constructing fixed offshore platforms – working stress design. 20th edition, American Petrolium Institute.

Augustesen, A.H. (2006). The effects of time on soil behavior and pile capacity. Ph.D. Thesis, Aalborg University, Denmark, ISSN 1901-7294.

Axelsson, G. (2000). "Long-Term Increase in Shaft Capacity of Non-Cohesive Soils." Thesis, *Royal Institute of Technology*, Division of Soil and Rock Mechanics, Stockholm, 194 p.

Azzouz, A. S., Baligh, M. M., Whittle, A. J. (1990). Shaft resistance of piles in clay. *Journal of Geotechnical Engineering*, ASCE, Vol. 116, No. 2, pp. 205-221.

Baligh, M. M. (1985). Strain path method. *Journal of Geotechnical Engineering*, ASCE, Vol. 111, No. 9, pp. 1108 – 1136.

Basu, P., Loukidis, D., Prezzi, M., and Salgado, R. (2009). Analysis of shaft resistance of jacked piles in sands. Accepted for publication in the *International Journal for Analytical and Numerical Methods in Geomechanics*.

Bishop, A. W., Green, G. E., Garga, V. K., Andresen, A., and Brown, J. D. (1971). New ring shear apparatus and its application to the measurement of residual strength. *Géotechnique*, Vol. 21, No. 4, 273–328.

Biot, M.A. (1941). General theory of three-dimensional consolidation. *Journal of Applied Physics*, Vol.12, pp. 155-164.

Bonaparte, R. (1982). "A Time-Dependent Constitutive Model for Cohesive Soils." *Ph.D. Thesis*, University of California, Berkeley, CA.

Bond, A.J. and Jardine, R.J. (1991). Effects of installing displacement piles in a high OCR clay. *Géotechnique*, Vol. 41, No. 3, pp. 341-363.

Bullock, Paul Joseph (1999). "Pile Friction Freeze: A Field and Laboratory Study, Volume 1," *Ph.D. Dissertation*, University of Florida.

Carter J. P., Randolph, M. F. and Wroth, C. P. (1979). Stress and pore pressure changes in clay during and after the expansion of a cylindrical cavity. *International Journal of Analytical and Numerical Methods in Geomechanics*. Vol. 3, pp. 305-322.

Chakraborty, T. (2009). Development of a clay constitutive model and its application to pile boundary value problems. Ph. D. Thesis. Purdue University, U.S.A.

Cho, C.W., Lee, M.W., and Randolph, M.F. (2000). "Set-up considerations in wave equation analysis of pile driving", Proc. Conf. on Application of Stress-Wave Theory to Piles, Sao Paulo, Brazil, Balkema, 41-46.

Chow, F.C., Jardine, R.J., Brucy, F., and Nauroy, J.F. (1998). "Effects of Time on Capacity of Pipe Piles in Dense Marine Sand," *Journal of Geotechnical and Geoenvironmental Engineering, ASCE*, Vol. 124, No. 3, pp. 254-264.

Collins, I.F., Pender, M.J. and Yan, W. (1992), "Cavity expansion in sands under drained loading conditions", International Journal of Numerical and Analytical Methods in Geomechanics, Vol. 16, No. 1, pp. 3-23.

Cooke, R. W., Price, G. and Tarr, K. (1979). Jacked piles in London clay: A study of load transfer and settlement under working conditions. *Géotechnique*, Vol. 29, No. 2, pp. 113-147.

Coop, M.R. and Wroth, C.P. (1989). "Field Studies of an Instrumented Model Pile in Clay." *Geotechnique*, Vol. 39, No. 4, pp. 679-696.

Dafalias, Y. F. and Manzari, M. T. (2004). Simple plasticity sand model accounting for fabric change effects. *Journal of Engineering Mechanics*, ASCE, Vol. 130, No. 6, pp. 622- 634.

Dafalias, Y. F., Manzari, M. T. and Papadimitriou, A. G. (2006). SANICLAY: Simple anisotropic clay plasticity model. *International Journal Numerical Analytical Methods in Geomechanics*, Vol. 30, pp.1231–1257.

Dafalias, Y. F., Papadimitriou, A. G. and Li, X. S. (2004). "Sand Plasticity Model Accounting for Inherent Fabric Anisotropy." *Journal of Engineering Mechanics, ASCE*, Vol. 130, No. 11, pp.1319-1333.

Gasparre, A. (2005). Advanced laboratory characterization of London Clay. Ph. D. Thesis, Imperial College of Science, Technology and Medicine, University of London, England.

Gasparre, A., Nishimura, S., Coop, M. R., and Jardine, R. J. (2007a). The influence of structure on the behaviour of London Clay. *Géotechnique*, Vol. 57. No. 1, pp. 19-31.

Gasparre, A., Nishimura, S., Minh, N. A., Coop, M. R., and Jardine, R. J. (2007b). The stiffness of natural London Clay. *Géotechnique*, Vol. 57, No. 1, pp. 33-47.

Gens A. (1982). "Stress–Strain and Strength of A Low Plasticity Clay" *Ph.D. Thesis*, Imperial College, London University.

Hight, D.W., McMillan, F., Powell, J.J.M., Jardine, R.J. and Allenou, C.P. (2003): "Some characteristics of London Clay," Characterisation of Engineering Properties of Natural Soils, Balkema, pp.851-908.

Hu, L. and Pu, J. (2004). Testing and modeling of soil structure interface. Journal of Geotechnical and Geoenvironmental Engineering, ASCE, Vol. 130, No. 8, pp. 851-860.

Hu, Y. and Randolph, M.F. (1998) A practical numerical approach for large deformation problems in soil. International Journal of Numerical and Analytical Methods in Geomechanics, Vol. 22, No. 5, pp. 327-350.

Jain S. and Nanda, A. (2008). "Constitutive Modelling of San Francisco Bay Mud". *Proceedings of the 12th International Conference of International Association for Computer Methods and Advances in Geomechanics (IACMAG)*, 1-6 October, 2008, Goa, India.

Jain S.K. (1985). "Analysis of The Pressuremeter Test by FEM Formulation of The Elasto-Plastic Consolidation", *Ph.D. Thesis*, Virginia Tech, Blacksburg, Virginia, USA.

Karlsrud, K., and Haugen, T. (1985), Axial static capacity of steel model piles in overconsolidated clay. *Proceedings of the 11th International Conference on Soil Mechanics and Foundation Engineering*, San Francisco, pp. 1401-1406.

Kim, D., Bica, A.V.D., Salgado, R., Prezzi, M. and Lee, W. (2009). Load Testing of a Closed-Ended Pipe Pile Driven in Multilayered Soil, Journal of Geotechnical and Geoenvironmental Engineering, Vol. 135, Issue 4, pp. 463-473.

Kirkgard, M.M., and Lade, P.V., (1991). "Anisotropy of Normally Consolidated San Francisco Bay Mud", Geotechnical Testing Journal, GTJODJ ASTM, Vol. 14, No. 3, pp. 231-246.

Komurka, V.E., Wagner, A.B., and Edil, T.B., (2003) "A Review of Pile Set-Up," *51st Annual Geotechnical Engineering Conference, edited by J.F. Labuz and J.G.* Bentler, University of Minnesota.

Konard, J. M. and Roy, M. (1987). Bearing capacity of friction piles in marine clay. *Géotechnique*, Vol. 37, No. 2, pp. 163-175.

Ladd, C. C. and Edgers, L. (1972). "Consolidated-Undrained Direct Simple Shear Tests on Boston Blue Clay", *Research Report R72-82*, Department of Civil Engineering, MIT, Cambridge, MA.

Ladd, C. C., Varallyay J. (1965). The influence of the stress system on the behavior of saturated clays during undrained shear. *Research Report* No. R65-11, Department of Civil Engineering, Massachusetts Institute of Technology (MIT), U.S.A.

Lee, P. K. K., Tham, L. G., Chan, S. T., Yu, F., and Yang, J. (2004). Recent field study on the behavior of jacked piles. *The Structural Engineer*, pp. 19-22.

Lehane, B. M. (1992). Experimental investigations of pile behavior using instrumented field piles. Ph. D. Thesis, Imperial College of Science, Technology and Medicine, University of London, England.

Lehane, B. M., Jardine, R. J., Bond, A. J., and Chow, F. C. (1994). The development of shaft resistance on displacement piles in clay. *Proceedings of the 13th International Conference on Soil Mechanics and Foundation Engineering*, New Delhi, India, pp. 473-476.

Li, X. S. (2002). "A Sand Model with State-Dependent Dilatancy." *Géotechnique*, Vol. 52, No. 3, pp. 173-186.

Li, X. S. and Dafalias, Y. F. (2000). Dilatancy of cohesionless soils. *Géotechnique*, Vol. 50, No. 4, pp. 449-460.

Ling, H. I., Yue, D., Kaliakin, V., and Themelis, N.J. (2002). "An Anisotropic Elasto-Plastic Bounding Surface Model for Cohesive Soils" *Journal of Engineering Mechanics, ASCE*, Vol. 128, No. 7, pp. 748-758.

Long, J. H., Kerrigan, J. A., and Wysockey, M. H. (1999). Measured time effects for axial capacity of driven piles. *Transportation Research Record 1663*, Paper No. 99-1183.

Loukidis, D. (2006). Advanced constitutive modeling of sands and applications to foundation engineering. Ph. D. Thesis, Purdue University, U.S.A.

Loukidis, D. and Salgado, R. (2008a). Modeling sand response using two-surface plasticity. *Computers and Geotechnics*, doi:10.1016/j.compgeo.2008.02.009 (in press).

Loukidis D. and Salgado R. (2008b). Analysis of the shaft resistance of non-displacement piles in sand. *Géotechnique*, Vol. 58, No. 4, 283-296.

Manzari, M. T. and Dafalias, Y. F. (1997). A critical state two-surface plasticity model for sands. *Géotechnique*, Vol. 47, No. 2, pp. 255-272.

Meehan, C. L. (2006). "An Experimental Study of the Dynamic Behavior of Slickensided Surfaces" *PhD Thesis,* Virginia Polytechnic Institute and State University. Blacksburg, Virginia.

Oka, F., Kodaka, T., and Kimoto, S., Ichinose, T. and Higo, Y. (2005). Strain localization of rectangular clay specimen under undrained triaxial compression conditions. *Proceedings of the 16th International Conference on Soil Mechanics and Geotechnical Engineering*. Osaka, Japan.

Papadimitriou, A. G., Bouckovalas, G. D. and Dafalias, Y. F. (2001). Plasticity model for sand under small and large cyclic strains. *Journal of Geotechnical and Geonvironmental Engineering*, ASCE, Vol. 127, No. 11, pp. 973-983.

Papadimitriou, A. G. and Bouckovalas, G. D. (2002). Plasticity model for sand under small and large cyclic strains: a multiaxial formulation. *Soil Dynamics and Earthquake Engineering*, Vol. 22, No. 3, pp.191-204.

Papadimitriou AG, Manzari MT and Dafalias YF. (2005) "Calibration of A Simple Anisotropic Plasticity Model for Soft Clays." *Proceedings, GeoFrontiers Conference of ASCE, January 24–26*, Austin, TX, Geotechnical Special Publication No. 128, pp. 415–424.

Pestana, J. M., Hunt, C. E., Bray, J. D. (2002). Soil deformation and excess pore pressure field around a closed-ended pile. *Journal of Geotechnical and Geoenvironmental Engineering*, ASCE, Vol. 128, No. 1, pp. 1-12.

Potts, D. M. and Martins, J. P. (1982). The shaft resistance of axially loaded piles in clay. *Géotechnique*, Vol. 32, No. 4, pp. 369-386.

Randolph, M.F. and Wroth, C.P. (1978). Analysis of deformation of vertically loaded piles. *Journal of Geotechnical Engineering*, ASCE, Vol. 104, GT12, pp. 1-17.

Randolph, M. F., Carter, J. P. and Wroth, C. P. (1979). Driven piles in clay – the effects of installation and subsequent consolidation, *Géotechnique*, Vol. 29, No. 4, pp 361-393.

Ratnam, S., Soga, K. and Whittle, R.W. (2005). A field permeability measurement technique using conventional self-boring pressuremeter. *Géotechnique*, Vol. 55, No. 7, pp. 527-537.

Rau, G.A. (1999). "Evaluation of Strength Degradation in Seismic Loading of Holocene Bay Mud from Marin County." *PhD Thesis*, University of California, Berkeley, California.

Salgado, R. and Randolph, M.F. (2001) Analysis of cavity expansion in sand. International Journal of Geomechanics. Vol. 1, No. 2, pp. 175-192.

Salgado, R. (2006). The role of analysis in non-displacement pile design. *Modern Trends in Geomechanics*, Springer Proceedings in Physics, Vol. 106, Eds. W. Wu and H-S Yu , pp. 521-540.

Salgado, R. (2008). Engineering of Foundations. *Mc Graw-Hill*, New York, U.S.A., 2008.

Santagata, M., Germaine, J. T., Ladd, C. C. (2007). "Small-Strain Nonlinearity of Normally Consolidated Clay" *Journal of Geotechnical and Geoenvironmental Engineering*, Vol. 133, No. 1, pp. 72-82.

Sempel, R. M., and Rigden, W. J. (1984). Shaft capacity of driven pipe piles in clay. *Analysis and Design of Pile Foundations*, Ed. J. R. Meyer, ASCE, pp. 59-78.

Seo, H., Yildirim, I.Z. and Prezzi, M. (2009) "Assessment of the Axial Load Response of an H Pile Driven in Multilayered Soil", Journal of Geotechnical and Geoenvironmental Engineering, ASCE, Published Online.

Sheahan TC. (1991) "An Experimental Study of the Time-Dependent Undrained Shear Behavior of Resedimented Clay using Automated Stress Path Equipment.", *Sc.D Thesis*, MIT, Cambridge, MA.

Sheng, D., Sloan, S. W. and Yu, H. S. (2000). "Aspects of Finite Element Implementation of Critical State Models", *Computational Mechanics*, Vol. 26, pp. 185–196.

Skov, R. and Denver, H. (1988). "Time-Dependence of Bearing Capacity of Piles," *Proceedings 3rd International Conference on Application of Stress-Waves to Piles*, pp. 1-10.

Steenfelt, J. S., Randolph, M. F., and Wroth, C. P. (1980). Instrumented model piles jacked into clay. *Proceedings of the 10th International Conference on Soil Mechanics and Foundation Engineering*, Stockholm, Ed. N. Flodin, A.A. Balkema, Rotterdam, Vol. 2, pp. 857-864.

Stewart, H. E. and Hussein, A. K. (1993). "Determination of the Dynamic Shear Modulus of Holocene Bay Mud for Site-Response Analysis." *The Loma Prieta, California, Earthquake of October 17, 1989, Marina District*, Thomas D. O'Rourke (Ed.), pp. 75-84.

Terzaghi, K., Peck, R. B., and Mesri, G. (1996). Soil mechanics in engineering practice, 3rd Edition, *Wiley Inter-Science*, New York.

Titi, H. and Wathugala, G. W. (1999), Numerical Procedure for Predicting Pile Capacity-Sepup/Freeze. Transportation Research Record 1663, TRB, pp 25-32.

Whittle, A. J., and Sutabutr, T. (1999). Prediction of pile setup in clay. *Trasportation Research Record*. No. 1663, pp. 33-40.

Whittle, A. J., DeGroot, D. J., Ladd, C. C., and Seah, T-H. (1994). Model prediction of the anisotropic behavior of Boston Blue Clay. *Journal of Geotechnical Engineering*, ASCE, Vol. 120, No. 1, pp. 199-225.

Whittle. A. J., and Kavvadas, M. J. (1994). Formulation of MIT-E3 constitutive model for overconsolidated clays. *Journal of Geotechnical Engineering*, ASCE, Vol. 120, No. 1, pp. 173-199.

Yu, H.S. and Houlsby, G.T. (1991) Finite cavity expansion in dilatants soils: loading analysis. *Géotechnique*, Vol. 41, No. 2, pp. 173-183.

Zhou, H., and Randolph, M.F. (2007). Computational techniques and shear band development for cylindrical and spherical penetrometers in strain-softening clay. *International Journal of Geomechanics*, Vol. 7, No. 4, pp. 287-295

Zienkiewicz, O. C. and Taylor, R. L. (2000). The finite element method: Volume 2 – Solid mechanics, *Butterworth-Heinemann Ltd*.